PHOTOCATALYTIC NO_X OXIDATION AND STORAGE UNDER AMBIENT CONDITIONS FOR AIR PURIFICATION

A THESIS

SUBMITTED TO THE DEPARTMENT OF CHEMISTRY

AND THE GRADUATE SCHOOL OF ENGINEERING AND SCIENCE

OF BİLKENT UNIVERSITY

IN PARTIAL FULFILLMENT OF THE REQUIREMENTS

FOR THE DEGREE OF

MASTER OF SCIENCE

By

ASLI MELİKE SOYLU

July 2012

To My Family

and Deniz

I certify that I have read this thesis and that in my opinion is it is fully adequate, in scope and quality, as a thesis of the degree of Master in Science

……..

Asst. Prof. Dr. Emrah Özensoy (Supervisor)

I certify that I have read this thesis and that in my opinion is it is fully adequate, in scope and quality, as a thesis of the degree of Master in Science

……..

Prof. Dr. Deniz Üner

I certify that I have read this thesis and that in my opinion is it is fully adequate, in scope and quality, as a thesis of the degree of Master in Science

……..

Prof. Dr. Ömer Dağ

Approved for the Graduate School of Engineering and Science

……..

Prof. Dr. Levent Onural

Director of the Graduate School of Engineering and Science

ABSTRACT

PHOTOCATALYTIC NO_X OXIDATION AND STORAGE UNDER AMBIENT CONDITIONS FOR AIR PURIFICATION

ASLI MELİKE SOYLU

M.S. in Chemistry

Supervisor: Asst. Prof. Dr. Emrah Özensoy

July, 2012

Air pollution is one of the most serious environmental problems in both urban and rural settings with a direct impact on human health. A variety of chemical compounds can be associated with air pollution and gaseous nitrogen oxides (NO_x), such as NO and NO_2, are especially among the most hazardous environmental pollutants. NO_x abatement can be efficiently performed at elevated temperatures (i.e. $T > 300^oC$), however, an important challenge in air purification is the abatement of gaseous NO_x species under ***ambient conditions*** (i.e. at room temperature and under regular atmospheric conditions). Photocatalytic systems offer promising opportunities in order to tackle this important environmental challenge, as these systems can be tailored to efficiently clean/purify air under ambient conditions with the help of ultraviolet (UV) and/or visible (VIS) light.

In the current work, a hybrid technology for the photocatalytic oxidation and storage of gas phase NO_x species is proposed where titania based powders are investigated as candidate photocatalytic materials. With this aim, various components of a thermally activated conventional NO_x Storage/Reduction (NSR) catalyst is combined with a photocatalytically activated NO_x oxidation catalyst to obtain a photocatalytically activated NO_x oxidation and storage material. In this regard, three different sets of samples were prepared and investigated.

The first set of photocatalysts was prepared by employing Al_2O_3, a high surface area support material, in order to disperse the photocatalytically active titania in an effective manner. Using a "sol-gel co-precipitation method", TiO_2/Al_2O_3 binary oxides were synthesized (where TiO_2:Al_2O_3 mole ratio was chosen to be 0.25, 0.5, 1.0) and characterized by X-ray diffraction, Raman Spectroscopy and BET. For these samples, the effects of specific surface area, calcination temperature and the crystallinity of TiO_2 were investigated in relevance to the photocatalytic NO_x oxidation/storage reaction.

Next, an alkali/alkaline earth oxide storage component is added to the TiO_2-Al_2O_3 mixture and the incorporation of the storage component is achieved via two different routes; (i) either through "incipient wetness impregnation" of 5 or 10% (w/w) metal nitrate [$M(NO_3)_x$] salts on TiO_2-Al_2O_3 and a subsequent calcination to obtain alkali/alkaline earth oxides [M_yO] or (ii) by physically grinding 5 or 10% (w/w) BaO powder with TiO_2-Al_2O_3 binary oxide to obtain a ternary mixture. For these samples, the route of metal oxide incorporation (impregnation vs. physical mixture), the type of metal oxide storage component (alkali vs. alkaline earth metal) and the percentage of metal oxide loading (5% vs. 10%, w/w) were examined in photocatlytic NO_x oxidation/storage reaction.

The photonic efficiencies of these samples were tested using a continuous flow system, composed of mass flow controllers, a custom-made UVA-illuminated reaction cell and an ambient chemiluminescence NO_x analyzer. Photocatalytic performance of all samples were compared with that of a commercially available Degussa P25 TiO_2 benchmark catalyst. Photocatalytic preformance tests revealed that the TiO_2-Al_2O_3 binary oxides had much higher NO_x storage capacities compared to Degussa P25 and the further addition of an alkaline earth oxide (BaO) storage component on TiO_2-Al_2O_3 by physical mixing significantly enhanced the NO_x capture in solid state and decreased unwanted gaseous NO_2 emission to an almost negligible level. On the other hand, the "incipient wetness impregantion" of metal nitrates resulted in metal titanate ($M_xTi_yO_z$) formation on TiO_2-Al_2O_3 binary oxide and diminished the photooxidation ability of the catalyst.

Keywords: Air Purification, Photocatalytic NO_x Oxidation and Storage, TiO_2, $DeNO_x$

ÖZET

FOTOKATALİTİK YÖNTEMLERLE ODA KOŞULLARINDA HAVA ARITIMINA YÖNELİK NO_X YÜKSELTGENMESİ VE DEPOLANMASI

ASLI MELİKE SOYLU

Kimya Yüksek Lisans Tezi

Danışman: Y. Doç. Dr. Emrah Özensoy

Temmuz, 2012

Hava kirliliği, insan sağlığına doğrudan etkisi bulunan en önemli çevre sorunlardan biridir ve hava kirliliğine katkıda bulunan zehirli gaz türlerinin başında NO ve NO_2 gibi azot oksitler (NO_x) gelir. Yüksek sıcaklıklarda ($T > 300^oC$) ısıl-katalitik yöntemler kullanarak NO_x türlerini zararsız kimyasallara başarıyla dönüştürmek mümkündür, ancak aşılması gereken en önemli engellerden biri, NO_x türü gazları ***oda koşulları*** (düşük sıcaklık ve basınç şartları) altında zararsız gazlara dönüştürmektir. Bu bağlamda, fotokatalitik süreçler oldukça umut verici bir alternatif olarak karşımıza çıkmaktadır; çünkü fotokatalitik malzemeler, doğru şekilde türevlendirilip, zenginleştirildiklerinde, mor otesi (UV) ve hatta görünür ışık yardımıyla NO_x dönüşümlerine imkan tanımaktadırlar.

Bu çalışmamızda, gaz fazı NO_x türlerini fotokatalitik olarak yükseltgeyip depolayacak hibrid bir sistem önerilmiş olup, TiO_2 bazlı nanoparçacıklar fotokatalitik malzeme adayları olarak incelenmiştir. Bu amaçla, ısıl olarak aktive edilen NO_x depolama/indirgeme (NSR) sisteminin depolama bileşenleri, fotokatalitik olarak aktive edilen NO_x yükseltgeme katalizörü olan TiO_2 ile biraraya getirilmiş ve fotokatalitik olarak etkinlik gösteren NO_x yükseltgeme/depolama malzemeleri elde edilmiştir. Bu malzemeler üç ayrı grup halinde hazırlanmış ve incelenmiştir.

İlk grup numuneler, aktif katalizör olan titanyanın yüksek yüzey alanlı bir alttaş (destek) malzemesi (Al_2O_3) üzerine yayılması yolu ile hazırlanmıştır. "Sol-jel birlikte çöktürme metodu" ile 0.25, 0.5 ve 1.0 TiO_2:Al_2O_3 mol oranına sahip olacak şekilde TiO_2-Al_2O_3 karışık oksitleri sentezlenmiş, ardından bu numuneler X-ışını kırınımı, Raman spektroskopisi ve BET metodlarıyla karakterize edilmiştir. Bu numunelerin yüzey alanı, kalsinasyon sıcaklığı ve içerdikleri TiO_2 kristal yapısı gibi özelliklerinin NO_x yükseltgeme/depolama tepkimesi üzerindeki etkileri incelenmiştir.

Bir sonraki aşamada alkali/toprak alkali oksit NO_x depolama bileşenleri TiO_2-Al_2O_3 karışık oksitine eklenmiş ve bu katkılandırma iki farklı şekilde yapılmıştır. İlk yöntemde, TiO_2-Al_2O_3 üzerine "ıslak emdirme" metodu ile kütlece %5 veya 10 metal nitrat tuzları eklenmiş ve oluşan malzemenin kalsine edilmesiyle alkali/toprak alkali metal oksit oluşumu hedeflenmiştir. Diğer yöntemde ise TiO_2-Al_2O_3 karışık oksiti, kütlece %5 veya 10 BaO kristali ile beraber fiziksel olarak ezilerek toz kaline getirilmiş ve üçlü bir karışım elde edilmiştir. Bu numunelerde, NO_x depolama bileşeninin katkılandırılma metodu (ıslak emdirme ya da fiziksel karışım), eklenen metal oksit çeşitleri ve metal oksit yükleme yüzdesinin (kütlece %5 veya %10) NO_x yükseltgeme/depolama tepkimesi üzerindeki etkileri incelenmiştir.

Bahsedilen numunelerin fotokatalitik etkinliği ve verimi, kurduğumuz sürekli akış sistemi ile test edilmiştir. Bu sistem, kütle akış kontrolörleri, özel tasarım UVA-aydınlatmalı fotokatalitik reaksiyon hücresi ve oda koşulu kimyasal ışıldama NO_x analizöründen oluşmaktadır. Degussa P25 tüm testlerde referans malzeme olarak kullanılmıştır. Fotokatalitik performans deneyleri sonucunda TiO_2-Al_2O_3 karışık oksitlerinin NO_x depolama verimlerinin Degussa P25'e kıyasla çok daha yüksek olduğu görülmüş; bu ikili oksitlere fiziksel karışım metoduyla BaO depolama bileşeni eklenmesinin ise katı fazda NO_x depolanmasını kat kat arttırdığı ve gaz fazda NO_2 salınımını yok denecek seviyede tuttuğu anlaşılmıştır. Buna karşılık, "ıslak emdirme" yönteminin TiO_2-Al_2O_3 karışık oksidi üzerinde metal titanat ($M_xTi_yO_z$) türleri oluşumuna yol açtığı ve bu durumun da katalizörün foto-yükseltgeme yeteneğini oldukça azalttığı gözlemlenmiştir.

Anahtar Kelimeler: Hava arıtımı, Fotokatalitik NO_x Yükseltgenmesi/Depolanması, TiO_2, $DeNO_x$

ACKNOWLEDGEMENT

First of all, I would like to express my deepest graditude to my supervisor, Asst. Prof. Emrah Özensoy, who gave me the opportunity to work with him in the field of environmental remediation. This thesis could not have been written without his patient guidance, encouragement and understanding.

I would like to offer my special thanks to Prof. Ömer Dağ and Prof. Deniz Üner for fruitful discussions on this research work, and I am also thankful to Asst. Prof. Özgür Birer for his help on the Diffuse Reflactance UV-VIS measurements.

Special thanks should also be given to our collaborators from Greece, Prof. Christos Trapalis and Dr. Tatiana Giannokopoulou for their valuable guidance in this project, and I greatly appreciated their warm hospitability throughout my visit to N.C.S.R. Demokritos, Athens.

I would like to extend my heartfelt gratitude to our technician Ethem Anber for his help during the construction of the photoctalytic flow reactor system in our laboratory.

I owe sincere and earnest thankfulness to Evgeny Vovk, Zafer Say and Merve Doğaç for their partnership and help during this research and I would also like to thank Seda Şentürk, Emre Emmez, Emrah Parmak and all of the members of our research group for their kind help and friendship.

I would like to thank all past and present members of Chemistry Department where I have learned a lot in the last 7 years. My special thanks go to Övgü Yılmaz and Zeynep Ayça Bölükoğlu who have been a source of continuous joy and motivation throughout this period.

I also wish to acknowledge the financial support provided by the Scientific and Technical Research Council of Turkey (TUBITAK) (Project Code: 109M713).

Last but not the least, I am truly indebted to my parents, my brother, and to Cemal Albayrak for their endless love and encouragement. Words alone cannot describe how grateful I am to have such a caring family... I would be lost without them in this important time of my life and I am eternally grateful for their continuous support.

Finally, this acknowledgement would not have been complete without mentioning Deniz Aksoy, who had always challenged and inspired me to learn more and reach for more than I have ever felt capable of achieving. He was always there for me through good and bad, he never hesitated to lend a hand whenever needed and always cheered me up with his upbeat attitude... Now, all that I can do is to wish that he were here and we could be together once more, but in the end, I know that *the ones that love us never truly leave us*.

This thesis is dedicated to the loving memory of *Deniz…*

TABLE OF CONTENTS

LIST OF FIGURES

LIST OF TABLES

1. INTRODUCTION

1.1 Overview

Atmospheric pollution is a major problem brought on by industrialization and urbanization, and many forms of air pollution disturb the delicate balance of life on earth. The eventual damage is not just on the environment but also on the human health, which is heavily at risk in polluted areas. The contaminants that generate air pollution are emitted from many diverse sources. While *biogenic emissions* (such as microbial breakdown of organic materials) and emissions coming from nonliving *natural sources* (such as volcanic eruptions) have some impact on the deterioration of atmospheric contaminant levels, it should be noted that the *anthropogenic emissions* that occur as a result of human activity remains as the main source of air pollution [1].

The contaminants that cause air pollution are basically divided into two subcategories; primary pollutants and secondary pollutants[1]. Primary pollutants are the ones that are directly released into the atmosphere and they can be listed as such:

- Sulfur Dioxide (SO_2), produced from fossil fuel combustion at power plants (73%) and other industrial facilities (20%) [2].
- Nitrogen Oxides (NO_x), produced by emissions from cars, trucks and buses, power plants, and off-road equipment [3].
- Carbon Monoxide (CO), the majority of which comes from mobile sources [4].
- Volatile Organic Compounds (VOCs), emitted from a wide range of sources, including fossil fuel combustion, industrial activities, and natural emissions from vegetation and fires [1].
- Suspended particulate matter (SPM), a complex mixture of extremely small particles and liquid droplets, produced by organic chemicals, acids (such as nitrates and sulfates), metals, soil or dust particles [5].
- Toxic metals (Pb, Cd, Hg etc.), introduced through petrol, paints, batteries, hair dye products etc. [6]

In the atmosphere, these primary pollutants may combine to form bigger molecules or they may break down by photolysis / thermal decomposition to produce lighter chemicals. These chemicals are known as *secondary pollutants* and one of the most destructive products of such reactions is “ground-level” ozone (O_3). O_3 is highly oxidative and toxic for both humans and vegetation [1]. It should be stated that although the ozone in the stratosphere has a critical role in protecting life by constituting a UV-shield against the sun (Figure 1 [7]), ground-level ozone is designated as the “bad” ozone since it is a major component of smog, which is harmful to the respiratory system, especially in children [8].

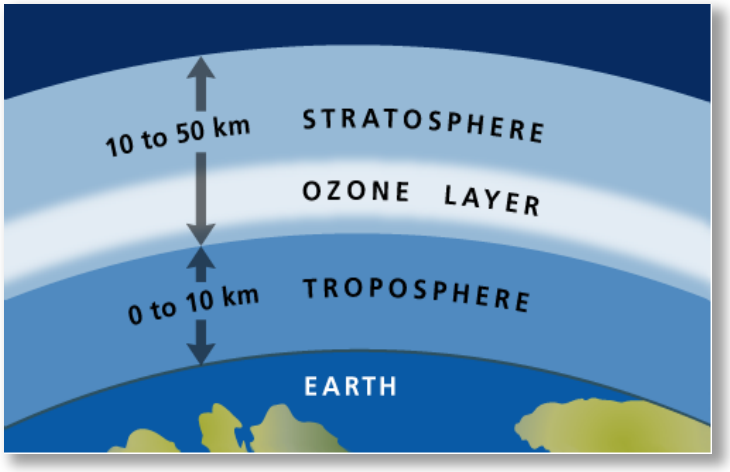

Figure 1. The ozone layer within stratosphere [7].

In United States, the *Clean Air Act* requires Environmental Protection Agency (EPA) to set National Ambient Air Quality Standards for six common air pollutants [9]. These commonly found pollutants (also known as "*criteria pollutants*") are particle pollution, ground-level ozone, carbon monoxide, sulfur oxides, nitrogen oxides and lead. In Turkey, Ministry of Health is responsible for monitoring air pollution levels. A total of 171 monitoring stations are distributed among 69 city centers and these stations continously measure SO_2 and particulate matter (PM) levels. In particular, Ankara-Sıhhiye station also monitors carbon monoxide (CO) and NO_x emissions [10].

Listed above among the primary air pollutants, gaseous nitrogen oxides (NO_x, such as NO and NO_2) are a group of highly reactive gases. According to the U.S. Environmental Protection Agency (EPA) Clean Air Act, having high levels of NO_x in the atmosphere leads to some major environmental and health-related problems. Some of these problems can be described as photochemical smog generation and toxic solid particulate formation with sizes less than 2.5 micron. Formation of ground level ozone (a detrimental secondary pollutant) is another consequence of high NO_x levels in the atmosphere, because $CO_{(g)}$ or short-lived VOCs react with NO_x and produce tropospheric ozone in polluted environments [1]:

$$VOC + OH\bullet \rightarrow HO_2\bullet + \text{other products} \quad (1\text{-a})$$

$$CO + OH\bullet \rightarrow HO_2\bullet + CO_2 \quad (1\text{-b})$$

$$HO_2\bullet + NO \rightarrow OH\bullet + NO_2 \quad (2)$$

$$NO_2 + h\nu\ (\lambda < 440\ nm) \rightarrow NO + O\bullet \quad (3)$$

$$O\bullet + O_2 + M \rightarrow O_3 + M \quad (4)$$

Along with producing "bad" ozone in troposphere, high concentrations of NO_x derivatives at the upper levels of the atmosphere results in the depletion of "good" ozone in stratosphere, thus impairing the UV-shield of Earth with the following reactions [11]:

$$NO + O_3 \rightarrow NO_2 + O_2 \quad (5)$$

$$NO_2 + O \rightarrow NO + O_2 \quad (6)$$

$$O + O_3 \rightarrow 2\ O_2 \quad (7)$$

NO_x species also contribute to acid rains by reacting with water vapor and some other air pollutants such as SO_2. Last but not the least, having relatively large heat capacities compared to other atmospheric gases (such as CO_2), NO_x species play a role in global warming, as well.

1.1.1 Effects of Indoor NO_x Pollution on Human Health

The general population gets exposed to nitrogen oxides primarily by breathing, however, combustion sources (such as coal burning power plants) or areas with heavy motor vehicle use pose a threat of higher NO_x exposure to people who live nearby. Furthermore, gas stoves and heating appliances which use wood and kerosene as fuel, produce more nitrogen oxide as compared to other alternatives. Finally, tobacco smoke contains nitric oxide (NO) and nitrogen dioxide (NO_2), so people who smoke or breathe in second-hand smoke may be exposed to higher levels of NO_x [12].

The most common manifestations of low level NO_x (<50 ppm) exposure are pulmonary symptoms such as cough, dyspnea (labored breathing), chest tightness/pain, choking, wheezing or rales. Other acute symptoms may include irritation of mucous membranes (including the eyes), light-headedness, agitation/confusion, weakness, fatigue, nausea, abdominal pain and even loss of consciousness [13] . Exposure to low levels can also result in fluid build-up in the lungs (pulmonary edema), 1 or 2 days after exposure [12].

Breathing high leves of NO_x (>100 ppm) however immediately causes rapid burning, spasms, swelling of tissues in the throat/upper respiratory tract, reduced oxygenation of body tissues, build up of fluid in lungs and in more serious cases death [12].

It should be noted that although nitric oxide (NO) constitutes the major portion of atmospheric NO_x, it reacts readily with oxygen to form NO_2, which is even more toxic than NO and can be a source of acute lung injury with pneumonitis and fulminant pulmonary edema, even at low doses [14]. The pulmonary injury related specifically to NO_2 exposure occurs as a result of NO_2 conversion to HNO_3 (nitric acid) and HNO_2 (nitrous acid) in the distal airways where type 1 pneumocytes and ciliated airway cells are directly affected. NO_2 initiates free radical generation in terminal bronchioles which results in protein oxidation, lipid peroxidation and subsequent cell membrane damage. Macrophage and immune function is also altered by NO_2, causing impaired resistance to infection [13].

Apart from these direct effects, NO_x species also react with ammonia, moisture, and other compounds to form small particles (<2.5 μm) in the air and while the *primary particles* are emitted directly from a source (such as construction sites, unpaved roads, fields, fires, etc.), these nitrogen oxide related particules (formed in atmospheric reactions) are known as *secondary particles* and they make up most of the fine particle pollution [5].

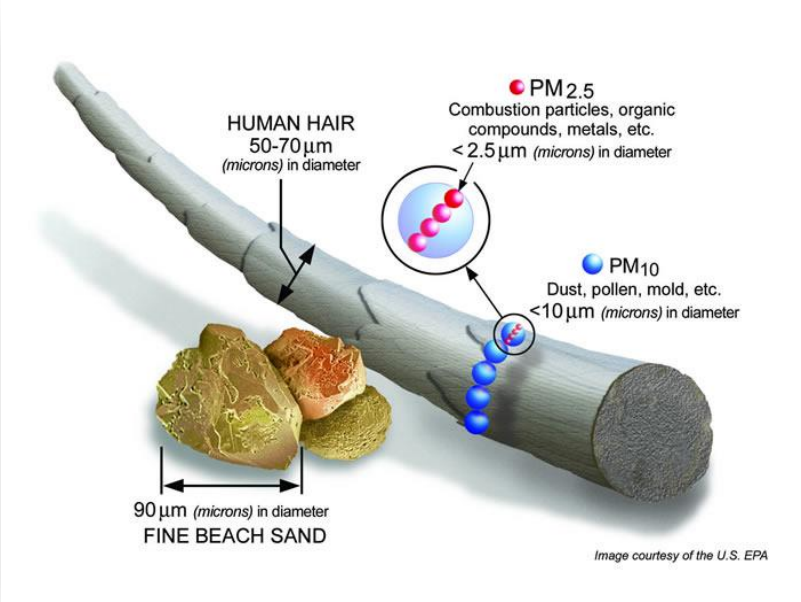

Figure 2. Size comparison for particulate matter pollutants [5].

These fine particles are especially pernicious since they are absorbed deeply into the lungs and even into the bloodstream. Exposure to particle pollution triggers a variety of problems, including [5]:

- premature death in people with heart or lung disease,
- nonfatal heart attacks,
- irregular heartbeat,
- aggravated asthma,
- decreased lung function,
- increased respiratory symptoms, such as irritation of the airways, coughing or difficulty breathing.

Another subsidiary damage of NO_x on human health comes from its role in the generation of ground level ozone, a highly toxic compound. Breathing in ozone has some deleterious consequences, including chest pain, coughing, throat irritation, and congestion. It can aggravate bronchitis, emphysema, asthma and chronic exposure to ozone carries the risk of permanent scarring to lung tissue [8].

The first and foremost stage of combatting NO_x related health-problems is to reduce the *production* of nitric oxides and since a large amount of the NO_x emission occurs as an outcome of fuel oil combustion in motor vehicles [15], the prevention of noxious emission from the automobile engines is necessary. Several approaches for NO_x abatement have been tried in automotive catalyst industry and some of these methods shall be discussed in the next section.

1.1.2 Catalytic Control of NO_x Pollution

In 1952, Haagen-Smit formulated the relationship between atmospheric NO_x species and the formation of photochemical smog in Los Angeles [16], since then there has been an ever increasing interest on the control of NO_x emissions. In United States, the first regulations on NO_x emission came in late 1969 and they were enacted in California by the local "Air Pollution Control District" [17]. In 1991, Environmental Protection Agency (EPA) has published *Tier 1* standards for light-duty vehicles in the U.S. and these rules were progressively introduced between 1994-1997. Then, in 1999, more stringent *Tier 2* standards were adopted to be phased in between 2004-2009 and this set of standards also brought in additional changes for larger vehicles. Finally, *Tier 4* standards are designed for 2008-2015 and these regulations require the emission of NO_x to be reduced by about 90% compared to *Tier 2* standards, down to 0.40 g/kW-h [18].

Similarly, Europe is also taking its measures against NO_x emissions and EURO 6 AECC regulations (Emission Control Technologies and Euro 5/6 Emission Legislation) state that by the end of 2014, diesel engines should not emit more than 0.08 g of NO_x per km travelled [19]. Table 1 shows the evolution of standard

regulation of atmospheric pollutants from both gasoline and diesel engines in the European Community [18]:

Table 1. Standard regulation of atmospheric pollutants from mobile sources in the European Community (1993-2014) [18]

	gasoline engine			
standard regulation [a]	CO	HC	NO_x	HC +NO_x
Euro 1 (1993)	2.72			0.97
Euro 2 (1996)	2.20			0.5
Euro 3 (2000)	2.30	0.20	0.15	
Euro 4 (2005)	1.00	0.10	0.08	
Euro 5 (2009)	1.00	0.10	0.06	
Euro 6 (2014)	1.00	0.10	0.06	

[a] Measured from New European Driving Cycle (g/km)

	diesel engine			
standard regulation [a]	CO	NO_x	HC +NO_x	particulates
Euro 1 (1993)	2.72		0.97	0.14
Euro 2 (1996)	1.00		0.90	0.10
Euro 3 (2000)	0.64	0.50	0.56	0.05
Euro 4 (2005)	0.50	0.25	0.30	0.025
Euro 5 (2009)	0.50	0.18	0.25	0.005
Euro 6 (2014)	0.50	0.08	0.17	0.005

[a] Measured from New European Driving Cycle (g/km)

In order to meet up with the expectations of these demanding regulations, the automotive catalyst industry has come up with several solutions to limit the pollutant emissions. Three of such important and widely used technologies can be listed as:

- Three-Way Catalysts (TWC)
- Selective Catalytic Reduction (SCR)
- NO_x Storage/Reduction (NSR)

Most of the commercially available Three-way catalysts (TWCs) contain noble metals (such as Pt/Rh and/or Pd/Rh) dispersed on a washcoat made up of Al_2O_3, CeO_2, ZrO_2, CaO, MgO and La_2O_3 [20]. As the name implies, TWCs enable the removal of three different post-combustion products (NO_x, CO and hydrocarbons) in three concurrent reactions: the reduction of nitrogen oxides (NO_x) to N_2 and O_2, the oxidation of carbon monoxide (CO) to carbon dioxide (CO_2) and the oxidation of unburned hydrocarbons (HC) to CO_2 and H_2O .

$$2NO_x \rightarrow xO_2 + N_2 \quad (8)$$

$$2CO + O_2 \rightarrow 2CO_2 \quad (9)$$

$$C_xH_{2x+2} + [(3x+1)/2]O_2 \rightarrow xCO_2 + (x+1)H_2O \quad (10)$$

The efficiencies of these reactions depend critically on the air to fuel ratio of the engine and TWCs perform best in the conventional gasoline engines where the A/F is around 14.5:1 [21].

Consequently, for *lean burn engines* where the A/F is around 25:1, TWCs do not work effectively, hence another catalytic conversion technology was required for NO_x abatement in high air to fuel ratios. Selective Catalytic Reduction (SCR) is one of these methods and it uses either ammonia (NH_3) or urea ($(NH_2)_2CO$) as the selective reductant to reduce the NO_x in the following reactions [15]:

$$4NH_3 + 4NO + O_2 \rightarrow 4N_2 + 6H_2O \quad (11)$$

$$4NH_3 + 2NO + 2NO_2 \rightarrow 4N_2 + 6H_2O \quad (12)$$

However, SCR also includes many competitive and nonselective reactions with oxygen and may produce secondary emissions, such as N_2O, NO, NH_4NO_3, NH_4-NO_2, NH_4HSO_4, and $(NH_4)_2SO$. Among these secondary emissions, ammonium nitrate (NH_4NO_3) has a tendency to form at low temperatures and is explosive. This product may also deposit in the pores of the catalyst, rendering it temporarily deactivated. Furthermore, sulfur in the diesel fuel leads up to the formation of SO_2 and SO_3 in oxidative conditions and NH_3 can combine with these products to form ammonium sulfates, which accumulate and cause irreversible damage on the

catalytic units. Besides, NH_3 (necessary for SCR) itself is toxic, corrosive, difficult to handle and a primary/secondary pollutant on its own. Urea has also various significant limitations as a reducing agent in SCR applications, such as its relatively high freezing point (-11^oC), which makes it unacceptable in winter conditions for several countries. [15].

Another catalytic conversion technology proposed for the lean-burn engines is the NO_x Storage-Reduction (NSR) method, also known as the Lean NO_x Trap (LNT). This system works under alternating fuel lean and fuel rich periods, during which NO_x is oxidized/stored and reduced consecutively. In the lean period (60-120 sec), the major component of NO_x in the diesel exhaust, NO, is oxidized over a precious metal (such as Pt, Pd and/or Rh) and the product NO_2 is captured on a storage component (such as BaO, K_2O etc.) in the nitrate (NO_3^-) form (Figure 3a) [21]. In the shorter rich period (5-15 sec) these nitrates are reduced into $N_{2(g)}$ and $O_{2(g)}$ while the unburned hydrocarbons are oxidized to $CO_{2(g)}$ and $H_2O_{(g)}$. The catalyst is regenerated by the end of the rich period and the storage sites are ready for the next lean period [21] (Figure 3-b).

$$NO \xrightarrow[Pt]{O_2} NO_2 \xrightarrow[Ba]{O_2} Ba(NO_3)_2 \qquad (13)$$

$$Ba(NO_3)_2 \xrightarrow{HC,\ H_2,\ CO} BaO + NO_2 \xrightarrow[Pt]{HC,\ H_2,\ CO} N_2+CO_2+H_2O \qquad (14)$$

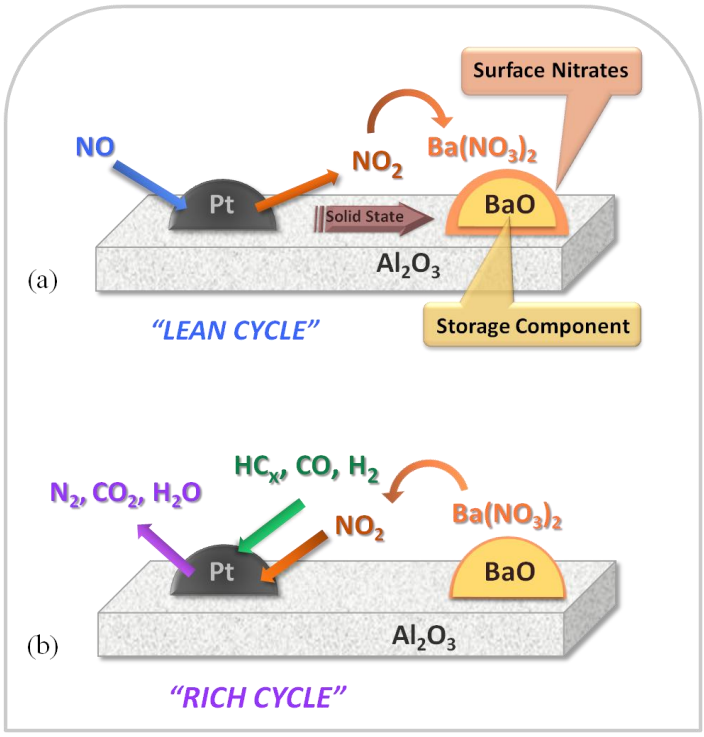

Figure 3. Illustration of the general operational principle of NSR catalyst during (a) lean cycle, (b) rich cycle.

Nevertheless, NSR catalysts have serious limitations as well, such as a high affinity towards sulfur compounds in the exhaust fume, which are adsorbed on the storage sites as sulfates and block those sites for NO_2 adsorption. Unfortunately, this binding is rather irreversible since the decomposition of sulfates requires higher temperatures than that is needed for nitrates. This poisoning occurs as a result of the higher thermodynamic stability of the sulfate species compared to the corresponding nitrates [15].

Many different types of catalytic converters in motor vehicle engines work for the same important aim; to reduce the emissions of NO_x into the atmosphere. Unfortunately, these systems cannot completely eradicate NO_x pollution and still we have nitric oxides in the air in spite of all these efforts. In the U.S., EPA has set National Ambient Air Quality Standards (NAAQS) for NO_2 and according to these standards, the hourly average for NO_2 should not exceed 0.100 ppm while the yearly average limit is set to an even lower value of 0.053 ppm [22].

In order to assess the air quality, EPA has also developed the color coded Air Quality Index (AQI) System, as shown in Table 2 below [22]. The level needed to violate the federal health standard for any pollutant corresponds to an AQI of 100 for that pollutant. Thus for NO_2, an AQI of 100 corresponds 0.053 ppm (averaged over 24 hours) while an index value of 201 corresponds to an NO_2 level of 0.650 ppm (averaged over 24 hours). After this point (0.650 ppm), one starts to experience the short-term health effects for NO_2.

Table 2. Air quality index (AQI) for Nitrogen Dioxide [22].

EPA Air Quality Index (NO_2)	**Levels of Health Concern**	**Cautionary Statements**
0 - 50	Good	None
51 - 100	Moderate	None
101 - 150	Unhealthy for Sensitive Groups	None
151 - 200	Unhealthy	None
201 - 300	Very Unhealthy	Children and people with respiratory disease, such as asthma, should limit heavy outdoor exertion.
301 - 500	Hazardous	Children and people with respiratory disease, such as asthma, should limit moderate or heavy outdoor exertion.

In cities with high air pollution, the hourly NO_x levels can climb up to 0.320 ppm near motorways during the rush hours [23]. Hence comes the second stage of combatting NO_x related health-problems, which is to reduce the levels of *atmospheric* NO_x. This aim, however, has to be realized at ambient conditions (at RT and under regular atmospheric conditions), since $NO_{x(g)}$ as a post-combustion product has left the automobile engine and is in the atmosphere at this point.

For this aim, *photocatalytic systems* can be proposed as a promising solution since they can be tailored to efficiently clean/purify air under ambient conditions with the help of ultraviolet (UV) and/or visible (VIS) light. In search of the perfect photocatalyst, titanium dioxide (TiO_2) has been studied extensively by many researchers since Fujishima and Honda demonstrated the semiconductor capabilites of rutile TiO_2 in water-splitting reaction in 1972 [24].

1.2 Physical Properties of Titania

Photocatalytic activity of titanium dioxide depends critically on its degree of surface crystallinity [25], therefore it is very important to know the properties of TiO_2 crystalline phases. Under normal atmospheric pressures, titanium dioxide has three polymorphs; rutile (stable), anatase (metastable) and brookite (metastable). Although other high-pressure phases of TiO_2 are also reported (such as; TiO_2-II [Srilankite], cubic fluorite-type, pyrite-type, monoclinic baddeleyite-type, cottunnite-type polymorphs [26]), these phases are of little importance for the photocatalytic research & development platform and they will not be further explored in this thesis.

In terms of abundancy among the TiO_2 polymorphs, anatase and rutile phases are significantly more common compared to the rarely found brookite, and although brookite also shows photoactivity [27-29], the field of photocatalysis is focused almost completely on anatase and rutile crystalline phases, making these former two polymorphs much more important in their photocatalytic applications compared to brookite.

Regarding the bulk thermodynamic stability, rutile is the more stable polymorph at all temperatures/pressures up to 60 kbar, where TiO_2-II becomes the thermodynamically stable phase [30]. Under ambient conditions, there is a small difference in the Gibbs free energy of formation between the bulk forms of these three polymorphs of TiO_2 (4-20 kJ/mol), suggesting that anatase and brookite are almost as stable as rutile under conventional temperatures and pressures. However, at elevated temperatures, anatase is transformed into rutile and thermodynamic studies show that negative pressures are required for the Gibbs free energy of anatase to be

lower than that of rutile (Figure 4), thus the transformation of anatase to rutile is irreversible [26].

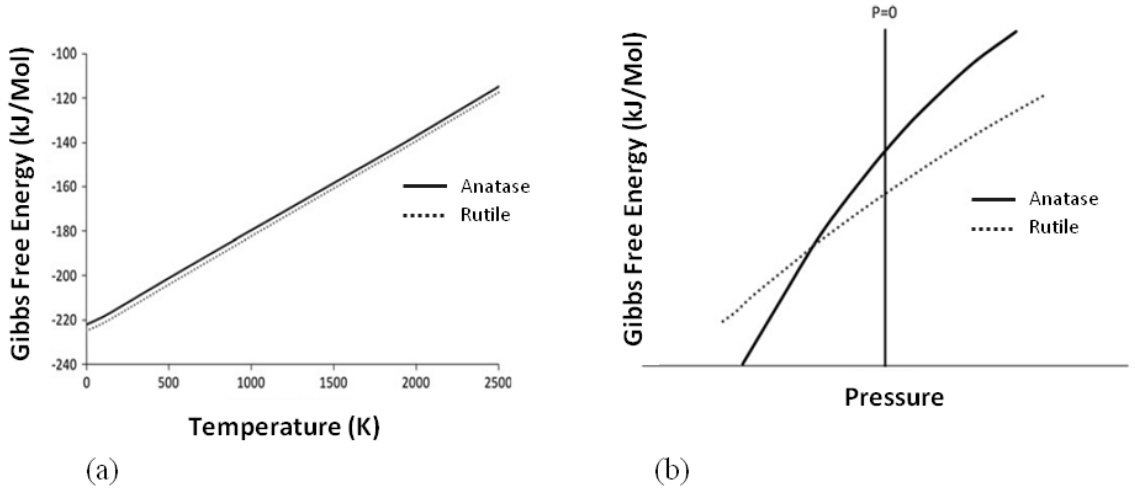

Figure 4. (a) Bulk Gibbs free energy of formation vs. temperature and (b) bulk Gibbs free energy of formation vs. pressure for anatase for anatase and rutile phases. [26]

It should be noted that due to surface free energy and surface stress effects, the relative stability of TiO_2 polymorphs may be reversed when the particle size decreases. At normal temperature and pressure, anatase is the most thermodynamically stable crystal structure for a particle size less than 11 nm, while between 11-35 nm, brookite presents the highest stability and for a particle size greater than 35 nm, rutile is the most stable phase [30].

Some of the fundamental properties of anatase and rutile are given below in Table 3 [26]:

Table 3. Properties of the anatase and rutile phases [26].

Property	**Anatase**	**Rutile**
Crystal Structure	Tetragonal	Tetragonal
Atoms per unit cell	4	2

Property	Anatase	Rutile
Space group	$I\,4_1/amd$	$P\,4_2/mnm$
Lattice parameters (nm)	a= 0.378 b= 0.951	a= 0.459 b= 0.296
Density (g/cm^3)	3.89	4.25
Calculated indirect band gap (eV) (nm)	3.23-3.59 345.4 – 383.9	3.02-3.24 382.7 – 410.1
Experimental band gap (eV) (nm)	~3.2 ~387	~3.0 ~413
Refractive Index	2.54	2.79
Hardness (Mohs)	5.5-6	6-6.5
Bulk Modulus (GPa)	183	206

1.2.1 The Crystal Structure of Titania

In both anatase and rutile, the crystal structure contains chains of *TiO_6 octahedra* where each Ti^{4+} is surrounded by six O^{2-} ions. However these crystal structures differ from one another by how the octahedra is distorted and how the octahedra chains are assembled in each case. In rutile, the distortion of the octahedra is slightly orthorhombic; yet in anatase, TiO_6 octahedron is significantly distorted and its symmetry is even lower than orthorhombic. Again in rutile, an octahedron is surrounded by 10 neighboring octahedra (two shared edges and eight shared corners), while in anatase each octahedron has eight neighbors (four shared edges and four shared corners), as depicted in Figure 5.

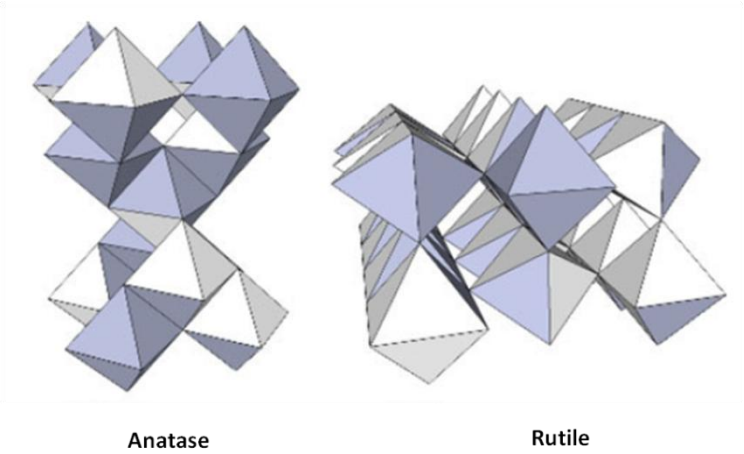

Figure 5. Three-dimensional representation of the octahedral arrengement in anatase and rutile phases of titania [26].

Also in anatase, Ti-Ti distances are larger compared to rutile (0.378 and 0.304 nm in anatase vs. 0.357 and 0.296 nm in rutile), but on the other hand, Ti-O distances are shorter in anatase (0.193 and 0.198 nm in anatase vs. 0.195 and 0.198 nm in rutile) [31]. Electronic band structures and mass densities of each polymorph is affected by these variations in their respective lattice structures.

1.2.2 Anatase to Rutile Phase Transformation

The formation of either anatase or rutile crystalline phase during TiO_2 synthesis depends primarily on the synthesis route and synthetic parameters. However, in general *anatase* forms as the initial crystalline TiO_2 phase for many of the synthesis protocols that take place at low temperatures, and the rutile phase is typically observed at elevated temperatures. [26]. This phenomenon can be explained from a thermodynamic point of view via Ostwald's step rule which states that "*the first phase to form will be the one possessing the least surface energy with respect to the reactants*" [32]. Therefore, the relatively lower surface free energy of anatase may lead to the rapid crystallization of this phase instead of rutile, although the Gibbs free energy of formation for bulk rutile is lower. Another explanation can be proposed from a structural perspective, the relatively less-constrained (and less dense) molecular structure of the anatase may be easier to be rearranged from the titanium-oxygen lattice of the amorphous reactants [32].

That being said, rutile can also be crystallized at low temperatures using hydrothermal methods, during which titania is precipitated directly from a liquid phase. However apart from this technique, high-temperature treatment is the most common way to obtain rutile crystals. Table 4 outlines various synthesis methods and the resultant phases of TiO_2 [26].

Table 4. Common synthesis methods of titanium dioxide and resultant phases (Amorph: Amorphous, A: Anatase, R: Rutile) [26]

Synthesis Method	**Mechanism**	**Phases formed**			
		Amorph	**A**	**R**	**A+R**
Room Temp. hydrolysis of $TiCl_4$	Precipitation from room temperature solutions of $TiCl_4$	✓			
Room Temp. sol-gel synthesis	Hydrolysis of $TiCl_4$ or an organometallic compound	✓			
Flame pyrolysis of $TiCl_4$	Combustion of $TiCl_4$ with oxygen; used in industrial processes		✓		✓
Synthesis Method	**Mechanism**	**Phases formed**			
		Amorph	**A**	**R**	**A+R**
Solvothermal/ Hydrothermal	Precipitation of TiO_2 from an aqueous or organic solution at elevated temperatures		✓	✓	✓
Chemical Vapor Deposisiton (CVD)	Spraying of Ti-bearing solution	✓	✓	✓	✓
Physical Vapor Deposition (PVD)	Deposition of evaporated Ti and its subsequent oxidation	✓	✓	✓	✓

The anatase to rutile transition (referred also as the ART) is a reconstructive process and in pure anatase, rutile may start nucleation at (112) twin interfaces of anatase, because these sites are structurally similar to rutile [33, 34]. In the transformation product, the (112) planes of anatase are kept as the newly formed (100) rutile planes [26] and an overall volume contraction (c.a. 8%) is observed as the c-axis is contracted during the process [35, 36]. Higher mass density of the rutile phase is explained by this decrease in the volume.

The ART is both temperature and time dependant, and several factors play a role in the exact temperature that is required for the transition to start and the time for it to be completed. Such parameters for undoped anatase can be listed as;

- Particle size
- Particle shape (aspect ratio)
- Surface area
- Volume of sample
- Nature of sample container
- Impurities
- Heating rate
- Atmosphere

It is generally considered that pure bulk anatase starts to transform when it is heated around ~600^{o}C in air. Nonetheless, temperatures ranging from 400 to 1200^{o}C have been reported [35, 37, 38] for the ART, owing to the differences in the above-listed factors.

The kinetics of the anatase to rutile transition are also strongly dependent on the presence of *dopant atoms* which may either facilitate or hinder the ART [39]. In this regard, the resulting effect depends critically on the *size*, the *valence* and the *content* of the dopant. For cationic dopants, cations with smaller radii and lower valence (<4) are known to promote the transition while cations with larger radii and higher valence (>4) can inhibit it [26].

Since the oxygen sublattice determines the structural stability of anatase and the reorganization of the bonds *en route* to the rutile formation, the transition is largely affected by the changes in the oxygen sublattice. If a cation with low valence substitutes a $Ti^{4+,}$ site, an increase in the oxygen vacancies is observed to obtain charge neutrality; this can facilitate the rutile transition. If, however, a cation with higher valence is substituted for a Ti^{4+}, then this requires the annihilation of the existing oxygen vacancies, which impedes the rutile transition.

Figure 6 shows a plot of the inhibiting and promoting dopant atoms. [26].

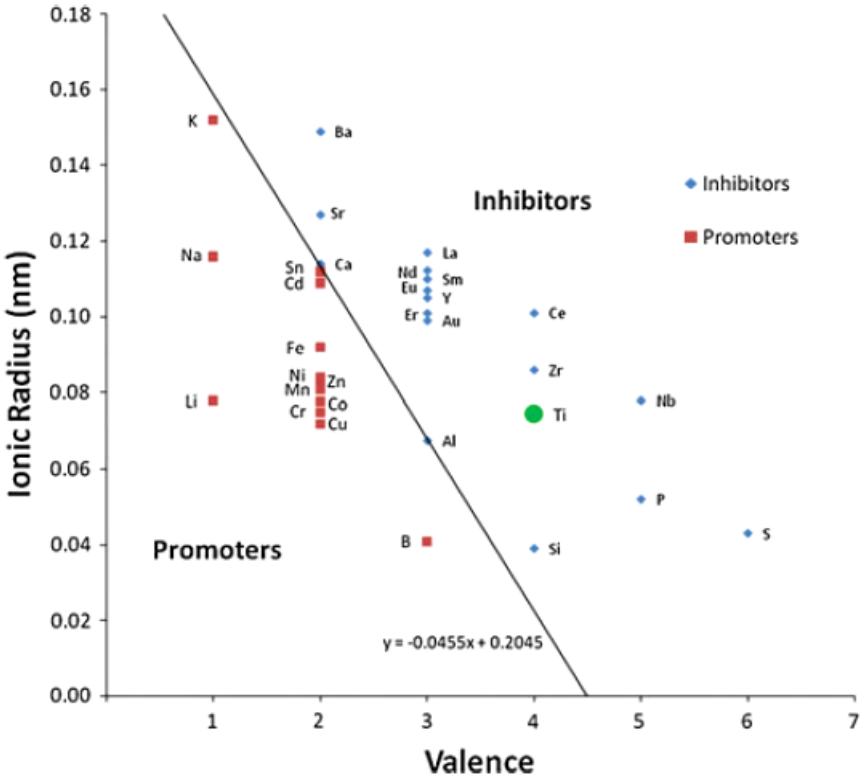

Figure 6. Plot of cationic dopant types, on account of their ionic radii and valence, categorized by their anatase-to-rutile transition inhibitive or promoting effect [26].

The effects of anionic dopant addition on the anatase-to-rutile transition is not very well known in the literature, however with a similar reasoning, it may be argued that the anionic dopants that can fill in the oxygen vacancies (such as F^- [40] or N^{3-} [41]) might increase the structural stability and inhibit the phase transformation [26].

1.2.3 Electronic Band Structure of Titania

In a semiconductor, the valence band (VB) and the conduction band (CB) are separated with a small yet non-zero band gap (E_g). The range for the VB-CB seperation lies between 0 to 4.0 eV for a semiconductor [42] and accordingly, titania is classified as a semiconductor.

The density of states (DOS) of TiO_2 consists of Ti e_g, Ti t_{2g} (d_{xz}, d_{yz} and d_{xy}), O p_σ and O p_π. The upper valence band is composed of three main regions; the lower energy σ bonding region (mainly contributed by O p_σ), the middle energy π bonding region and the high energy O p_π states. These O p_π states at the top of the valence band are non-bonding, since here the hybridization with Ti-d states is almost negligible. [43, 44]. On the other side, the conduction band can be decomposed into two regions; Ti e_g (> 5eV) and and Ti t_{2g} (< 5eV) bands. In anatase, the main peak of t_{2g} band is idenfied to be mostly d_{xz}+d_{yz} states (antibonding π*) and the nonbonding d_{xy} state lies at the bottom of the conduction band. Figure 7 shows the DOS of anatase TiO_2 structure and its derived molecular orbital diagram [43].

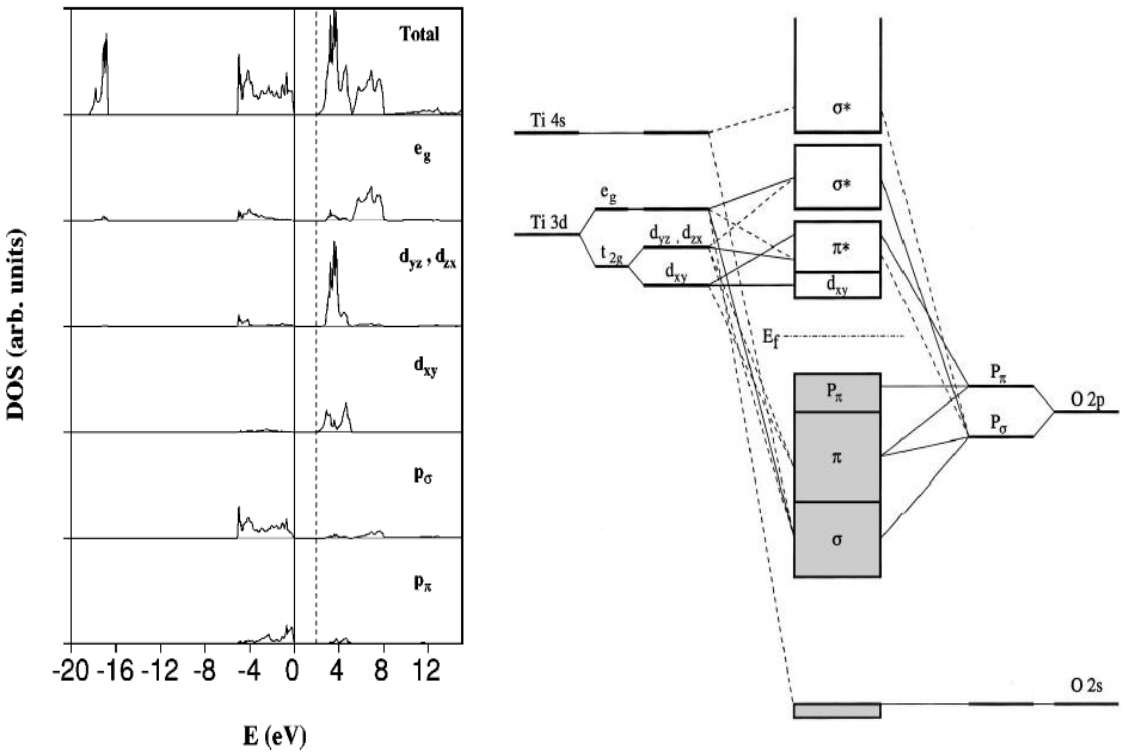

Figure 7. (a) Total and projected densities of states (DOS) of the anatase TiO_2 structure (b) Molecular-orbital bonding structure for anatase TiO_2 [43]

For the rutile, a *nonbonding* d_{xy} feature is less significant, because rutile phase is denser than anatase and has smaller Ti-Ti distances, so the t_{2g} orbitals at the bottom of the conduction band provide metal-metal interactions and lie lower than in the case of anatase [43, 44]. As a result of this, rutile has a smaller gap between its valence and conduction bands. Figure 8 gives a comparison of the calculated electronic density of states (DOS) for bulk rutile and anatase structures [45].

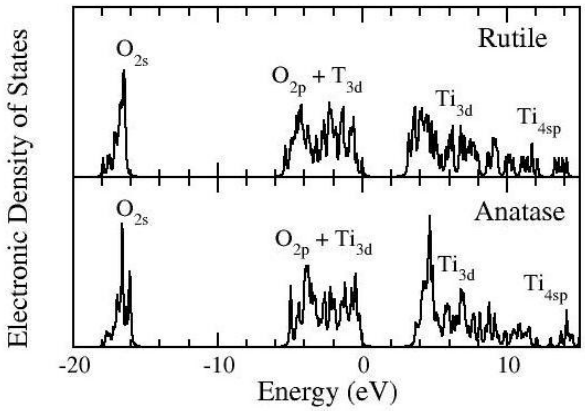

Figure 8. Electronic density of states for bulk rutile (upper panel) and anatase (lower panel) phases. The valence band maximum is taken as the zero of energy [45]

In bulk limit, it is both experimentally determined and theoretically calculated that anatase has an *indirect* band gap of ~3.2 eV while rutile has a *direct* band gap around 3.0 eV [25, 26, 30, 43, 46, 47]. Kavan et al. [48] experimentally showed that the difference between the band gap of anatase and rutile phases occurs mainly as a result of the change in the position of the conduction band edge, and the CB edge for anatase lies ~0.2 eV higher than that of rutile.

1.3 Photocatalysis on TiO_2-based materials

The principle of photocatalytic reactions on semiconductor surfaces can be described simply in the following way; if a photon with energy equal to or greater than the band gap energy ($h\nu \geq E_g$) of a semiconductor is absorbed by that material, a valence band electron (e^-_{VB}) is excited to the conduction band, leaving a positively charged hole (h^+) behind and this process creates an electron-hole pair.

These pairs, also known as the charge-carriers, diffuse to the surface of the material and there, they react with the surface-adsorbed species and decompose them [44, 46].

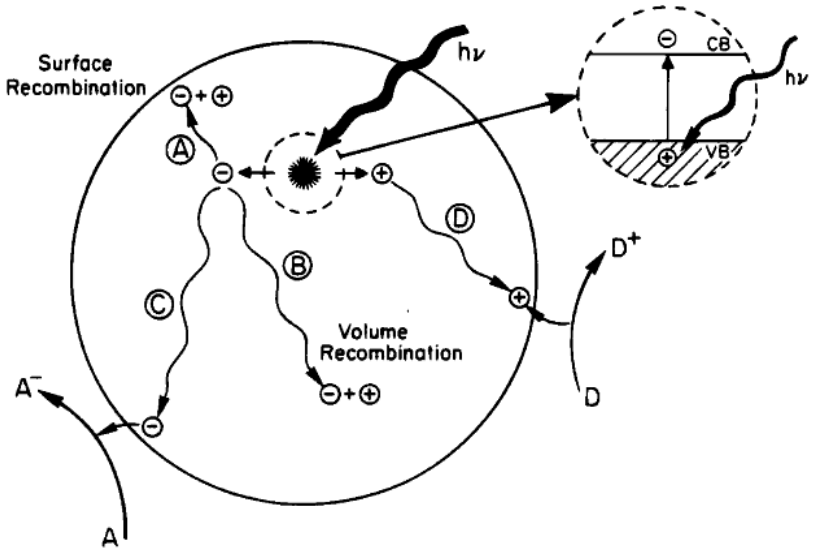

Figure 9. Schematic view of the photoexcitation and the following deexcitation events [46].

After the initial excitation, the electron-hole pair may reach different outcomes under different circumstances. The photoinduced electron may migrate to the semiconductor surface and reduce an electron acceptor, which is generally oxygen in aerated conditions (Figure 9, Pathway C). The hole, on the other hand, can also migrate to the surface and combine with an electron of a donor species (such as H_2O or OH^-), oxidizing the donor in turn (Figure 9, Pathway D). However, rather than undergoing such charge-transfer processes, the electron-hole pair may recombine / annihilate each other and this recombination event may take place either on the surface of the semiconductor (Figure 9, Pathway A) or inside the bulk of the material (Figure 9, Pathway B) [46].

The efficiency of a photocatalytic reaction is measured in terms of *quantum yield*, a quantity which is calculated by the number of a specific event occuring per photon absorbed. Since it is very difficult to measure the actual amount of photons absorbed, all the light that is sent to the surface is assumed to be absorbed, an the

quantum yield calculated in this way is named the "apparent quantum yield" [46]. Electron-hole recombinations decrease the quantum yield and so the efficiency of the photocatalysis depends on the recombination rate in the semiconductor.

Bulk and surface irregularities/defects usually act as charge-carrier traps and affect the recombination rate, however the effect of such carrier traps on the photocatalytic efficiency is much debated [25]; these traps may be beneficial if they promote charge-carrier separation by stabilizing the seperated e^-/h^+ pair. In this case, trapping helps to retard the recombination event, which in turn increases the photocatalytic efficiency [46]. Another advantage may be if the charge-traps localize charge carriers at TiO_2 surfaces where the electron transfer takes place. On the other hand, trapping can be disadvantageous when the charge carriers are trapped far from the preferred electron transfer sites or if they recombine in these trapping sites [25].

The quantum yield (or photonic efficiency) is also greatly influenced by the irradiation type and source. In order to provide the energy required for the excitation of a semiconductor, various types of electromagnetic radiation (Table 5) can be used, depending on the bandgap of the photocatalyst [42]. Table 6 gives the bandgap energies for different semiconductors [42].

Table 5. Excitation energy types used in photo-processes [42].

Type of EM radiation	Wavelength (nm)	Energy (eV)
Vacuum UV (VUV)	100-200	12.4 – 6.2
UV-C	200-280	6.2 – 4.4
UV-B	280-315	4.4 – 3.9
UV-A	315-380	3.9 – 3.3
Visible Light	380-780	3.3 – 1.6

Table 6. Bandgap energies (eV) of various semiconductors and their respective colors [42].

Semiconductor	E_g (eV)	Color
Cu_2O	2.2	Red
CdS	2.4	Yellow
Bi_2O_3	2.7	Yellow
TiO_2 (rutile)	3.0	White
TiO_2 (anatase)	3.2	White
ZnO	3.2	White
SnO_2	3.8	Grey

Having a bandgap of at least 3.0 eV (Rutile), pure TiO_2 can be excited with the high energy portion of the visible light or better with a UV-A source. Also, being relatively cheap, stable and non-toxic, TiO_2 is preferred as a photocatalyst in a multitude of applications, ranging from energy technologies such as hydrogen generation [24, 49, 50] and dye-sensitized solar cells [51, 52] to air and water purification [53-57], as well as self-cleaning tiles [58], non-spotting glasses[59] and self-sterilizing (anti-bacterial) coatings [60, 61].

Anatase and rutile phases of TiO_2 are both commonly used as photocatalysts and in the literature, there is a general perception that anatase is inherently more photoreactive than rutile [25, 30, 46, 62]. It has been suggested that this increased photoreactivity of anatase is due to its slightly higher Fermi level and higher degree of hydroxylation (number of hydroxyl groups on the surface) [62-64]. However, this perception on the anatase photoreactivity may also be a result of its higher relative surface area compared to rutile. It is not easy to compare the activities of titania polymorphs with different surface areas. Recent generation of rutile nanoparticles with particle sizes smaller than 10 nm facilitated a direct comparison between anatase and rutile nanoparticles. Interestingly, many studies showed that these rutile

nanoparticles have comparable or even higher photoreactivities than anatase nanoparticles of similar size [25].

Apart from the debate on anatase vs. rutile activity, it is also argued in the literature that a mixture of anatase and rutile is even more photoactive than either of these phases [65, 66]. This statement is especially true for the behavior of Degussa P25, a commercial TiO_2 photocatalyst that is used as the "gold-standard" in the TiO_2-based photocatalysis research against which the efficiencies of other TiO_2 photocatalysts are frequently reported. Degussa P25 is a composite mixture of TiO_2 nanopowder, comprising of ~85% anatase and ~15% rutile phases (by mass), whose enhanced activity is generally conceived as a result of the interfacial properties between anatase and rutile [25]. It has been shown that in such mixed-phase TiO_2 specimens, the anatase and rutile particles must be in chemical contact for an enhanced photoreactivity effect to be observed. The need for chemical contact has been generally explained by the slightly different band-edge positions of anatase and rutile phases. According to this explanation, there is a possibility for a hetero-junction to form between these two phases where electron transfer can take place. In this sense, an interface between anatase and rutile can increase the efficiency of charge ($e^- - h^+$) separation, although the nature of atomic contact that facilitates this charge separation is not completely understood [25].

1.3.1 Photocatalytic Oxidation (PCO) on TiO_2-based materials

Photocatalytic oxidation (PCO) has drawn much attention in the field of air and water purification, as an attractive alternative to the conventional purification methods, such as carbon adsorption, incineration and catalytic oxidation [67]. PCO is consired to be more advantageous compared to the competing technologies, due to its following properties: (1) Low-concentration and low-flow rate waste streams can be oxidized at ambient temperatures and pressures; (2) PCO systems can easily be operated (instant on/off), modulated, and transported; (3) Hydrocarbons can completely be mineralized (4) PCO by-products of oxygenates are amenable to bio-

remediation; (5) Solar energy can be utilized with semiconductor particles (e.g. TiO_2) with a mechanism similar to photosynthesis in green plants [67].

As explained earlier in Chapter 1.3, PCO on TiO_2 surfaces is based on the excitation of the semiconductor with photons ($h\nu \geq E_g$), the subsequent removal of an e^- from the valence band (VB) to the conduction band (CB) and the creation of a hole (h^+) back in the VB. The redox potential for a valence-band hole is +2.53 eV with respect to the standard hydrogen electrode (SHE) in pH 7 solution (Figure 10), meaning that the photoinduced h^+ is highly oxidizing [68].

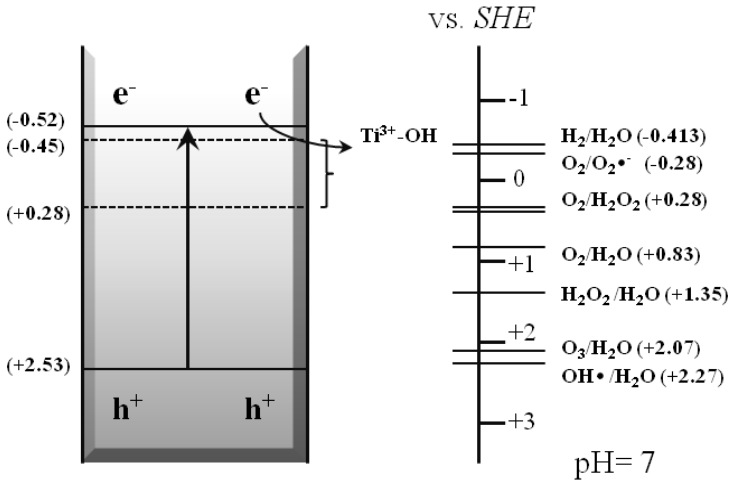

Figure 10. The potentials for various redox processes occurring on the TiO_2 surface at pH 7 [68].

The generated h^+ can be transferred to the TiO_2 surface and oxidize an adsorbate, generating *a singly oxidized* electron donor, whilst the excited e^- can diffuse to the surface, reduce an adsorbate, forming *a singly reduced* electron acceptor [47].

$$TiO_2 + h\nu \rightarrow TiO_2\,(e^-, h^+) \quad (15)$$

$$TiO_2\,(h^+) + RX_{ads} \rightarrow TiO_2 + RX_{ads}^{\bullet +} \quad (16)$$

$$TiO_2\,(h^+) + H_2O_{ads} \rightarrow TiO_2 + OH_{ads}^{\bullet} + H^+ \quad (17)$$

$$TiO_2\,(h^+) + OH_{ads}^- \rightarrow TiO_2 + OH_{ads}^{\bullet} \quad (18)$$

$$TiO_2\,(e^-) + O_{2,ads} \rightarrow TiO_2 + O_2^{\bullet -} \quad (19)$$

$$TiO_2\,(e^-) + H_2O_{2,ads} \rightarrow TiO_2 + OH^- + OH_{ads}^{\bullet} \quad (20)$$

Equations 14-19 give examplary reactions that can occur on the TiO_2 surface and show the formation of anionic/cationic radicals that can undergo further redox reactions. An oxidation reaction on TiO_2 may be a direct oxidation via the highly oxidative valence-band holes (h^+), or it can happen indirectly via the surface generated hydroxyl ($OH^\bullet$) or superoxide radicals ($O_2^{\bullet -}$). [25].

The generated hydroxyl radical ($OH^\bullet$) is considered to be one of the the most important species in the photocatalytic oxidation/degredation of organic pollutants. There is not a consensus on the common pathway of $OH^\bullet$ generation, but it is generally thought to form via direct (h^+) capture by the *adsorbed* OH^- species, rather than through water, whose radical-cation ($H_2O^{\bullet +}$) can be neutralized before decomposing into $OH^\bullet$ [47]. In any case, since TiO_2 surface is assumed to be covered with OH^- to a certain extent, the hole is most probably transferred directly to OH_{ads}^- [47].

The electron scavenger in the system can be any species whose electron affinity is higher than that of an e^- trap site in TiO_2, and that being said, molecular oxygen is the most common electron scavenger on TiO_2 surfaces [25]. The reduction potential of oxygen in inert solvents is almost isoenergetic with the conduction band of TiO_2 (Figure 10, [68]), thus the photogenerated electrons are efficiently trapped by the adsorbed oxygen [47]. The reduction of oxygen results in the formation of superoxide radicals ($O_2^{\bullet -}$), which are highly reactive and can readily attack other adsorbed molecules. The photocatalytic activity of TiO_2 has been observed to be completely suppressed without an electron scavenger, such as oxygen [47].

An immense variety of reactants can undergo oxidation/degredation on the TiO_2 surface and many have been explored extensively in the literature. Although the PCO reactant list is rather lengthy, it can be divided into the following subgroups; carbon monoxide, carboxylic acids (e.g. formic acid, acetic acid), alcohols (e.g. methanol, ethanol, isopropanol), aldehydes (e.g. acetaldehyde), ketones (e.g. acetone), alkanes (e.g. methane, propane, cyclohexane), alkenes (e.g. ethylene, propylene, isobutene), aromatics (e.g. benzene, toluene, naphthelene), halocarbons (e.g. carbontetrachloride, trichloroethylene, fluoro-, bromo-, iodo-hydrocarbons), nitrogen containing molecules (e.g. nitric oxide, ammonia, cyanide, alkylamines), organophosphorus and organosulfide compounds [25, 47].

Photocatalytic oxidation rate of these chemicals is affected by several operational parameters in both solution and gas-phase reactions. The following chapter explores these factors in more detail.

1.3.1.1 Operational parameters in Photocatalytic Oxidation Experiments

The photooxidation/degradation rate on TiO_2 surface is dictated by the following parameters [30]:

- Catalyst loading,
- Chemical structure and the initial concentration of the target compound,
- Temperature,
- UV light intensity,
- Oxygen concentration,
- Presence of supplementary oxidizable substances,
- Circulating flow rate,
- pH for aqueous treatments,
- Water concentration for gaseous phases.

Four of these main factors are discussed below.

(a) Catalyst Loading

For solution phase reactions, an increase in the catalyst loading generally results in a subsequent improvement in the decomposition rate, since higher surface area of the catalyst is available for adsorption and degradation. However, there exists an optimum loading value, above which the solution opacity increases unfavorably, leading to the reduction of light penetration in the solution [69, 70]. As a result, the oxidation rate diminishes. Furthermore, the following reactions may take place at high TiO_2 concentrations and cause further decrease in the photo-degradation rate, since the formed hydroperoxyl radical (HO_2•) is less reactive than OH• [30]:

$$H\bullet + OH\bullet \rightarrow H_2O_2 \quad (21)$$

$$H_2O_2 + OH\bullet \rightarrow H_2O + HO_2\bullet \quad (22)$$

For TiO_2 immobilized systems, there is also an optimal thickness for the catalyst film. Since the film is porous, the thickness of catalyst is proportional to the interfacial area and thus an increase in the film thickness can be conceived to favor catalytic oxidation. However, the internal mass transfer resistance for both photo-generated e^-/h^+ pairs and the organic species increases with increasing thickness. This enhances the recombination chance of the e^-/h^+ pair and, as a result, the degradation performance may be reduced [30].

(b) Temperature

Photocatalytic oxidation rate is known to be rather insensitive to minor changes in the temperature [71]. This phenomenon can be explained by the low thermal energy at room temperature (kT= 0.026 eV) that has almost no contribution to the activation energy of the wide bandgap TiO_2. However that being said, at higher temperatures, both substrates and intermediates desorb more rapidly from the catalyst, which leads to a larger effective surface area for the reaction. Also, the effect of temperature may be dominated by the rate of interfacial e^- transfer to oxygen [72]. Although at temperatures between 21 to 75^oC, the change in the relative position of the Fermi level in TiO_2 powders is reported to be relatively small, the interfacial electron-transfer kinetics is still improved at higher temperatures [73].

(c) Photon flux

Basically, two regimes govern the photocatalytic reaction with respect to the UV photon flux. A first-order regime is observed for fluxes up to about 25 mW/cm^2 in laboratory experiments and for higher intensities, a half-order regime is noted [30]. In the first-order regime, chemical reactions consume the e^-/h^+ pairs more rapidly than the recombination reactions, however in the half-order regime, the recombination rate is dominant [74-76].

(d) Oxygen pressure

Oxygen, as an electron scavenger, is essential for semiconductor photocatalytic oxidation of both organic compounds and nitric oxides. Since the dissolved molecular oxygen is strongly electrophilic, an increase in O_2 content probably hinders the unfavorable electron–hole recombination event [74]. Nevertheless, higher concentrations of O_2 can lower the reaction rate, if the TiO_2 surface becomes highly hydroxylated and the adsorption of pollutant at active sites is inhibited [77].

1.3.1.2 Photocatalytic Oxidation (PCO) of NO on TiO_2-based materials

NO_x pollution is controlled via two approaches; first, the NO_x species can be catalytically reduced to N_2 in the automotive converters or alternatively they can be photocatalytically oxidized to NO_2 and NO_3^- (HNO_3) on semiconductor surfaces. As an advantage of the second mechanism, the oxidation of $NO_{x(g)}$ to nitric acid completes the nitrogen fixation and in this way, a pollutant can be converted into a raw material for beneficial applications, such as fertilizers [78].

Many studies proposed photocatalytic oxidation mechanisms for NO_x oxidation over TiO_2 and the PCO reaction is generally considered to proceed through the following steps, *in the presence of water* [67, 79-82]:

(a) Adsorption of the involved gas species over the active sites of TiO_2:

$$O_2 + site \rightarrow O_{2\,ads} \quad (23)$$

$$H_2O + site \rightarrow H_2O_{ads} \quad (24)$$

$$NO + site \rightarrow NO_{ads} \quad (25)$$

$$NO_2 + site \rightarrow NO_{2\,ads} \quad (26)$$

(b) Activation of TiO_2 by generating holes and electrons:

$$TiO_2 + h\nu(\lambda < \sim 390\ nm) \rightarrow e^- + h^+ \quad (27)$$

(c) Trapping of holes by water and adsorbed OH^-:

$$h^+ + H_2O_{ads} \rightarrow OH\bullet + H^+ \quad (28)$$

$$h^+ + OH^-_{ads} \rightarrow OH\bullet \quad (29)$$

(d) Trapping of electron by oxygen:

$$e^- + O_{2\,ads} \rightarrow O_2\bullet^- \quad (30)$$

(e-1) Contaminants attacked by hydroxyl radical:

$$NO_{ads} + OH\bullet \rightarrow HNO_2 \quad (31)$$

$$HNO_2 + OH\bullet \rightarrow NO_{2\,ads} + H_2O \quad (32)$$

$$NO_{2\,ads} + OH\bullet \rightarrow NO_3^- + H^+ \quad (33)$$

(e-2) Contaminants attacked by oxygen radical:

$$NO + O_2\bullet^- \rightarrow NO_3^- \quad (34)$$

In this scheme, a photogenerated hydroxyl radical (OH•) attacks the adsorbed NO molecule and oxidizes it to HNO_2, which is later oxidized to NO_2 by another OH• radical. Finally, the adsorbed NO_2 is transformed to NO_3^- by another photogenerated hydroxyl radical, completing its oxidation. On another account, a NO molecule can directly be oxidized to nitrate upon reacting with a photogenerated superoxide ($O_2\bullet^-$) radical.

In 2006, using in-situ FTIR, Wu et al. have proposed an experimental mechanism for the adsorption of NO and its subsequent photocatalytic oxidation on TiO_2, *in the absence of water* [78]. In their experiments, the authors utilized zero-grade air and high-purity He as carries gases and passed them through a moisture-adsorbing material before the photoreactor. Then, in order to remove the trace water, they passed all gas (air, He, and NO mixture) through a cold trap (-75 to -95 ◦C). and finally, they thermally pretreated the catalyst sample inside the photoreactor under air flow and UV irradiation at 500^{o}C to remove residual hydrocarbons and water from the surface.

According to their observations, the adsorption of NO on TiO_2 results in the formation of NOH, bidentate nitrite, bidentate and monodentate nitrates, $TiOO^-$ and other surface peroxides (750–680 cm^{-1}). Apparently, adsorbed hydroperoxo (TiOOH) species are also generated during NO adsorption, and their absorption bands are observed at 870–770 cm^{-1}.

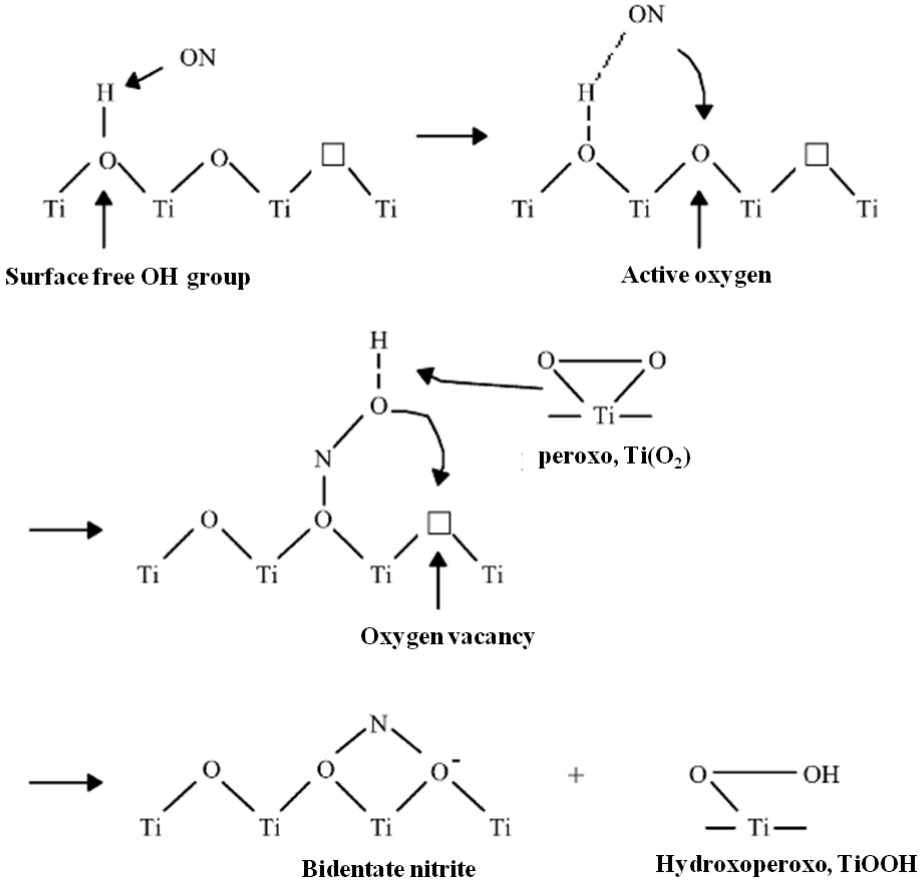

Figure 11. A possible mechanism of NO adsorption on TiO_2 [78].

In the scheme summarized in Figure 11, NO preferentially attacks surface free OH groups and then is oxidized to monodentate nitrite by an oxygen with unsaturated coordination (surface active oxygen). Next, an oxygen vacancy and surface peroxo species transform the monodentate nitrite into bidentate nitrite, and a hydroperoxo species is generated.

When the UV light is turned on, e^-/h^+ pairs are generated and the holes are trapped by surface *peroxo* species which are then oxidized to *superoxo* species. The adsorbed bidentate nitrite is oxidized to either monodentate or bidentate nitrate, upon reacting with these superoxo species (Figure 12). As a result, a rapid decrease in bidentate nitrite (1192 cm^{-1}) and an increase in monodentate and bidentate nitrates is observed within the first 3-10 s of UV irradiation. If the superoxo species do not come into contact with nitrites, then they are claimed to be further photooxidized to O_2 molecules, leaving oxygen vacancies.

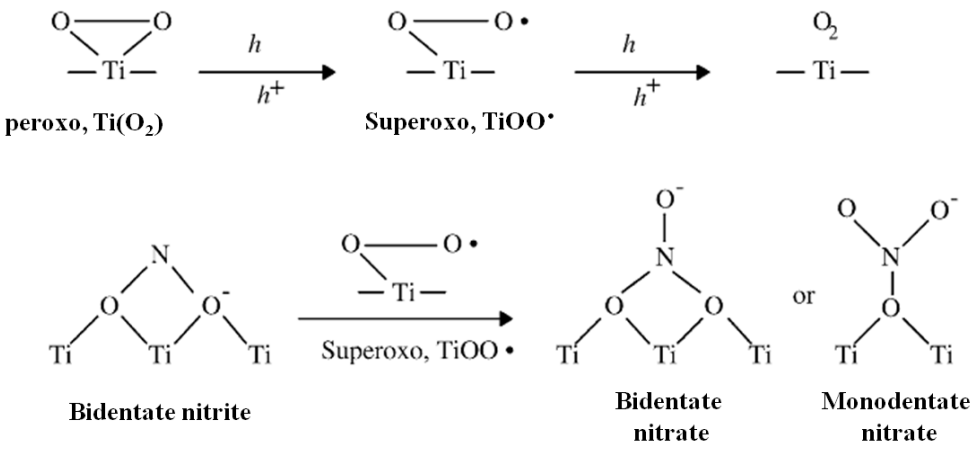

Figure 12. A possible mechanism of photocatalytic NO oxidation on TiO_2 [78].

Between 1-30 minutes of UV irradiation, bidentate nitrite signal is diminished and a decrease in surface peroxo species in the structure of $Ti(O_2)$ (at 1000-900 cm^{-1}) is also observed, while H-bonded OH groups peak at 3605 cm^{-1}. Finally, 5 h of UV irradiation further increases nitrates and decreases $Ti(O_2)$ and free OH groups (at 3727 cm^{-1}). Moreover after 5 h, the intensity of the peak at 3565 cm^{-1} increases, indicating a growing number of OH groups coupled by nitrates. It should be noted that during this time, the increase in nitrates and decrease in surface peroxo species occurs simultaneously [78].

1.3.1.3 Applications of Photocatalytic NO Oxidation on TiO_2-based materials

Each and every year, more TiO_2-based products are coming onto the stage and getting commercialized for NO_x abatement purposes. In Japan, traffic tunnels, paved roads and buildings have been coated with TiO_2-based materials to remove NO with photocatalytic oxidation [83]. Furthemore, Mitsubishi Materials Corporation has produced and commercialized a photocatalyticaly active pavement block (NOXer®), to remove atmospheric NO_x [84]. These blocks have been tested in Osaka and in Westminster borough of London [85].

In Italy, the *Italcementi* group has come up with a photocatalytic cement (TX Active ®) and has filed 12 patents on photocatalysis applied to cementitious materials [86]. Figure 13 shows a representation of photocatalytic air purification in urban areas, depicted by the *Italcementi* [87].

Figure 13. Representative drawing of photocatalytic air purification in urban areas, where (1) shows CO, VOC (Benzene, Toluene, etc.), Methyl Mercaptan(g), Organic chlorinated compounds, Polycondensed aromatic compounds, Acetaldehyde, Formaldehyde and (2) shows NO_x, SO_x, NH_3(g) [87].

In 2002, the TX Active ® cement have been tested against NO pollution in Milan, where a heavily trafficked bituminous road surface (a 230 m-long section with total a surface area of 7,000 m^2) was covered with a thin layer of photoactive TX Active® binder-based mortar [87]. The experiment was carried on for 9 months (November 2002-July 2003) during which the continuation of the tested road (featuring a traditional asphalt-treated pavement) was used as a reference. At the end of the testing period, the recorded data showed that compared to the untreated area, up to 60% NO_x abatement was achieved and the best results were obtained in summer with an average luminous intensity of about 90,000 Lux, a wind speed of approximately 0.7 m/s, an ambient temperature of 32°C, and 46% humidity [87].

In 2007, an international ISO working group has published the ISO22197-1 standard [88], titled as "Fine ceramics (advanced ceramics, advanced technical ceramics) - Test method for air purification performance of semiconducting photocatalytic materials. Part 1: Removal of nitric oxide". This standard was derived from the 2004 Japanese one (JIS R 1701-1), which was not developed specifically for cement-based materials. ISO22197-1 is applicable for materials that contain a photocatalyst or a photocatalytic film on the surface and specifies a test method for the determination of the air purification performance of these materials by continuous exposure of a test piece to the model air pollutant (NO) under 10 W/m^2 UV illumination. This standard can also be applied to materials in honey-comb form and to plastic or paper materials containing ceramic microcrystals and composites but is not suggested for powder or granular photocatalytic materials [88].

PCO applications also include indoor air cleaners and car deodorizers in which indoor VOCs and NO_x are oxidized over TiO_2 activated by sunlight or fluorescent light [30]. There is also a study where the TiO_2 activity is aimed to be improved by the addition of zeolites (A and Y), which concentrate NO on the surface [89].

1.4 Aim of the Study

In this work, a hybrid technology for the photocatalytic oxidation and storage of gas phase NO_x species is proposed and with this aim, the components of thermaly activated NO_x Storage- Reduction (NSR) system is combined with photocatalytically activated NO_x oxidation catalyst TiO_2, and a photocatalytically activated NO_x oxidation & storage (PhoNOS) material is obtained.

In this respect, a sol-gel synthesis route is employed to co-precipitate titania with alumina, a high surface area support material, in order to both *disperse the photocatalytically active titania* in an effective manner and to *increase the NO_x adsorption capacity* of the material. Next, an alkaline oxide storage component (e.g CaO, BaO, etc.), inspired from the NSR technology, is added to the TiO_2-Al_2O_3 mixture. In this system, the presence of oxygen, water and an excitation source will let the atmospheric NO_x to be oxidized on the surface of the photocatalyst and the gaseous oxidation products will be anchored on the adsorption-sites as solid nitrates, instead of being released back into the atmosphere (Figure x).

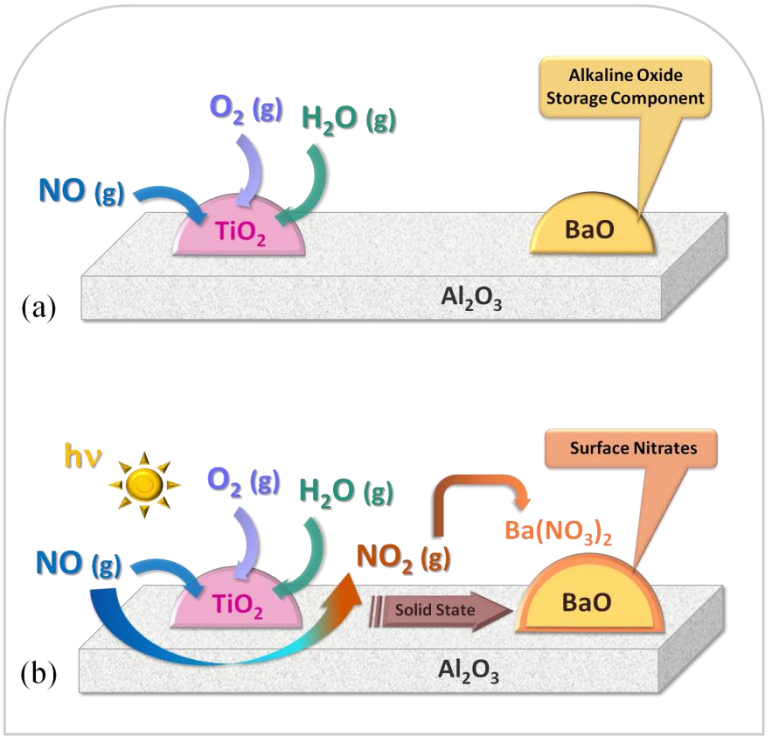

Figure 14. Schematic depiction of the photocatalytic NO_x oxidation and storage (PhoNOS) catalyst and the PhoNOS process.

These powders can be added into paints or coatings to be effectively used in atmospheric NO_x abatement and these products can be utilized either indoors or outdoors where they will continuously operate to oxidize and capture gaseous NO_x species. When the absorption sites are covered/saturated with nitrates, regeneration of the storage sites will be required which can be achieved by scrubbing with water. If the photocatalyst is used in an outdoor application (i.e. on the outer walls of the buildings, factories, or on the bridges and walls near heavy traffic areas), rain should wash out the nitrates and resurface the alkaline oxides. If, on the other hand, the photocatalyst is utilized inside a building, scrubbing the application area with a wet towel can be suggested to dissolve the accumulated nitrates and regenerate the absorbtion sites.

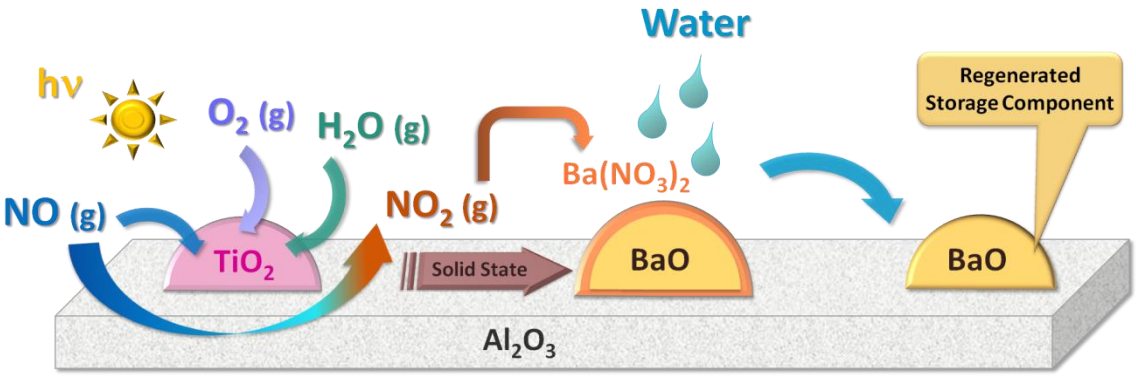

Figure 15. Schematic depiction of catalyst regeneration with water

The utilization of an alkali oxide component is very important in this concept, because although titania alone is very efficient in oxidizing NO, the reaction product gaseous NO_2, which is even more toxic than NO itself, is mostly released to the atmosphere as it cannot be captured by the surface effectively. In currently proposed photocatlytic system, however, both the oxidation of NO and the storage of NO_2 is achieved with a relatively higher efficiency and the decrease in the total NO_x concentration is significant compared to conventional titania photocatalysts.

2. EXPERIMENTAL

2.1. Sample preparation

2.1.1 Preparation of Sol-Gel TiO_2

For the synthesis of the sol-gel TiO_2, the following protocol was followed. 14.8 ml (of titanium(IV) isopropoxide (97 %, Sigma Aldrich) was mixed with 50 ml propan-2-ol (99.5 +%, Sigma Aldrich) and 1.6 ml acetylacetone (99.3 %, Fluka) for 30 min. This clear yellow solution was vigorously stirred at room temperature. The precipitation of the corresponding hydroxide was accomplished after the gradual addition of 6 ml of 0.5 M HNO_3 to the solution, which consecutively led to the formation of gel. The resulting yellow slurry was aged under ambient conditions for 3 days and then further dried at 60^{o}C for 48h. The dried sample was grinded to fine powder with a glass mortar. For further analysis of the obtained TiO_2, various annealing steps ranging from 150 to 1000^{o}C (2 h in air for each temperature) were performed as listed in Table 7.

Table 7. Calcination temperatures of the synthesized TiO_2 samples.

Calcination Temperature	**TiO_2 Sample Name**
RT	TiO_2-UNC
150 ^{o}C	TiO_2-150
350 ^{o}C	TiO_2-350
500 ^{o}C	TiO_2-500
600 ^{o}C	TiO_2-600
700 ^{o}C	TiO_2-700
800 ^{o}C	TiO_2-800
1000 ^{o}C	TiO_2-1000

2.1.2 Preparation of TiO_2/Al_2O_3 binary oxides

Binary oxide TiO_2/Al_2O_3 photocatalysts were prepared through a sol-gel route [90]. Three different set of samples were prepared in which TiO_2 to Al_2O_3 mol ratio was 0.25, 0.5 or 1.0. The binary oxide photocatalyst was prepared by the co-hydrolysis of titanium and aluminium alkoxides.

For the synthesis of the ***0.25 Ti/Al*** samples, the following protocol was followed. First, 12.4 g of aluminum *sec*-butoxide (97%, Sigma Aldrich) was mixed with 50 ml propan-2-ol (99.5 +%, Sigma Aldrich) and 1.6 ml acetylacetone (99.3 %, Fluka) for 30 min. Sequentially, 1.85 ml titanium(IV) isopropoxide (97 %, Sigma Aldrich) was added dropwise to the mixture that proceeded for another half an hour. All of the synthesis steps were carried out at room temperature under vigorous stirring. The co-precipitation of the corresponding hydroxides was accomplished after the gradual addition of 3.5 ml of 0.5 M HNO_3 to the solution which consecutively led to the formation of gel. The resulting yellow slurry was aged under ambient conditions for 2 days and the dried sample was ground to fine powder with a glass mortar . For further analysis of the obtained TiO_2/Al_2O_3 binary oxides, various calcination steps ranging from 150 to 1000^oC (2 h in air for each temperature) were performed.

A similar protocol was applied during the synthesis of the ***0.5 Ti/Al*** samples. Here, 12.4 g of aluminum *sec*-butoxide (97%, Sigma Aldrich) was mixed with 55 ml propan-2-ol (99.5 +%, Sigma Aldrich) and 1.6 ml acetylacetone (99.3 %, Fluka) for 30 min. Next, 4 ml titanium(IV) isopropoxide (97 %, Sigma Aldrich) was added dropwise to the mixture that proceeded for another half an hour. All of the synthesis steps were carried out at room temperature under vigorous stirring. The co-precipitation of the corresponding hydroxides was accomplished after the gradual addition of 5 ml of 0.5 M HNO_3 to the solution which consecutively led to the formation of gel. The resulting yellow slurry was aged under ambient conditions for 2 days and the dried sample was ground to obtain a fine powder using a glass mortar. For further analysis of the obtained TiO_2/Al_2O_3 binary oxides, various calcination steps ranging from 150 to 1000^oC (2 h in air for each temperature) were performed.

Finally, for the synthesis of ***1.0 Ti/Al*** samples the same protocol was applied with the following amount of ingredients: 12.4 g of aluminum *sec*-butoxide (97%, Sigma Aldrich), 60 ml propan-2-ol (99.5 +%, Sigma Aldrich), 1.6 ml acetylacetone (99.3 %, Fluka), 7.5 ml titanium(IV) isopropoxide (97 %, Sigma Aldrich) and 6 ml of 0.5 M HNO_3.

The compositions and calcination temperatures of these materials are listed in Table 8.

Table 8. Compositions and calcination temperatures of the synthesized TiO_2/Al_2O_3 binary oxides

	Ti/Al Mol Ratio		
Calcination Temperature	**0.25 Ti/Al**	**0.5 Ti/Al**	**1.0 Ti/Al**
RT	0.25 Ti/Al-UNC	0.5 Ti/Al-UNC	1.0 Ti/Al-UNC
150 °C	0.25 Ti/Al-150	0.5 Ti/Al-150	1.0 Ti/Al-150
350 °C	0.25 Ti/Al-350	0.5 Ti/Al-350	1.0 Ti/Al-350
600 °C	0.25 Ti/Al-600	0.5 Ti/Al-600	1.0 Ti/Al-600
800 °C	0.25 Ti/Al-800	0.5 Ti/Al-800	1.0 Ti/Al-800
900 °C	0.25 Ti/Al-900	0.5 Ti/Al-900	1.0 Ti/Al-900
950 °C	0.25 Ti/Al-950	-	-
1000 °C	0.25 Ti/Al-1000	0.5 Ti/Al-1000	1.0 Ti/Al-1000

2.1.3 Preparation of $M_xO/TiO_2/Al_2O_3$ Mixed Oxides via Impregnation

A set of NO_x oxidation/storage materials in the form of $M_xO/TiO_2/Al_2O_3$ were synthesized by conventional incipient wetness impregnation of the 0.5 and 1.0 TiO_2/Al_2O_3 binary oxide support materials. Here "M" denotes different Group IA (Li, Na, K, Cs) or Group IIA (Ca, Sr, Ba) metals, and x is 1 or 2 respectively. In order to obtain 5 wt% and 10 wt% M_xO loadings, TiAl were impregnated with aqueous solutions of these alkali/alkaline earth metals' nitrate salts. The synthesized materials ($M(NO_3)_x/TiO_2/Al_2O_3$) were then dried at 80^oC. Finally, the samples were calcined under $Ar_{(g)}$ atmosphere for 4 h at 700^oC before being inserted into the catalytic reactor for photocatalytic oxidation experiments. In the current text, synthesized NO_x oxidation/storage materials are denoted as xTiAl-T+yM (IM) (where x is the Ti:Al mole ratio, T is the calcination temperature (^oC) for TiAl binary oxide, y is metal oxide loading in terms of weight percent and IM is an abbreviation for "*Impregnation*"). The compositions and calcination temperatures of these materials are also listed in Tables 9 and 10.

Table 9. Compositions and calcination temperatures of the ternary oxide NO_x oxidation/storage materials, prepared from 0.5 TiO_2/Al_2O_3 via impregnation.

	Calcination Temperature		**Calcination Temperature**
Alkaline Earth Metal Addition 5 %	**900 ^oC**	**Alkaline Earth Metal Addition 10 %**	**900 ^oC**
Ba	0.5Ti/Al-900+5Ba (IM)	**Ba**	0.5Ti/Al-900+10Ba (IM)

Table 10. Compositions and calcination temperatures of the ternary oxide NO_x oxidation/storage materials, prepared from 1.0 TiO_2/Al_2O_3 via impregnation.

	Calcination Temperature			**Calcination Temperature**	
Alkali Metal Addition 5 %	**800 °C**	**900 °C**	**Alkali Metal Addition 10 %**	**800 °C**	**900 °C**
Li	1.0Ti/Al-800 +5Li (IM)	1.0Ti/Al-900 +5Li (IM)	**Li**	1.0Ti/Al-800 +10Li (IM)	1.0Ti/Al-900 +10Li (IM)
Na	1.0Ti/Al-800 +5Na (IM)	1.0Ti/Al-900 +5Na(IM)	**Na**	1.0Ti/Al-800 +10Na (IM)	1.0Ti/Al-900 +10Na (IM)
K	1.0Ti/Al-800 +5K (IM)	1.0Ti/Al-900 +5K (IM)	**K**	1.0Ti/Al-800 +10K (IM)	1.0Ti/Al-900 +10K (IM)
Cs	1.0Ti/Al-800 +5Cs (IM)	1.0Ti/Al-900 +5Cs (IM)	**Cs**	1.0Ti/Al-800 +10Cs (IM)	1.0Ti/Al-900 +10Cs (IM)
	Calcination Temperature			**Calcination Temperature**	
Alkaline Earth Metal Addition 5 %	**800 °C**	**900 °C**	**Alkaline Earth Metal Addition 10 %**	**800 °C**	**900 °C**
Ca	1.0Ti/Al-800 +5Ca (IM)	1.0Ti/Al-900 +5Ca (IM)	**Ca**	1.0Ti/Al-800 +10Ca (IM)	1.0Ti/Al-900 +10Ca (IM)
Sr	1.0Ti/Al-800 +5Sr (IM)	1.0Ti/Al-900 +5Sr (IM)	**Sr**	1.0Ti/Al-800 +10Sr (IM)	1.0Ti/Al-900 +10Sr (IM)
Ba	1.0Ti/Al-800 +5Ba (IM)	1.0Ti/Al-900 +5Ba (IM)	**Ba**	1.0Ti/Al-800 +10Ba (IM)	1.0Ti/Al-900 +10Ba (IM)

2.1.4 Preparation of $M_xO/TiO_2/Al_2O_3$ Mixed Oxides as a Physical Mixture (with Sol-Gel TiAl)

These set of samples are composed of the TiO_2-Al_2O_3 mixed oxides (prepared via the sol-gel route) and commercially available BaO (99.9 %, Sigma Aldrich) powder. The TiO_2-Al_2O_3 binary oxides with either 0.5 or 1.0 Ti/Al mol ratios were ground with 5 or 10% (w/w) BaO (s) with an agate mortar & pestle. The powders are thoroughly mixed for about 15 minutes and then the sample is used without further calcination. In the current text, these NO_x oxidation/storage materials are denoted as xTi/Al-T+yBaO (PM) (where x is the Ti:Al mole ratio, T is the calcination temperature (^oC) for Ti/Al binary oxide, y is BaO loading in terms of weight percent and PM is an abbreviation for "*Physical Mixture*")

Compositions of these materials are listed in Table 11.

Table 11. Compositions and calcination temperatures of the ternary oxide NO_x oxidation/storage materials, prepared from sol gel TiO_2/Al_2O_3 via physical mixing.

	Calcination Temperature			**Calcination Temperature**	
Alkaline Earth Metal Addition 5 %	**800 ^{o}C**	**900 ^{o}C**	**Alkaline Earth Metal Addition 10 %**	**800 ^{o}C**	**900 ^{o}C**
Ba	-	0.5Ti/Al-900 +5BaO (PM)	**Ba**	-	-
Ba	1.0Ti/Al-800 +5BaO (IM)	1.0Ti/Al-900 +5BaO (IM)	**Ba**	1Ti/Al-800 +10BaO (IM)	1.0Ti/Al-900 +10BaO (IM)

2.1.5 Preparation of TiO_2/γ-Al_2O_3 Mixed Oxide as a Physical Mixture (with Degussa P25)

Commercially avaiable Degussa P25 TiO_2 was physically mixed with commercially available γ-Al_2O_3 (PURALOX, 200 m^2/g, SASOL GmbH, Germany) powder, using an agate mortar and pestle. The powders are thoroughly mixed for about 15 minutes and the TiO_2 to Al_2O_3 mol ratio in the final mixture is 0.5. This sample is denoted as 0.5 P25 + γ-Al_2O_3.

2.1.6 Preparation of $M_xO/TiO_2/\gamma$-Al_2O_3 Mixed Oxide as a Physical Mixture (with Degussa P25)

Commercially avaiable Degussa P25 TiO_2 was physically mixed with commercially available γ-Al_2O_3 (PURALOX, 200 m^2/g, SASOL GmbH, Germany) powder, using an agate mortar & pestle. The powders are thoroughly mixed for about 15 minutes and the TiO_2 to Al_2O_3 mol ratio in the final mixture is designated to be 0.5. This P25+γ-Al_2O_3 physical mixture is then ground with 5 or 10% (w/w) commercially available BaO (99.9 %, Sigma Aldrich) powder in the agate mortar, and again, the mixing period is 15 minutes.

Compositions of these materials are listed below in Table 12.

Table 12. Compositions of the ternary oxide NO_x oxidation/storage materials, prepared from Degussa P25 via physical mixing.

Alkaline Earth Metal Addition 5 %	**0.5 Ti/Al**	**Alkaline Earth Metal Addition 10 %**	**0.5 Ti/Al**
Ba	0.5P25 + γ-Al_2O_3 +5BaO(PM)	**Ba**	0.5P25+ γ-Al_2O_3 +10BaO(PM)

2.2 Experimental set-up

2.2.1 Photocatalytic Flow Reactor set-up

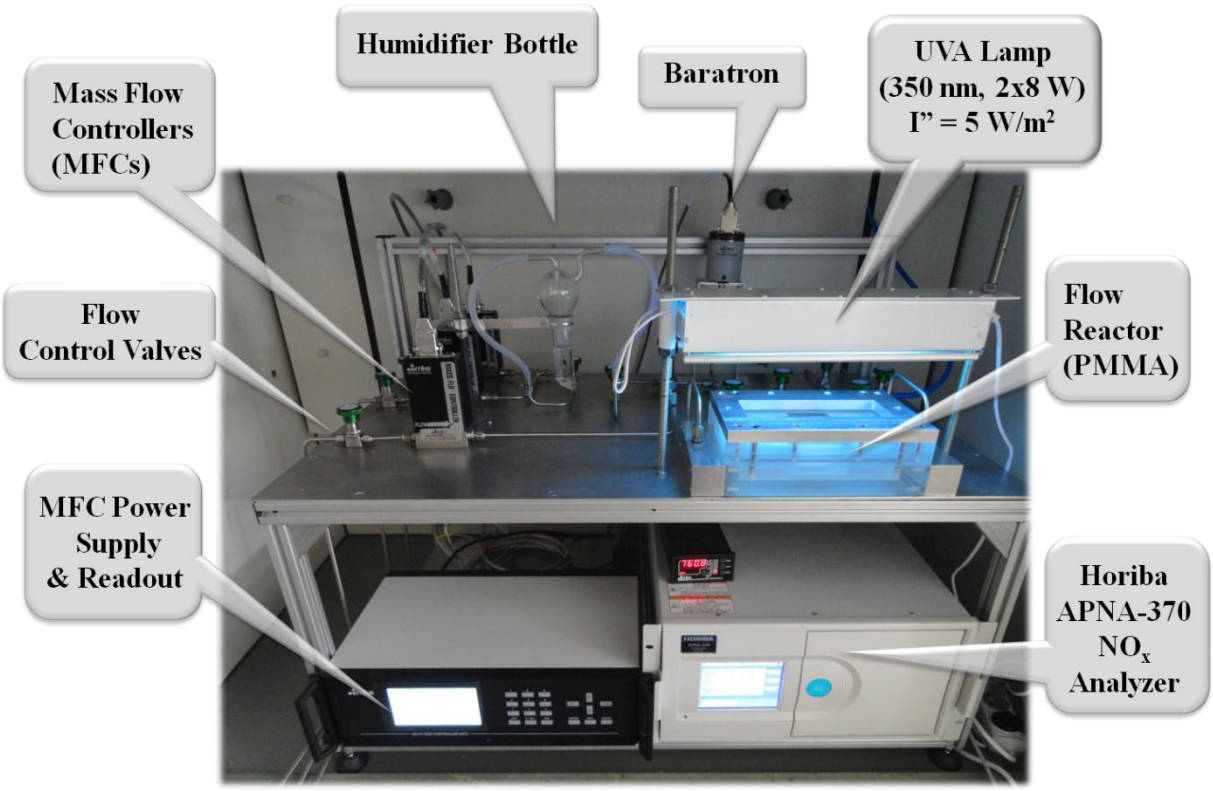

Figure 16. Components of the Photocatalytic Flow Reactor system, assembled and placed inside the fumehood.

The photocatalytic flow reactor set-up is shown in Figure 16. The custom designed flow reactor system is assembled with the aim of measuring the photocatalytic NO_x oxidation and storage performances of candidate photocatalysts under UVA exposure. The system consists of the following main sections: **(a)** High purity gases (Linde **(i)** 99.998% pure N_2 **(ii)** 99.998% pure O_2 and **(iii)** NO diluted in N_2 (100 ppm)) and gas regulators (Linde B5665) **(b)** Flow control valves (Swagelok, SS Bellows-Sealed Valve, SS-4H) **(c)** Mass flow controllers (*MFC*) calibrated for N_2 and O_2 gases [MKS, 1479A 01313CS1BM (1000 sccm N_2), 1479A 01321CS1BM (20 sccm N_2) and 1479A 01552CS1BM (500 sccm O_2)] **(d)** Power Supply and Readout for MFC units (MKS, 647C-4R1N) **(e)** Gas humidifier bottle **(f)** Pressure

gauge (Capacitance Manometer, MKS Baratron 626B13TBE) and its power supply/readout (PDR2000AO) **(g)** UVA Lamp (2 x 8W, F8W/T5/BL350, Sylvania) **(h)** Photoradiometer (HD 2302.0 - Delta OHM) and its UVA probe (LP471 UVA, DeltaOhm) **(i)** Photocatalytic Flow Reactor and **(j)** HORIBA APNA-370 Chemiluminescence Ambient NO_x Analyzer.

The whole apparatus is fixed on an aluminum profile (shown in Figure 17), whose dimensions are designed to fit inside a fumehood.

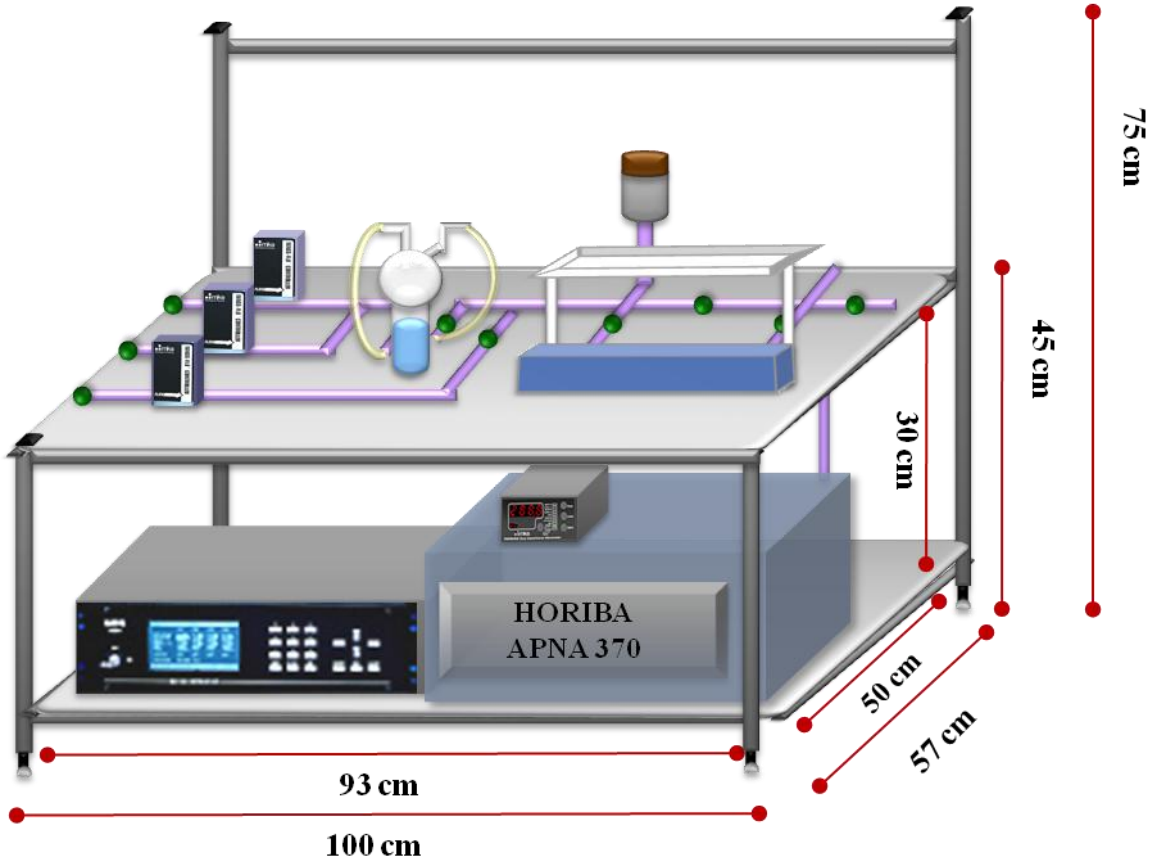

Figure 17. Simplified schematic of the Photocatalytic Flow Reactor system and dimensions of the aluminum profile.

2.2.1.1 Gas Manifold System

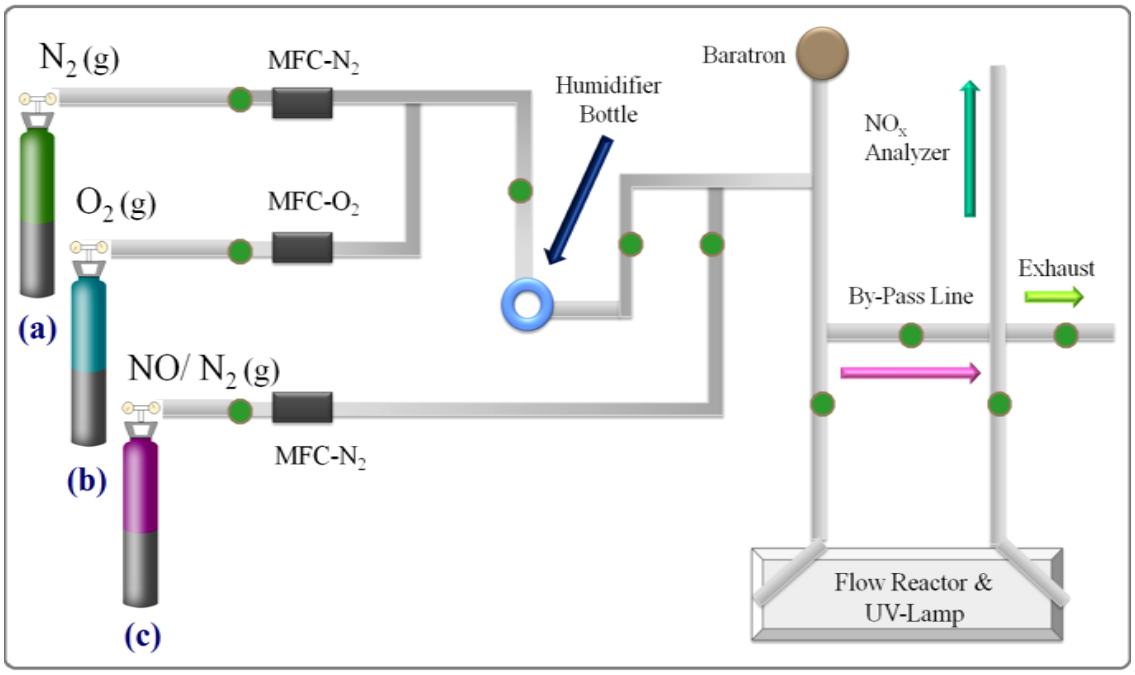

Figure 18. Schematic representation of the gas manifold system (topview).

The gas manifold system is shown schematically in Figure 18. The gas lines are Swagelok stainless steel tubings with an inner diameter of ¼ inch. They are connected to gas tanks of **(a)** 99.998% pure N_2 **(b)** 99.998% pure O_2 and **(c)** NO diluted in N_2 (100 ppm). As can be seen from Figure 18, the two top-most lines carry N_2 and O_2 gases which are later combined to form artificial pure air, i.e. without the interference of $CO_{2(g)}$, hydrocarbons, etc. The mass flow controllers on each line governs the gas flow rates and they are calibrated specifically for the type of gas that runs through them. The volumetric flow rate for $N_{2(g)}$ is set to be 0.750 SLM (standard liters per minute) while the volumetric flow rate for $O_{2(g)}$ is 0.250 SLM, thus the total air volume equals to 1.0 SLM. After mixing, this artificial air bubbles through a glass humidifyier bottle which is filled with deionized water, as shown in Figure 19.

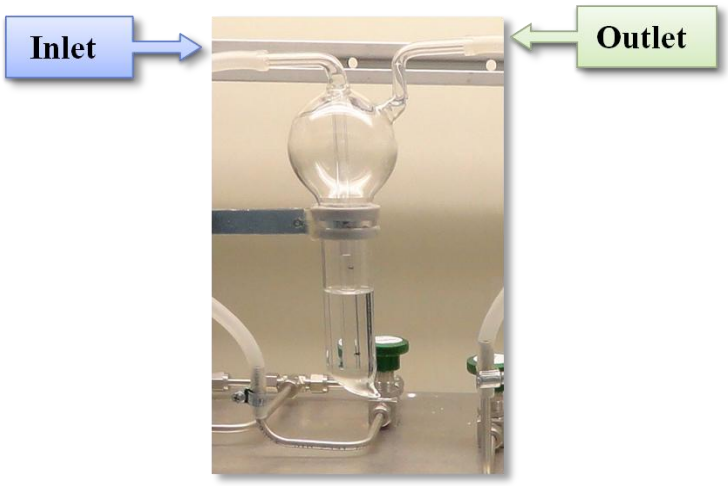

Figure 19. Gas humidifier bottle, filled with deionized water.

The third gas line (*NO line*) is used to carry the $NO_{(g)}$ into the gas mixture. As mentioned above, the gas tank connected to the *NO line* has 100 ppm $NO_{(g)}$ in $N_{2(g)}$, however the NO_x level at the reactor inlet is set to be 1 ppm NO in 1.0 L air. In other words, the concentration of NO in the gas tank is diluted in N_2+O_2 mixture by a hundred-fold to obtain 1 ppm NO in the reactor inlet. The required flow rate is calculated according to the following equation:

$$Ax+By+Cz = n\,(x+y+z)$$

where A, B and C represents the concentration of $NO_{(g)}$ in each pipe before mixing (A=0, B=0), x, y and z are the volumetric flow rates in each pipe before mixing and n=1ppm, the final concentration of $NO_{(g)}$ after mixing. The sum x+y+z represents the total gas flow rate in the pipeline (and therefore in the reactor) after mixing. Taking into account that C=100ppm ($NO_{(g)}$ concentration in the gas tank) and x+y = 1.0 L/min, one can calculate the flow rate, z, to give 1ppm gas concentration over the catalyst:

$$(0 \text{ x } 0.75 \text{ L/min}) + (0 \text{ x } 0.25 \text{ L/min}) + (100\text{ppm x } \mathbf{z}) = 1 \text{ ppm x } (1.0 \text{ L/min} + \mathbf{z})$$

$$100\,\mathbf{z} = 1.0 \text{ L/min} + \mathbf{z}$$

$$\mathbf{z} = 0.0101 \text{ L/min}$$

$$= 10{,}1 \text{ mL/min}$$

Therefore, approximately 10,1 mL/min (SCCM) $NO/N_{2(g)}$ is sent through the third gas line and it gets mixed with the humid air (N_2+O_2) that comes out of the humidifier bottle.

After mixing, the humid NO/ N_2+O_2 mixture flows into the reactor and over the catalyst and the pressure of the mixture is measured just before the reactor entrance by a CM (Capacitance Manometer, MKS Baratron). This gauge operates within 1.0 – 1000 Torr and provides reproducible pressure readings independent of the type of the gas(es) used.

The reacted gas comes out of the photoreactor and goes directly into the Chemiluminescence Ambient NO_x Analyzer (HORIBA), which monitors the concentrations of $NO_{(g)}$, $NO_{2(g)}$ and the total $NO_{x(g)}$ in the incoming gas stream.

2.2.1.2 Photocatalytic Flow Reactor

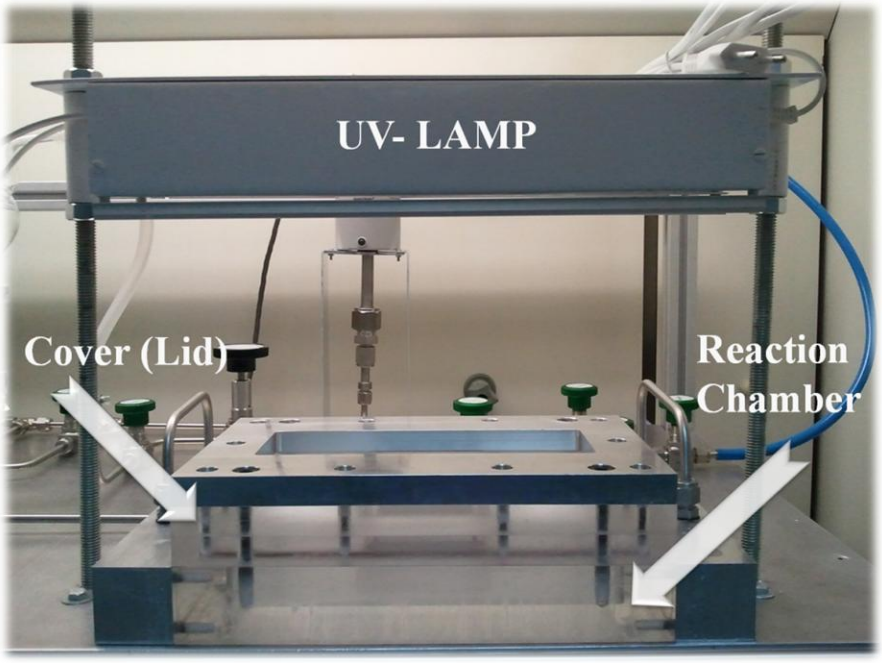

Figure 20. Photocatalytic flow reactor and the UV-lamp that irradiates the reaction chamber.

The photocatalytic flow reactor, shown above in Figure 20, is a custom designed reaction cell for photocatalytic NO oxidation and storage. Its main framework is made out of poly-methyl methacrylate (PMMA), a thermoplastic which is used as a transparent glass substitute and is also known as "*acrylic glass* or *plexy glass*". PMMA is a lightweight and strong material with an impact strength (~0.22 J/cm) higher than that of glass [91]. It is shatter-proof and easily shapeable for processing compared to glass. In addition, PMMA is also more resistant to environmental weathering compared to other plastics such as polystyrene (PS) or polyethylene (PE) [92]. Such properties of PMMA make it an excellent choice for usage under UV-light.

The main framework of the flow reactor is composed of two parts; **(a)** a reaction chamber where the photocatalyst is placed and **(b)** a cover that is tightly closed on top to make the reactor airproof. The passage of UV light, however, is allowed by a 3 mm thick quartz window placed inside the cover piece and when the reactor is closed, this quartz window sits right above the photocatalyst (Figure 21).

The cover itself is assembled by combining four separate pieces; two specially designed PMMA plates are utilized to sandwich the quartz window (via O-rings) and a screw-in aluminum pressure plate on top is used to compress and tighten all components into a single piece-reactor cover. Two types of screws are placed on the aluminum pressing plate; 10 x M5 screws (green circles in Figure 21) are used to hold together the cover and once they are fixed, they are not opened. On the other hand, 4 x M8 screws (violet circles in Figure 21) are inserted through the cover into the bottom half of the reactor and they are screwed in and out to close and open the reaction chamber before and after the photocatalytic performance experiments.

The connection of the stainless steel gas lines to the PMMA reaction chamber is managed via two aluminum connection blocks. The tubings are attached to these aluminum blocks with Swagelok straight fittings and the blocks themselves are screwed into the reaction chamber at both inlet and outlet ends. The gas stream comes through a 5 mm high conical slit inside the inlet aluminum block, then is delivered into the photoreactor where it passes through a 3 mm high slit over the catalyst and finally the flow comes out of the outlet aluminum block and goes directly to the NO_x Analyzer.

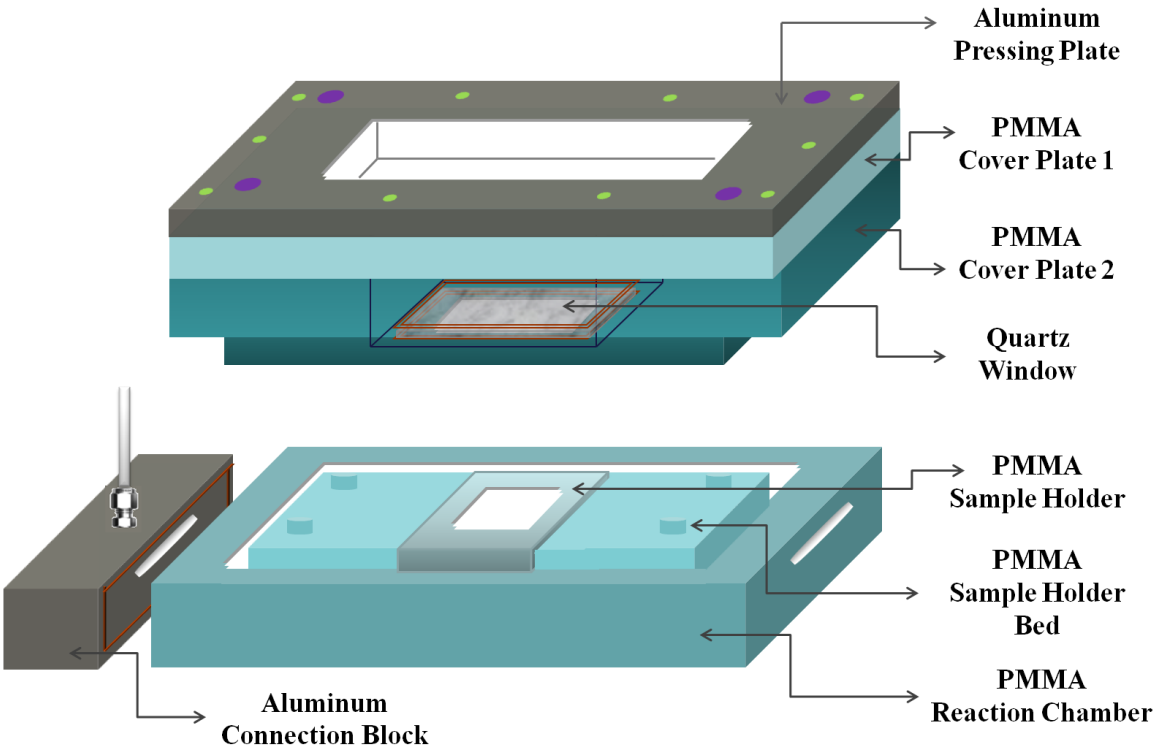

Figure 21. Custom designed photocatalytic flow reactor assembly.

The powder photocatalysts are pressed into a 2 x 40 x 40 mm sample holder (Figure 22), which is inserted into a sample holder bed and finally, this sample holder bed is placed into the reaction chamber.

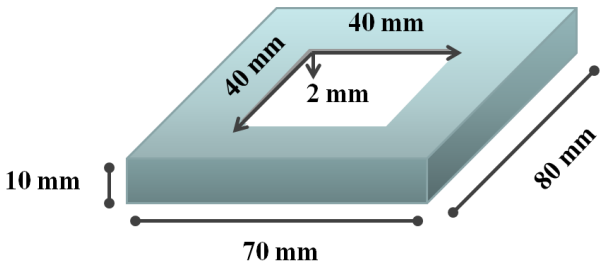

Figure 22. Dimensions of the sample holder for powder photocatalysts.

Top and lateral dimensions of the reactor can be seen in Figures 23- 24.

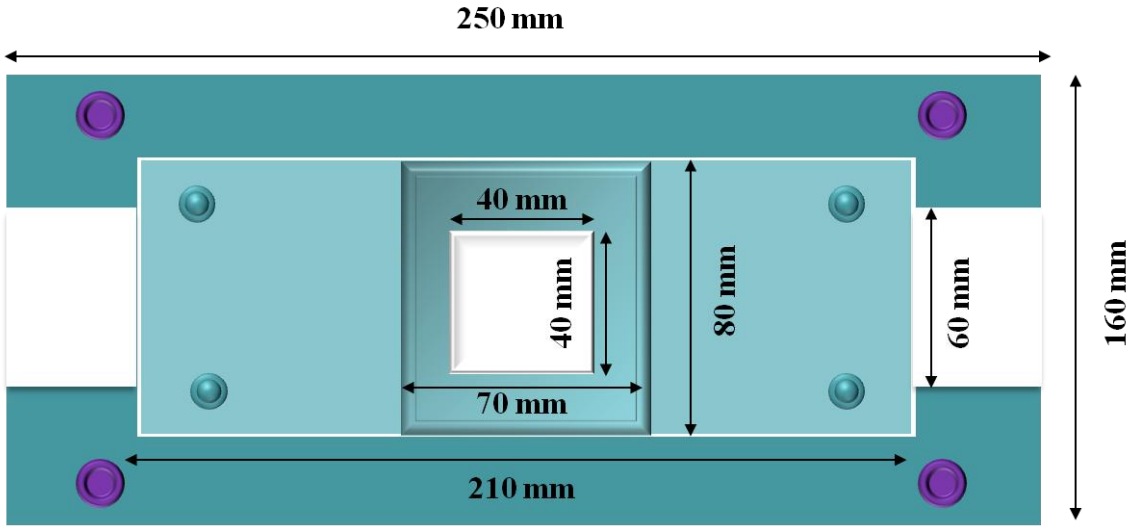

Figure 23. Topview dimensions of the reaction chamber.

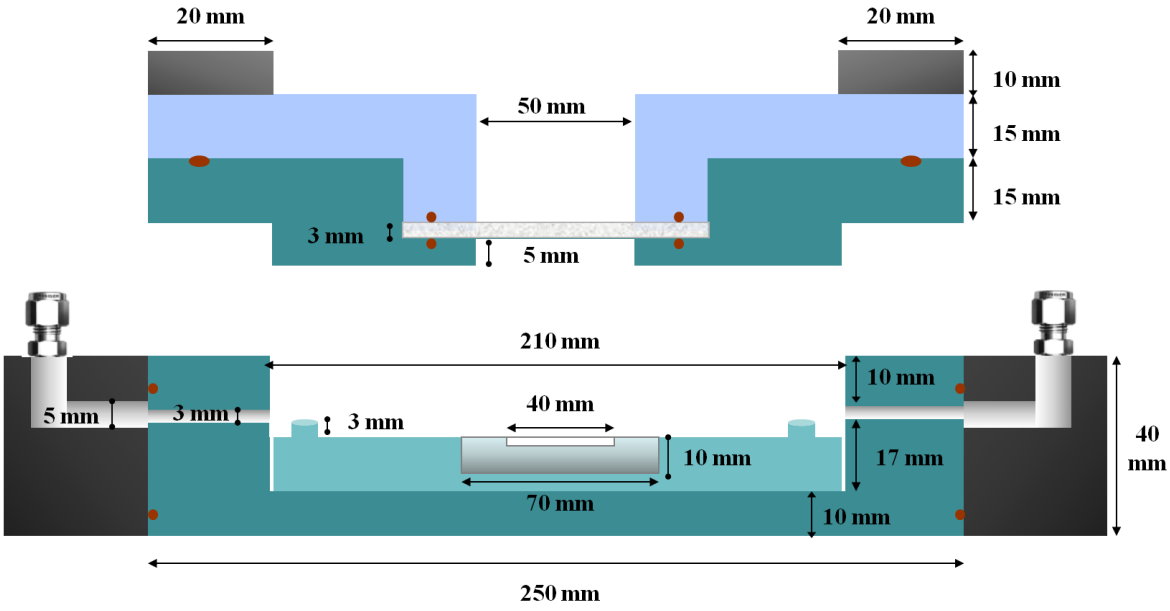

Figure 24. Lateral dimensions of the photocatalytic flow reactor. Brown circles show the positioning of viton O-rings.

In Figure 25, the pathway of the gas stream inside the closed reactor is visualized.

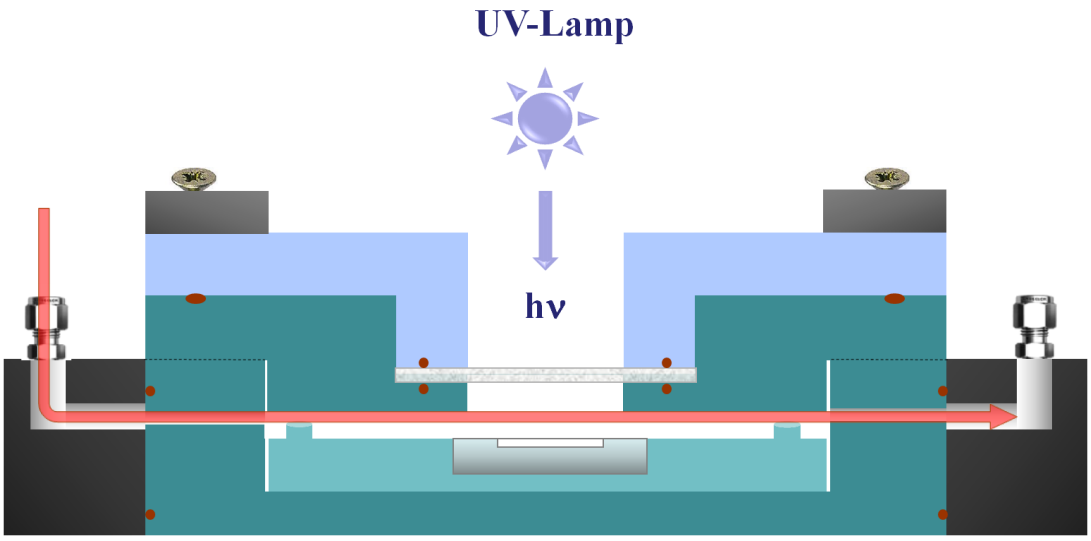

Figure 25. Closed view of the photocatalytic flow reactor and pathway of the flow inside the reactor.

2.1.1.3 UV-Lamp

The photoreactor is illuminated with a UV-lamp, constituted by two parallel connected 8 Watt UVA lamps (F8W/T5/BL350, Sylvania/Germany) whose emission wavelength is centered around 350 nm (Figure 26). These lamps are also known as black lights.

Figure 26. 8W UVA lamp (Sylvania).

The photon power density (Irradiance, W/m^2) of the UV-lamp is measured by a photo-radiometer (HD2302.0, DeltaOhm/Italy) with a UVA probe (LP471 UVA, DeltaOhm).

Figure 27. Photoradiometer for irradiance measurements and its UVA probe (DeltaOhm).

Typical response curve of the UVA probe is shown in Figure 28:

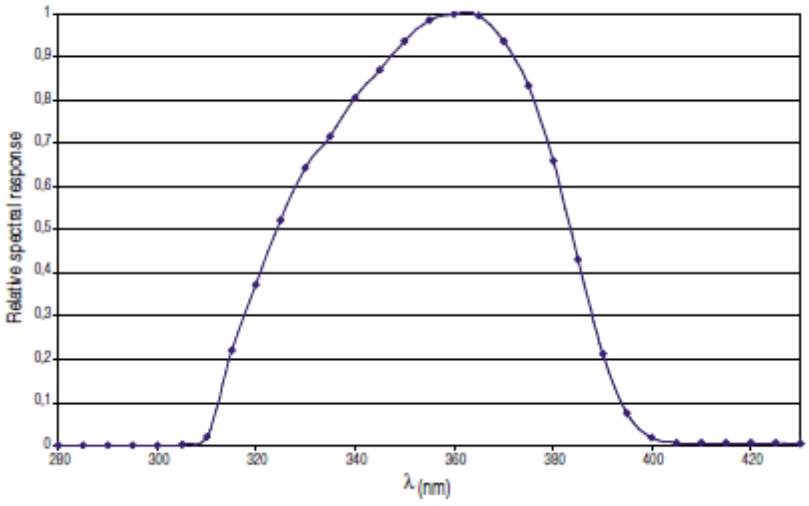

Figure 28. Response curve for LP471 UVA probe.

2.1.1.4 Chemiluminescent Ambient NO_x Analyzer

Figure 29. APNA 370 Chemiluminescent Ambient NO_x Analyzer (HORIBA)

Figure 29 gives the frontal view of APNA 370 Chemiluminescent Ambient NO_x Analyzer (HORIBA) which is used to measure the concentrations of $NO_{(g)}$, $NO_{2(g)}$ and the total $NO_{x(g)}$ in the gas stream coming from the outlet of the photoreactor.

The measurement principle of the instrument depends on the oxidation of the incoming NO into the excited state NO_2* with $O_{3(g)}$ and the device itself is capable of producing ozone inside its ozonizer unit. This unit pumps in atmospheric air through an air filter and oxidizes the $O_{2(g)}$ in the air into $O_{3(g)}$ using an incorporated UV-lamp. The generated ozone is introduced into a reaction chamber inside the instrument where it is used in oxidizing NO [93]. The instrument also has a *self-reproducing* type silica gel dryer unit to dry the air that is used in forming $O_{3(g)}$. The dryer unit has two drying cylinders. When one cylinder is in use, the other is being reactivated. During the reactivation, silica gel is heated at about 160^{o}C for 135 minutes to expel the moisture and then cooled for 45 minutes. The lines are used and reactivated interchangeably every 180 minutes so that continuous drying is achieved [93]. The schematic representation of the ozonizer unit is shown in Figure 30.

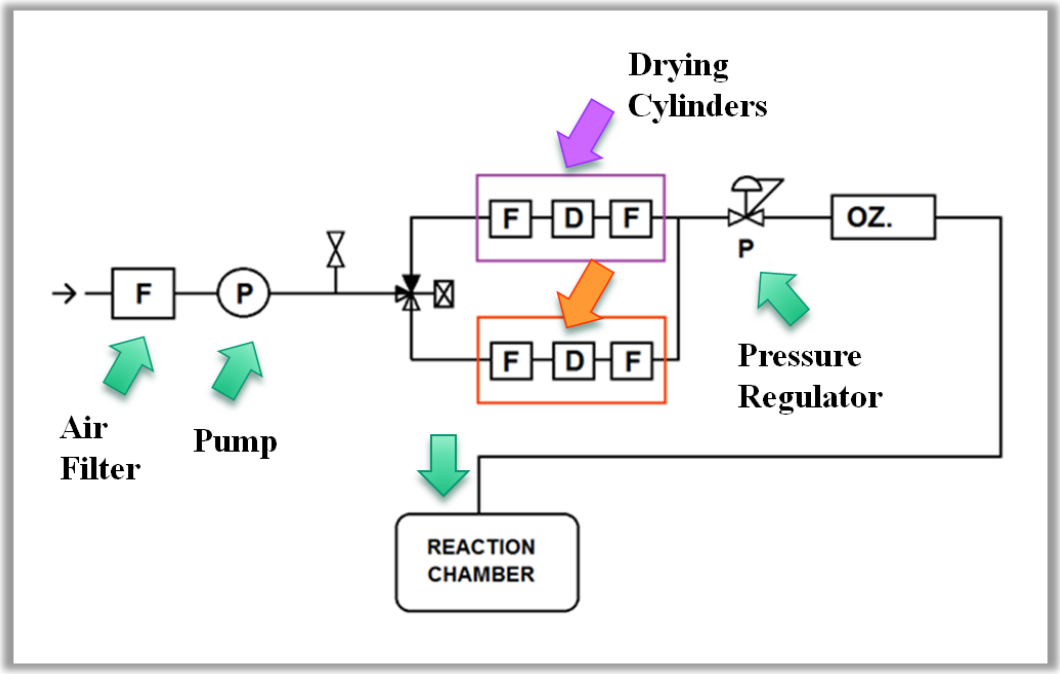

Figure 30. Schematic drawing of the *Ozonizer unit* inside the Chemiluminescent NO_x Analyzer [93].

Inside the reaction chamber of the NO_x analyzer, ozone is added to the sample gas containing NO_x species and a part of nitrogen monoxide (NO) in the sample gas is oxidized to nitrogen dioxide (NO_2). Some of the generated NO_2 is in the excited state (NO_2*) and these species luminesce broadband ***visible to infrared*** photons as they revert to a lower energy state. This phenomenon of light emission is known as chemiluminescence.

$$NO + O_3 \rightarrow NO_2^* + O_2 \quad (35)$$

$$NO_2^* \rightarrow NO_2 + h\nu \quad (36)$$

Reaction (35) is extermely fast, involves only NO and is affected little by other coexistent gases. When the NO concentration is low, the generated light intensity is proportional to the NO concentration. Measuring the concentration of NO by monitoring this reaction is known as the *chemiluminescence method* (CLD method).

In APNA 370, the samples gas is divided into two flow lines. One line measures the NO concentration directly with the descibed CLD method, while the other line is used for measuring the total NO_x ($NO+NO_2$) concentration. This measurement is achieved by first reducing NO_2 in the flow into NO with an incorporated *catalytic NO_x converter* and then determining the NO concentration which is equal to the starting NO_x concentration. These gas lines are switched every 0.5 s with solenoid valves and are introduced to the reaction chamber in turn [93].

The instrument calculates NO_x, NO_2 and NO concentrations from the outputs obtained by a photodiode, which are proportional to the NO_x and NO concentrations and monitors the results as continuous signals.

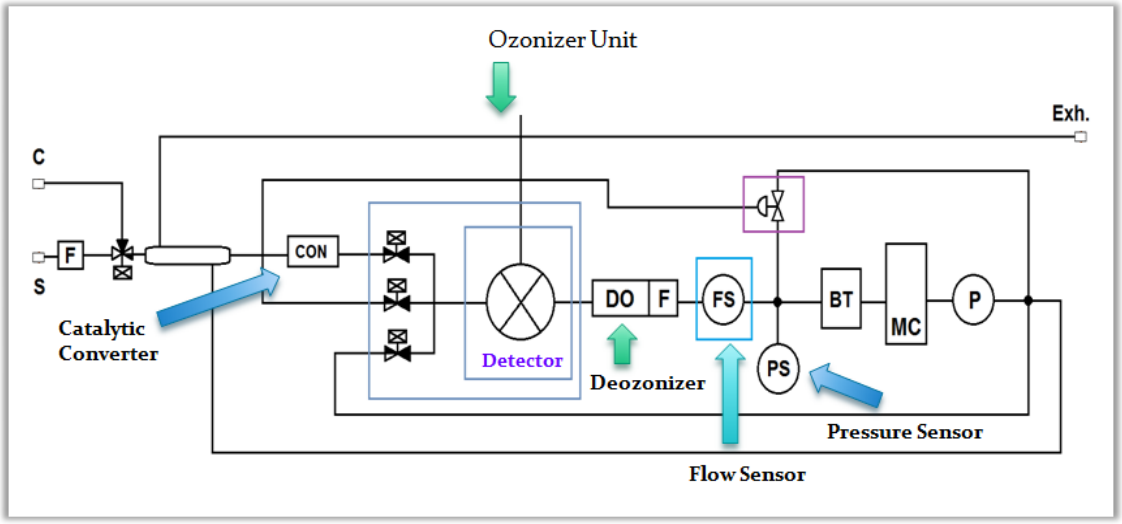

Figure 31. Schematic drawing of the *Reaction Chamber* inside the Chemiluminescent NO_x Analyzer [93].

The output range of APNA 370 can be adjusted to 1, 2, 5 or 10 ppm for NO, NO_2 and NO_x concentrations and the instrument has a minimum detection sensitivity of 0.5% of the selected full scale.

2.3 Experimental Protocols

2.3.1 Photocatalytic NOx Oxidation/Storage under UVA Exposure

The photocatalytic powder samples are pressed into the sample holders in equal amounts (950 mg for each photocatalyst) and these sample holders are placed inside a custom designed UVA cabinet before the photocatalytic performance tests. There, the samples are irradiated with an ultraviolet lamp (3x 8W Sylvania, with a photon power density of ~7.5 W/m^2) for 18 hours, and this pretreatment is required to decompose residual organic matter on the surface of the photocatalyst. This duration is defined as "*the activation period*" for the samples. In ISO22197-1 standard for photocatalytic NO_x oxidation, the pretreatment time is suggested to be at least 5 hours [88].

After the 18 hour activation period, the sample holder is taken out of the UVA cabinet and placed into the flow reactor where the photocatalytic performance experiment takes place. These experiments are completed in five consecutive stages: **(1)** Dark by-pass (*Start*) **(2)** Dark adsorption **(3)** UV-On period (Photocatalytically active period) **(4)** UV-Off period (Dark purge) **(5)** Dark by-pass (*End*).

The experiment starts off with a *Dark by-pass* period and during this time, first the N_2 and O_2 valves are opened, the gases begin to flow and mix, the tubings are flushed, the air bypasses the reactor through the by-pass line and goes directly to the chemiluminescent NO_x analyzer (Figure 32). At this stage, the analyzer gives ~0.001 ppm readings for all three channels (NO, NO_2 and total NO_x). Typical overall duration of the initial *Dark by-pass* period is 15 min.

Next, the NO/N_2 valve is opened and $NO_{(g)}$ starts to mix with N_2 + O_2 and then the NO + N_2 + O_2 mixture bypasses the reactor through the by-pass line and flows to the chemiluminescent NO_x analyzer (Figure 33). At this point, both NO and NO_x concentrations read by the analyzer is stabilized at 1 ppm while the experimentally measured NO_2 concentration is around 0.01 ppm. Typical overall duration of this period is 1 hour.

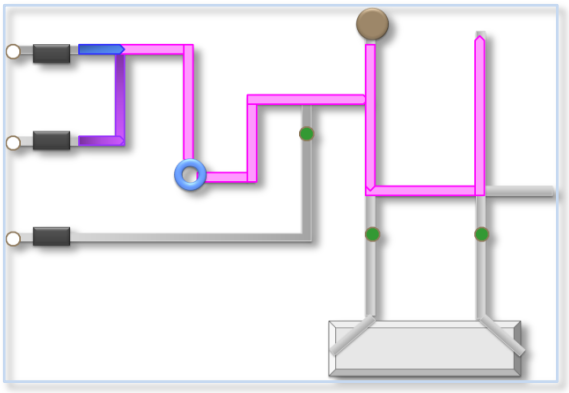

Figure 32. Gas flow at the beginning of the initial **Dark by-pass** period. The blue line represents $N_2(g)$, purple line represents $O_2(g)$ and pink line is their mixture.

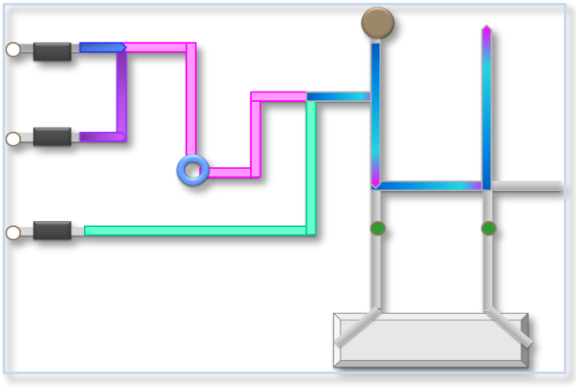

Figure 33. Gas flow after the opening of NO/N_2 valve during the initial **Dark by-pass** period. The pink line represents N_2+O_2, green line represents $NO(g)$ and multicolored line is the N_2+O_2+NO mixture.

Next stage is the *Dark adsorption* and this period starts when the by-pass valve is closed and at the same time the inlet and outlet valves of the flow reactor are opened. During this time the UV-lamp is still off and thus the $NO + N_2 + O_2$ mixture starts to run through the reactor and over the catalyst in dark (Figure 34). When the reactor valves are opened, the concentration of $NO_{(g)}$ (thus, the $NO_{x(g)}$) decreases to a certain level but after a short while their concentrations return almost back to the 1 ppm level and is stabilized at this value. This drop is observed as a result of $NO_{(g)}$ adsorption occuring on the surface of the catalyst and on the walls of the reactor. When the sample surface gets saturated, $NO_{(g)}$ starts flowing over the catalyst without getting captured on its surface and $NO_{(g)}$ level read by the NO_x analyzer is

stabilized back at ~1 ppm. The time required for the stabilization of $NO_{(g)}$ concentration varies between 5-20 minutes depending on the physisorption-capacity of the sample. The dark purge is continued for 10 more minutes after the stabilization of the $NO_{(g)}$ level at ~1 ppm.

The third and the most important stage of the experiment is the *UV-On* period and the photocatalytic oxidation and storage reactions take place during this time. In this period, the UV-light (with a photon power density of ~ 5 W/m^2) is turned on and as a result, $NO_{(g)}$ is oxidized to $NO_{2(g)}$. The lamp is kept on for about 60 minutes.

The fourth stage is the *UV-Off* (or dark purging) period. As the name implies, after completion of the 60-minute *UV-On* period, the UV-light is turned off. $NO_{(g)}$ oxidation stops immediately and after a few minutes, the concentrations of $NO_{(g)}$ and $NO_{x(g)}$ reaches back to c.a. 1 ppm, while the $NO_{2(g)}$ level drops down to virtually zero. Typical overall duration of this period is 10 min.

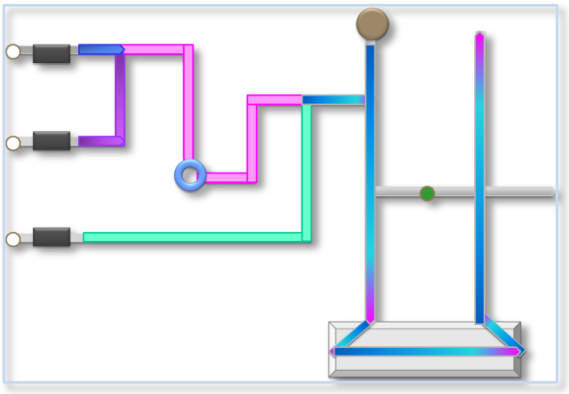

Figure 34. Gas flow during the dark adsorption, *UV-On* (Photocatalytically active period) and UV-Off (Dark purging) periods. The pink line represents N_2 + O_2 mixture, the green line represents *NO* and the multicolored line is the *NO* + N_2 + O_2 mixture.

Finally, the experiment is completed when the inlet and outlet valves of the flow reactor is closed and the by-pass line is re-opened. The *NO* + N_2 + O_2 mixture starts to go directly to the the chemiluminescent NO_x analyzer, same as the *Dark by-pass* period at beginning of the experiment. At this point, the reactor cover can be opened and the photocatalyst can be replaced with a new catalyst in order to start a new experiment.

The continuous readings of the NO_x Analyzer are recorded in performance analysis plots. X-axis of the graph gives the time in minutes and Y- axis of the graph shows the concentrations of the gases (NO, NO_2 and total NO_x) in ppm. In these plots, the blue line is the NO_x concentration, the black line is the NO concentration and the red line is the NO_2 concentration.

When the by-pass line is re-opened at the end of the experiment, the photocatalytic analysis curve is complete and ready to be examined (Figure 35).

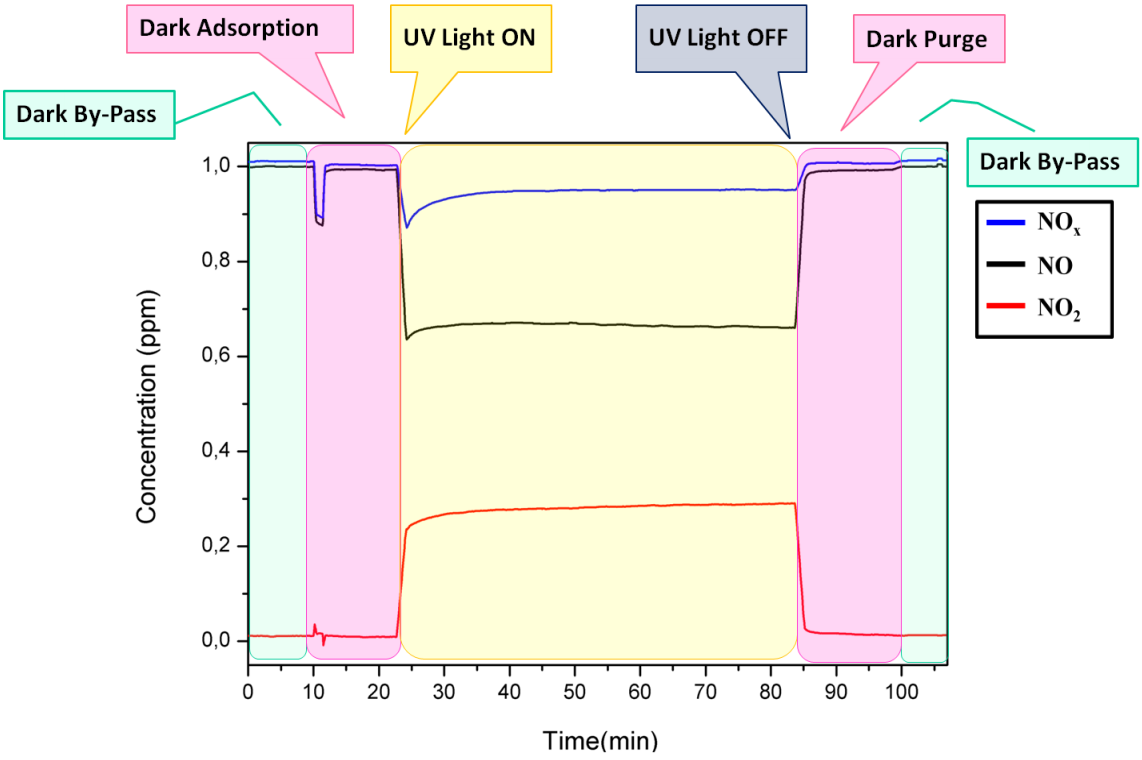

Figure 35. Complete photocatalytic analysis curve at the end of the experiment.

The evaluation of the performance analysis plot is achieved in three steps; in the first step, the integrated areas over the NO_x line (blue area in Figure 36), over the NO line (blue+black areas in Figure 36) and under NO_2 line (red area in Figure 36) are determined for the first 60 minutes of UV-irradiation. These areas represent the decrease in the total $NO_{x(g)}$ and NO(g) as well as the increase in the $NO_{2(g)}$ (in ppm) for the first hour of the photocatalytic reaction. Next, these ppm values are converted into moles, showing the change in the amount of each species.

Finally, using the calculated mole values, the photonic efficiency, ζ%, of the photocatalytic NO_x oxidation and storage catalyst is determined for the total NO_x abatement (absorption/storage) and NO_2 production (release). In an efficient PhoNOS catalyst, the photonic efficiency for the total NO_x abatement should be very high while the efficiency for NO_2(g) release should be as low as possible, since the main function of these materials is not just to oxidize NO, but also to prevent the release of gaseous oxidation product, NO_2 back into the atmosphere .

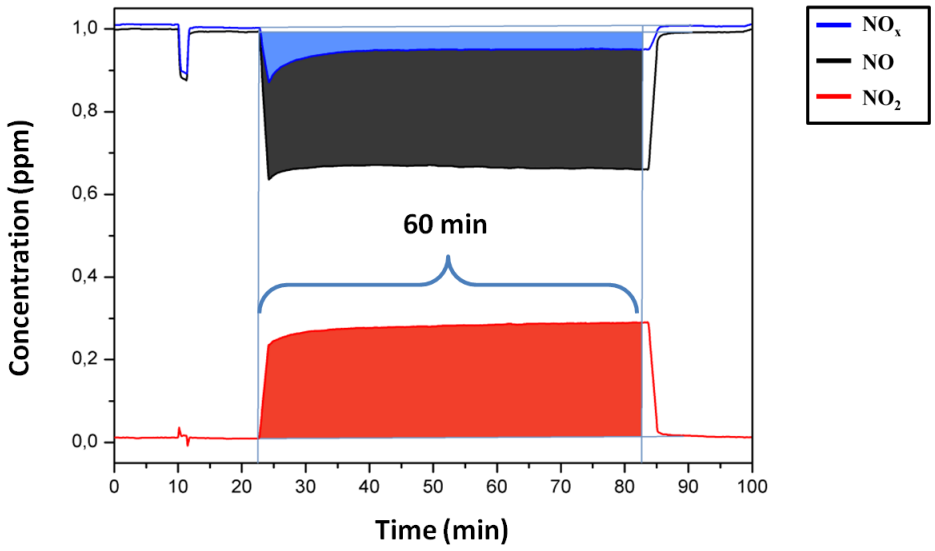

Figure 36. Schematic depiction the integrated areas for the total NO_x (blue area) and NO (blue+black areas) abatement and NO_2 (red area) production.

Since the number of moles of the stored NO_x or produced $NO_{2(g)}$ are known, the photonic efficiency (ζ%) can be calculated with the following equation [94]:

$$\zeta\% = \frac{n\,(\text{stored } NO_x \text{ or produced } NO_2)}{n\,(\text{available photons})} \times 100$$

In order to determine the number of moles of incident photons on the catalyst surface during 60 min, the photon flux of the lamp (ϕ, mol of photons/h) should be known. Note that all of the photons sent to the photocatalyst in that time are assumed to be absorbed by the catalyst surface, although practically this is not the case (due to various complex photon scattering phenomena).

The photon flux (ϕ) can be calculated using the following simple relationship [94]:

$$\phi = \frac{I'' \lambda S}{N h c}$$

Here, *I''* represents the photon power density for the UV lamp experimentally measured at the top surface of the quartz cover of the photoreactor (typically, 5 Watts/m^2), λ is the representative emission wavelength of the UV lamp (i.e. 350 nm), S is the surface area of the photocatalyst that is exposed to the UV irradiation (i.e. 16 cm^2); N is Avagadro's number, h is Planck's constant and c is the speed of light. With this formula, the typical photon flux corresponding to the current set of experiments was calculated to be 8.4×10^{-5} einstein/h (= 0.23×10^{-5} einstein/s) and using this value, one can calculate the photonic efficiency of the aforementioned reactions. Typical photonic efficiency values obtained in the current work was in the range of 0.005%- 1.2%.

2.3.2 XRD & BET

The powder XRD patterns were recorded using a Rigaku diffractometer, equipped with a Miniflex goniometer and an X-ray source with Cu$K\alpha$ radiation, at λ = 1.54 Å, 30 kV and 15 mA. The powder samples were pressed and affixed to standard-sized glass slides and scanned in the 10–80° 2θ range with a scan rate of 0.05° s^{-1}. Diffraction patterns were assigned using Joint Committee on Powder Diffraction Standards (JCPDS) cards supplied by the International Centre for Diffraction Database (ICDD).

Surface area measurements of the samples (which were initially dehydrated at 623 K for 4 hr in vacuum) were determined by N_2 adsorption at 77 K via conventional BET (Brunauer, Emmett, and Teller) method by using a BET surface area analyzer (Micromeritics TriStar Surface Area and Porosity Analyzer).

2.3.3 Raman Spectroscopy

Raman spectra were recorded on a HORIBA Jobin Yvon LabRam HR 800 instrument, equipped with a confocal Raman BX41 microscope, spectrograph with an 800 mm focal length and a nitrogen cooled CCD detector. The Raman spectrometer was equipped with a Nd:YAG laser (λ = 532.1 nm). During the Raman experiments, the laser power was tuned to 20 mW, measured at the sample position, in order to minimize the sample heating effects. The incident light source was dispersed by holographic grating with a 600 grooves/mm and focused onto the sample by using a 50X objective. The confocal hole and the slit entrance were set at 1100 μm and 200 μm, respectively. The spectrometer was regularly calibrated by adjusting the zero-order position of the grating and comparing the measured Si Raman band frequency with the typical reference value of 520.7 cm^{-1}. The powder samples were mechanically dispersed onto a single-crystal Si holder for the Raman measurements and all Raman spectra were acquired within 100-4000 cm^{-1} with an acquisition time of 213 s and a spectral resolution of 4 cm^{-1}.

Pure TiO_2 (Anatase - Nano powder, 99.9%, 40nm, Inframat Advanced Materials), rutile (obtained after calcination of the anatase nanopowder at 1000^oC for 2 h), $NaNO_3$ (ACS Reagent, Sigma Aldrich), $LiNO_3$ (ReagentPlus®, Sigma Aldrich), KNO_3 (ACS Reagent, Fluka), $CsNO_3$ (ACS Reagent, Sigma Aldrich), $Ca(NO_3)_2$ (Fluka, Sigma Aldrich), $Sr(NO_3)_2$ (ACS Reagent, Sigma Aldrich) and $Ba(NO_3)_2$ (ACS Reagent, Sigma Aldrich) samples were used for the reference Raman spectra.

3. RESULTS AND DISCUSSION

3.1 Pure TiO_2 and TiO_2/Al_2O_3 Binary oxides

3.1.1 Structural Characterization of the Thermally Treated Pure TiO_2 and TiO_2/Al_2O_3 Binary oxides

The crytalline structures of the pure TiO_2 and TiO_2/Al_2O_3 (Ti/Al) binary oxides have been examined with XRD and Raman spectroscopy techniques while their specific surface areas have been determined with BET method. The anatase to rutile transition characteristics of Ti/Al samples have been compared with that of pure TiO_2.

3.1.1.1 XRD Experiments

In all of the photocatalytic performance tests, commercially available Degussa P25 mixed phase titania was utilized as the benchmark (gold standard) sample. Figure 37 represents the reference XRD data for Degussa P25 titania, in comparison with pure anatase and pure rutile TiO_2 phases. Degussa P25, consisting of a mixture of approximately 85% anatase and 15% rutile, shows both anatase (JCPDS 21-1272) and rutile (JCPDS 04-0551) diffraction lines in its XRD pattern.

In 1957, *Spurr and Myers* have developed a method tocalculate the mass fraction of rutile and anatase phases in a crystalline TiO_2 sample [95], which utilizes the intensity of the anatase (101) diffraction line at 25.18^o 2θ (I_A) and the intensity of the rutile (110) diffraction line at 27.35^o 2θ (I_R) :

$$\text{Anatase (\%)} = [I_A / (I_A + 1.26\ I_R)] \times 100$$

$$\text{Rutile (\%)} = [1.26\ I_R / (I_A + 1.26\ I_R)] \times 100$$

In Figure 37 the intensities of the anatase (101) line and the rutile (110) line are observed to be I_A =3454 and I_R =620. By substituting these values to the above formula, the mass fractions of anatase and rutile in P25 were calculated to be 85% and 15% respectively, same as the literature values [96-100].

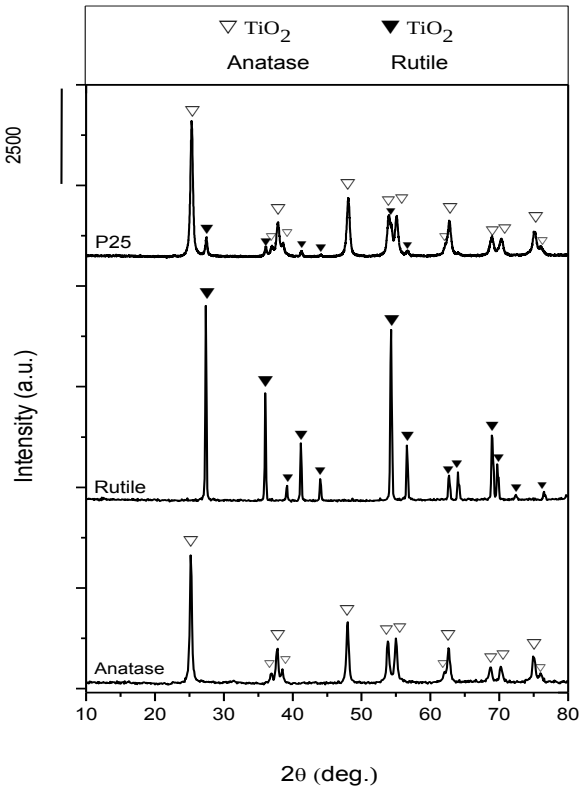

Figure 37. XRD patterns of Degussa P25, pure *anatase* and pure *rutile*.

Figure 38a and 38b illustrate the thermal behavior of pure TiO_2 prepared in our lab and calcined in air between 150-1000^oC for 2 h. Panel (a) shows that crystalline titania is not discernible in XRD until 350^oC after which the anatase diffraction pattern (JCPDS 21-1272) starts to be visible. It is also observed that TiO_2 becomes fully crystallized in anatase phase (with no sign of rutile) when heated up to 500^oC. However, when the sample is calcined at 600^oC, minor diffraction lines coming from the (110) and (101) planes of the rutile phase (JCPDS 04-0551) can be seen at 27,35^o and 36^o *2θ* respectively (Figure 38-b). Using the *Spurr and Myers* method, the phase distribution of TiO_2 at 600^oC is calculated to be 92% anatase and 8% rutile.

At 700°C, the rutile lines in the XRD pattern become much more apparent and the calculated mass fraction for TiO_2 changes to 62% anatase and 38% rutile. Finally, when the TiO_2 is heated up to 800°C, the crystal structure becomes fully rutile (with no sign of anatase diffraction) and at 1000°C, rutile diffraction lines become slightly more intense.

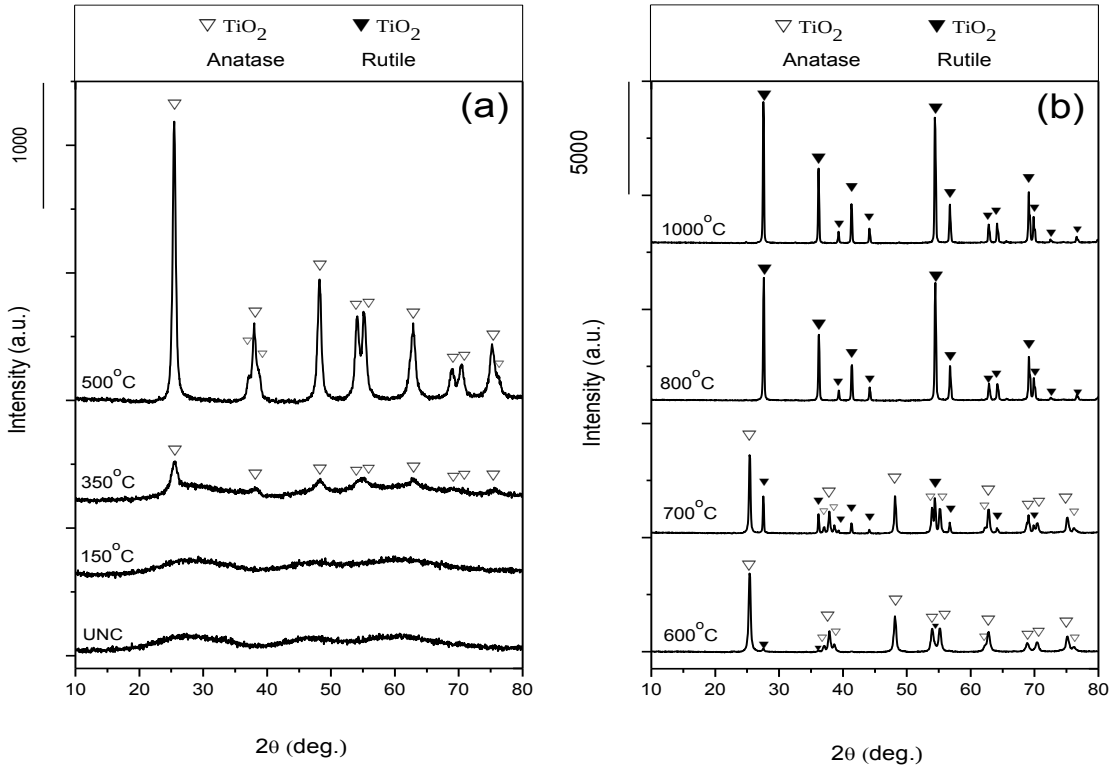

Figure 38. XRD patterns of pure TiO_2 before and after calcination in air between (a)150 to 500°C and (b) 600 to 1000°C.

In Figure 39, XRD patterns of the thermally treated TiO_2/Al_2O_3 (Ti/Al) binary oxides are given for three different Ti:Al mole ratios. Figure 39a indicates that in the presence of excess alumina in the mixture (i.e. Ti:Al mole ratio=0.25), the crystallization of titania is hindered to the extend that no TiO_2 crystalline phase is visible in XRD until the sample is heated up to 1000°C. However, an increase in the crystallinity of alumina is observed between room temperature and 950 °C and the intensity of γ-Al_2O_3 lines increase steadily. At 1000°C, titania crystallizes suddenly, followed by a transition of the alumina crystalline phase from γ-Al_2O_3 to α-Al_2O_3.

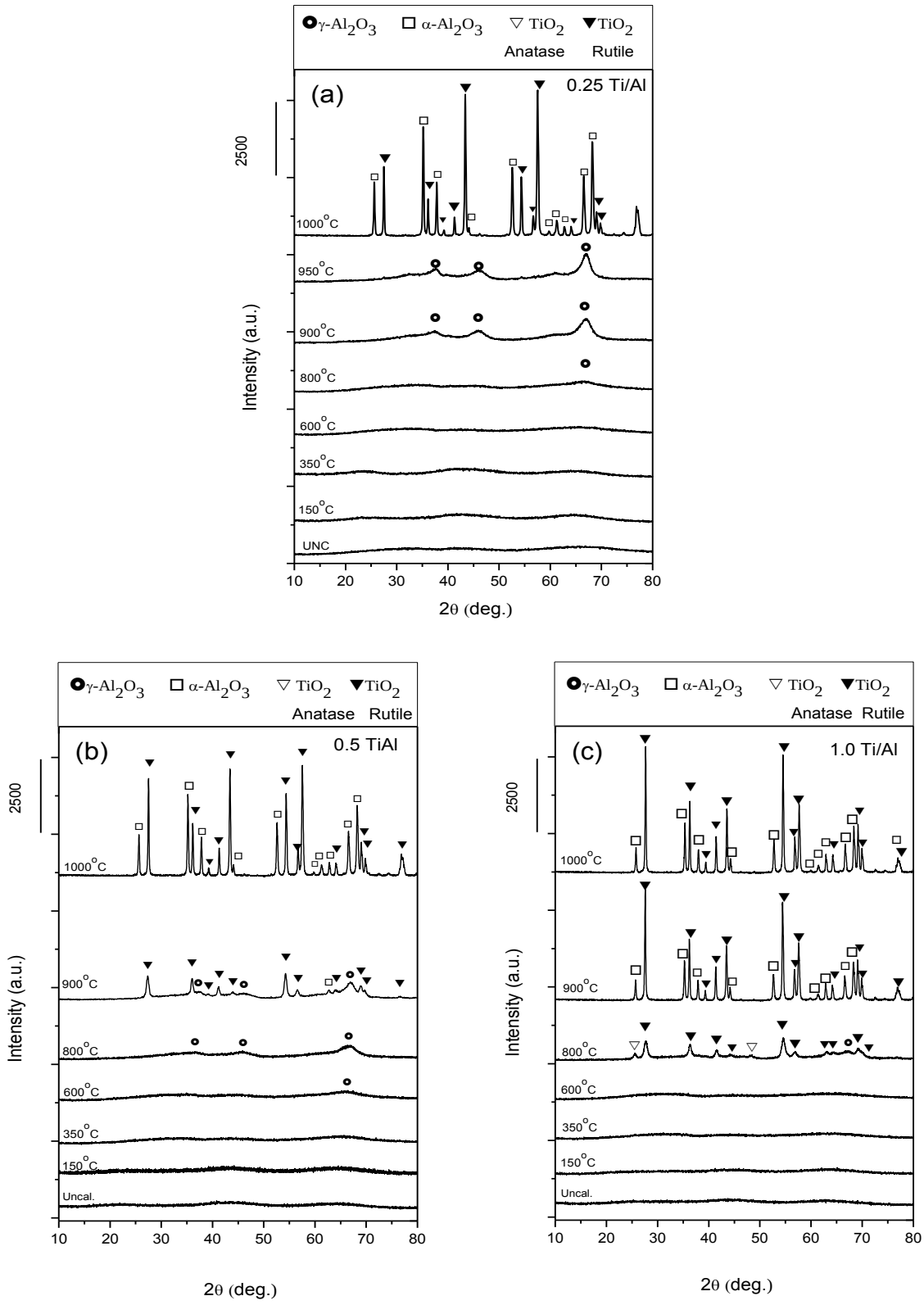

Figure 39. XRD patterns of the Ti/Al samples before and after calcination in the temperature range of 150-1000°C. (a) Ti:Al mol ratio = 0.25, (b) Ti:Al mol ratio = 0.50 and (c) Ti:Al mol ratio = 1.0.

It is known that the Al_2O_3 in this Ti/Al binary oxide system can incorporate into the anatase lattice and the two components end up forming a solid solution [101]. In such a solid solution, the anatase to rutile transition of titania is accompanied by a concurrent phase transition in alumina where γ-Al_2O_3 is transformed into α-Al_2O_3 (corundum). Depending on the TiO_2 content, γ-Al_2O_3 to corundum transition may occur at an earlier temperature than observed in pure alumina. This simultaneous phase transition is seen for 0.25 Ti/Al sample, although the rutile forms directly from an amorphous phase rather than through the usual anatase route.

In Figure 39b, the thermal evolution of 0.5 Ti/Al is given, which shows an amorphous structure for TiO_2 until 900^{o}C where it starts crystallizing directly as rutile. Note that the crystallization temperature of TiO_2 in 0.5 Ti/Al is lower than that of 0.25 Ti/Al. On the other hand, alumina in 0.5 Ti/Al becomes gradually more crystalline with thermal treatment and the intensity of γ-Al_2O_3 lines increase until 900^{o}C. At 1000^{o}C, TiO_2 reaches almost a fully crystalline state (as rutile) and the transition from γ-Al_2O_3 to α-Al_2O_3 is observed, similar to what is seen in the case of 0.25 Ti/Al. Figure 39c shows the thermal transformation for 1.0 Ti/Al sample. Here the crystallization of titania is observable in XRD around 800^{o}C where a mixture of both anatase and rutile crystalline phases forms. The composition of the mixture is calculated to be approximately ~27% anatase and ~73% rutile. When the sample is heated to 900^{o}C, anatase is almost completely transformed into rutile and concurrently the transition of γ-Al_2O_3 to corundum (α-Al_2O_3) is completed. At 1000^{o}C, only an increase in the intensities of rutile and α-Al_2O_3 lines is observed.

By comparing the characteristics of all three Ti/Al binary oxides and of pure titania, it can be suggested that as the amount of alumina in the mixture increases, nucleation of TiO_2 crystals is hindered and titania crystallization starts at a higher temperature. As a result, the temperature where XRD can detect crystalline phases increases (350 ^{o}C in pure titania compared to 800 ^{o}C for 1.0 Ti/Al, 900 ^{o}C for 0.50 Ti/Al and 1000^{o}C for 0.25 Ti/Al). Along these lines, it can also be argued that the addition of alumina inhibits the formation of anatase by increasing the nucleation temperature to a point at which rutile forms naturally. This argument has been discussed in a former study [102], where Wang et al. reported that in Ti/Al

composites, the amorphous TiO_6 octahedra and the AlO_6 octahedra interact strongly on the surface and form Ti-O-Al bonds. Phase transformation beginning from the surface of the structure is impeded by this bonding effect which restricts the self-structure and mode adjustment of TiO_6 octahedra and retards the phase transformation from an amorphous titania phase to anatase.

3.1.1.2 Raman Analysis

Raman spectroscopy measurements of the thermally treated pure titania and Ti/Al binary oxide samples were also performed in order to have a better understanding of their structural properties. Raman spectra for pure anatase, pure rutile and Degussa P25 TiO_2 are used as references. These results are given in Figure 40.

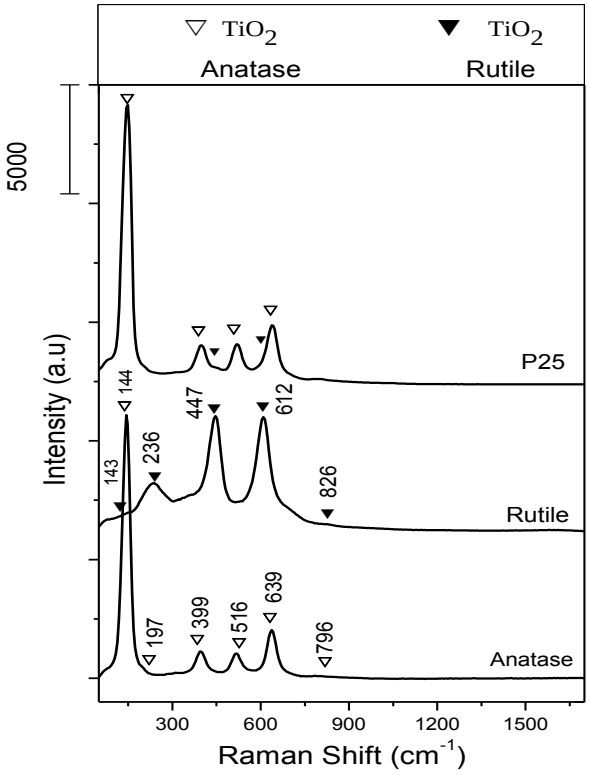

Figure 40. Raman spectra of Degussa P25, pure *anatase* and pure *rutile*.

The reference Raman spectrum of anatase phase shows six Raman peaks ($1A_{1g}$, $2B_{1g}$, and $3E_g$) at 144 (E_g), 197 (E_g), 399 (B_{1g}), 516 (A_{1g} + B_{1g}), 639 (E_g) and

796 cm^{-1} (E_g) [103]. On the other hand, the rutile phase can be characterized by a Raman spectrum with four Raman active modes ($A_{1g} + B_{1g} + B_{2g} + E_g$) at 143 ($B_{1g}$), 447 ($E_g$), 612 ($A_{1g}$), 826 cm^{-1} (B_{2g}) and also a two-phonon scattering band at 236 cm^{-1} [104]. Being a composite mixture of these two phases, the Raman spectrum of Degussa P25 displays both anatase and rutile bands, but the major contribution comes from the anatase phase.

Figure 41 represents the Raman data for the thermally treated pure TiO_2 and the Ti/Al binary oxides in three different Ti:Al mole ratios. In Figure 41a, The evolution of TiO_2 crystalline phases in pure titania can be observed upon calcination between 150-1000^oC for 2h. Here, the Raman spectra are in accordance with the XRD data, showing fully crystalline anatase signals even at 500^oC. At 600^oC, the only observable phase is still the anatase in the Raman spectrum although the XRD data showed weak diffraction lines for the rutile phase at that temperature. Around 700^oC, rutile formation is clearly observed with the Raman signals at 447 and 612 cm^{-1} and after 800^oC, the crystalline phase becomes totally rutile.

In panels (b), (c) and (d) of Figure 41, the thermal transformation of TiO_2/Al_2O_3 binary oxides with 0.25, 0.50 and 1.0 Ti:Al mole ratios are illustrated. As can be seen in panel (b), 0.25 Ti/Al sample do not show any crystalline phases until heated up to 900^oC where broad Raman signals that can be attributed to a poorly crystallized rutile phase is observed. At 950^oC, these signals become slightly more discernable but at 1000^oC, all four raman active modes (at 143, 447, 612, 826 cm^{-1}) and the two-phonon scattering band (236 cm^{-1}) of the rutile phase is apparent. This observation supports the XRD data where the bulk rutile signals could only be detected at 1000^oC. In the 0.50 Ti/Al case (Figure 41-c), when the sample is calcined at 800^oC, broad Raman features become visible around 236 and 447 cm^{-1}, which possibly belong to the rutile crystals and a poor signal around 144 cm^{-1}, which can be attributed to a minute amount of anatase phase in the mixture. Calcination for 2 h at 900^oC sharpens the rutile signals at 236, 447, 612 and 826 cm^{-1} and the major band of anatase at 144 cm^{-1} is still visible, though very weakly. Finally at 1000^oC, full transformation to rutile is observed. These findings justify the XRD data where 0.5 Ti/Al is crystalline after 900^oC and is completely rutile at 1000^oC.

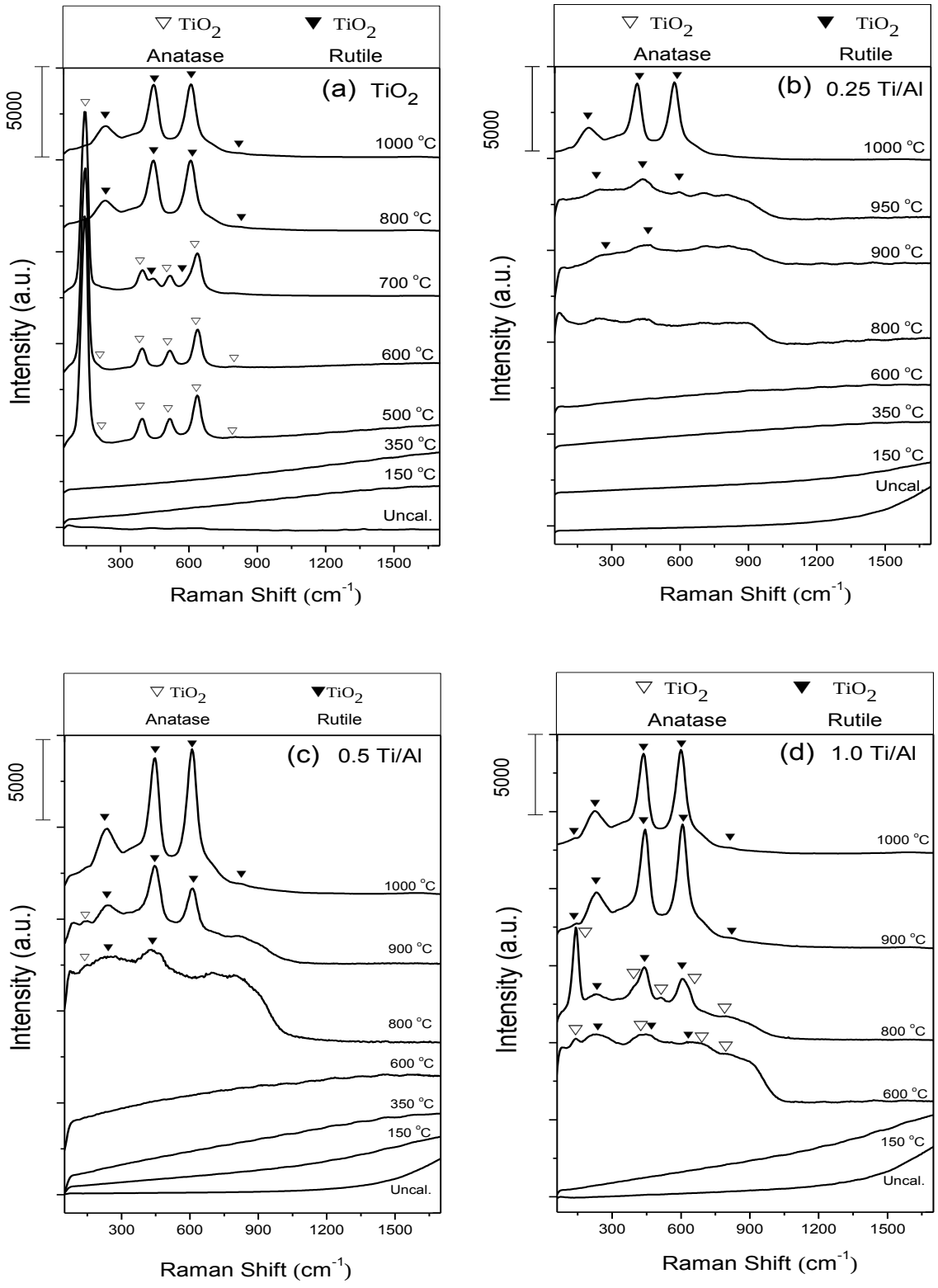

Figure 41. Raman spectra of pure TiO_2 and the Ti/Al samples before and after calcination in the temperature range of 150-1000^{o}C. (a) Pure TiO_2 (b) Ti:Al mol ratio is 0.25, (c) Ti:Al mol ratio is 0.50 (d) Ti:Al mol ratio is 1.0.

For 1.0 Ti/Al, even the 600^{o}C sample shows visible anatase and rutile bands at 144, 399, 516, 639, 796 cm^{-1} and at 236, 447, 612 cm^{-1}, respectively. When calcined at 800^{o}C, the signals for both phases become more intense, but at 900^{o}C, all bands belonging to the anatase phase diminish while the rutile signals become completely dominant.

In general, current Raman spectra of the Ti/Al binary oxides are consistent with the XRD data. However, the Raman measurements are more sensitive in monitoring the surface crystallization which starts almost a hundred degrees below compared to the transition temperatures obtained with XRD. For instance, in 0.50 Ti/Al, the Raman spectrum shows that at 800^{o}C the sample have a poorly crystalline rutile phase, while the XRD pattern of the sample does not display any crystallinity in titania until 900^{o}C.

3.1.1.3 BET Analysis

BET surface areas of the thermally treated pure titania and Ti/Al binary oxides were analyzed and the results are given in Table 13. Appearently, the titania-alumina composites have higher specific surface areas compared to pure titania, and based on the data presented, it can be suggested that adding alumina helps dispersing the titania considerably. Secondly, with increasing calcination temperatures, the S_{BET} values decrease monotonically, showing that the samples are strongly affected by the thermal treatment and cannot retain their porous structures at high temperatures. The reduction of the surface areas can be explained as a result of sintering and/or phase transformations. Pure titania loses its amorphous structure and starts displaying anatase diffraction lines in XRD at around 350^{o}C, whereas the Ti/Al samples stay amorphous at that temperature, and as a result, S_{BET} of TiO_2 is almost half of those of Ti/Al binary oxides at 350^{o}C. However at around 1000^{o}C, all samples have crystalline titania in rutile phase, and except for the 0.25 Ti/Al sample whose crystalline structure is composed mostly of corundum (α-Al_2O_3), all surface areas become nearly the same after calcination at 1000^{o}C.

Table 13. BET Specific surface areas (in m^2/g) of the samples calcined within 150-1000°C.

Sample T/ °C	**0.25 Ti/Al** [a]	**0.50 Ti/Al** [a]	**1.0 Ti/Al** [a]	**TiO_2** [a]
350	487.1	424	469.7	219.8
600	285.1	393	389.8	-
800	256.1	131	85.6	-
900	-	63.4	24.7	-
1000	16.8	9	8.8	8.9

[a] *Samples were calcined in air at the given temperatures for 2 hr.*

The specific surface area of Degussa P25 at room temperature is defined to be around 55 m^2/g in the literature [105].

3.1.2 Photocatalytic Performance Experiments

Photocatalytic performance results of the thermally treated Ti/Al binary oxides (0.25 Ti/Al, 0.5 Ti/Al and 1.0 Ti/Al) for NO oxidation and storage were evaluated against pure γ-Al_2O_3, pure γ-Al_2O_3 physically mixed with 10% (w/w) BaO and most importantly against Degussa P25 TiO_2. The interpretation of the relative photocatalytic performances were made by comparing the photonic efficiency of the samples towards total NO_x abatement and towards $NO_{2(g)}$ production.

Figure 42 shows the performance plots and photonic efficiencies of pure γ-Al_2O_3 and pure γ-Al_2O_3 +10% (w/w) BaO mixture. It is observed that neither alumina nor alumina+BaO mixture have the capability to oxidize NO or store NO_x directly from the gas phase in the presence of UVA irradiation.

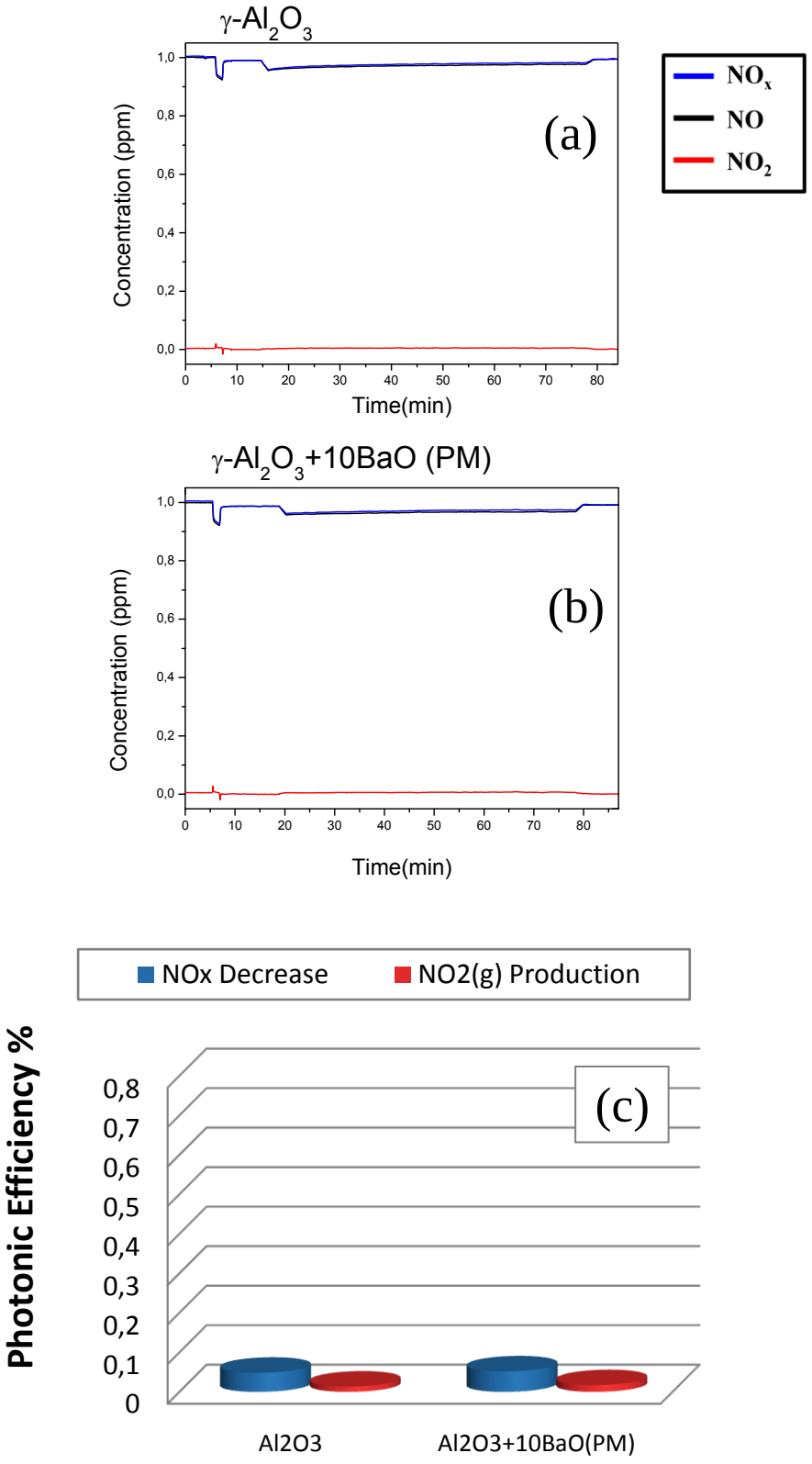

Figure 42. Performance plots of (a) pure γ-Al_2O_3 and (b) pure γ-Al_2O_3 +10% (w/w) BaO mixture. (c) The photonic efficiencies of the samples (a) and (b) in total NO_x abatement and $NO_{2(g)}$ production.

Figure 43 gives the performance plot of Degussa P25 TiO_2 and the comparison of photonic efficiencies of pure γ-Al_2O_3 , pure γ-Al_2O_3 +10% (w/w) BaO mixture and Degussa P25 TiO_2 in total NO_x abatement and $NO_{2(g)}$ production.

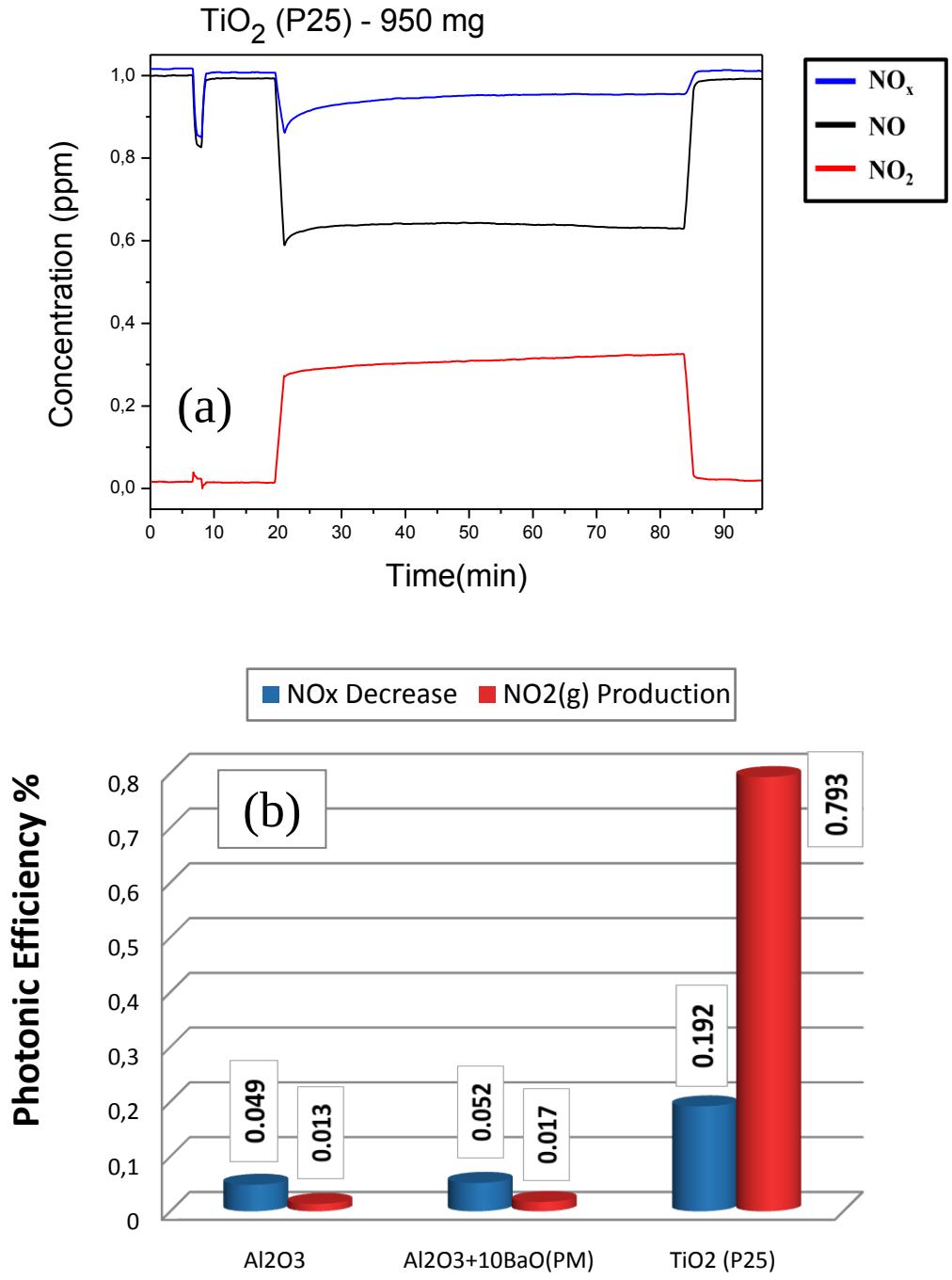

Figure 43. (a) Performance plot of Degussa P25 TiO_2 (b) The photonic efficiencies of pure γ-Al_2O_3 , γ-Al_2O_3 +10% (w/w) BaO mixture and Degussa P25 TiO_2 in total NO_x abatement and $NO_{2(g)}$ production.

As can be seen in Figure 43a, Degussa P25 has an excellent ability in NO oxidation. A sharp decrease in $NO_{(g)}$ concentration can be observed as soon as the UV lamp is turned on, accompanied by a fast increase in $NO_{2(g)}$ levels. This effect can also be seen in Figure 43b, where the efficiency of NO_2 production in Degussa P25 is almost 60 times higher than in pure γ-Al_2O_3 and γ-Al_2O_3 + 10% (w/w) BaO mixture. On the other hand, if the NO_x abatement efficiencies are taken into account, it is seen that P25 do not prevent NO pollution very effectively, because although it can oxidize NO into NO_2, further oxidization of NO_2 to NO_3^- and solid adsorption of the produced NO_3^- do not occur to a great extend and most of the oxidized NO is released as $NO_{2(g)}$. This result makes P25, or pure TiO_2 in that sense, a rather poor air purifier since it produces NO_2 (a more toxic gas than NO) as a result of the photocatalitic oxidation reaction on its surface. Therefore, it can be argued that the NO_x abatement efficiency of Degussa P25 is not exceedingly higher than that of pure γ-Al_2O_3 and γ-Al_2O_3 +10% (w/w) BaO mixture, even though these latter two samples do not possess significant photocatalytic ability.

Next, the performances of Ti/Al binary oxides are evaluated and compared to Degussa P25. Figure 44 shows the performance plots of thermally treated 0.25 Ti/Al samples. Note that neither uncalcined nor 0.25Ti/Al-800^oC sample has any photocatalytic ability. Although they can adsorp NO physically to some extend, these samples can not oxidize NO as a result of their amorphous structure. At 900^oC, where Raman measurements start showing some broad rutile bands, NO oxidation can also be observed with almost no concomitant $NO_{2(g)}$ production. At 950^oC, where Raman data shows slightly more distinctive rutile bands, NO oxidation efficiency seems to get more than 2-fold better compared to 0.25 Ti/Al-900 and 8-times better compared to the amorphous 0.25 Ti/Al-800. As a result, the $NO_{2(g)}$ production also increases but the total NO_x abatement is still 1.6 times better than the 900^oC sample. Finally at 1000^oC, the material becomes fully crystalline in rutile, but the sample loses much of its surface area which reduces the ability to store NO_x and the photonic efficiency of total NO_x abatement drops down to half of its value, compared to 0.25 Ti/Al-950. It should also be noted that the $NO_{2(g)}$ production efficiency becomes higher than NO_x abatement efficieny for 1000^oC calcination.

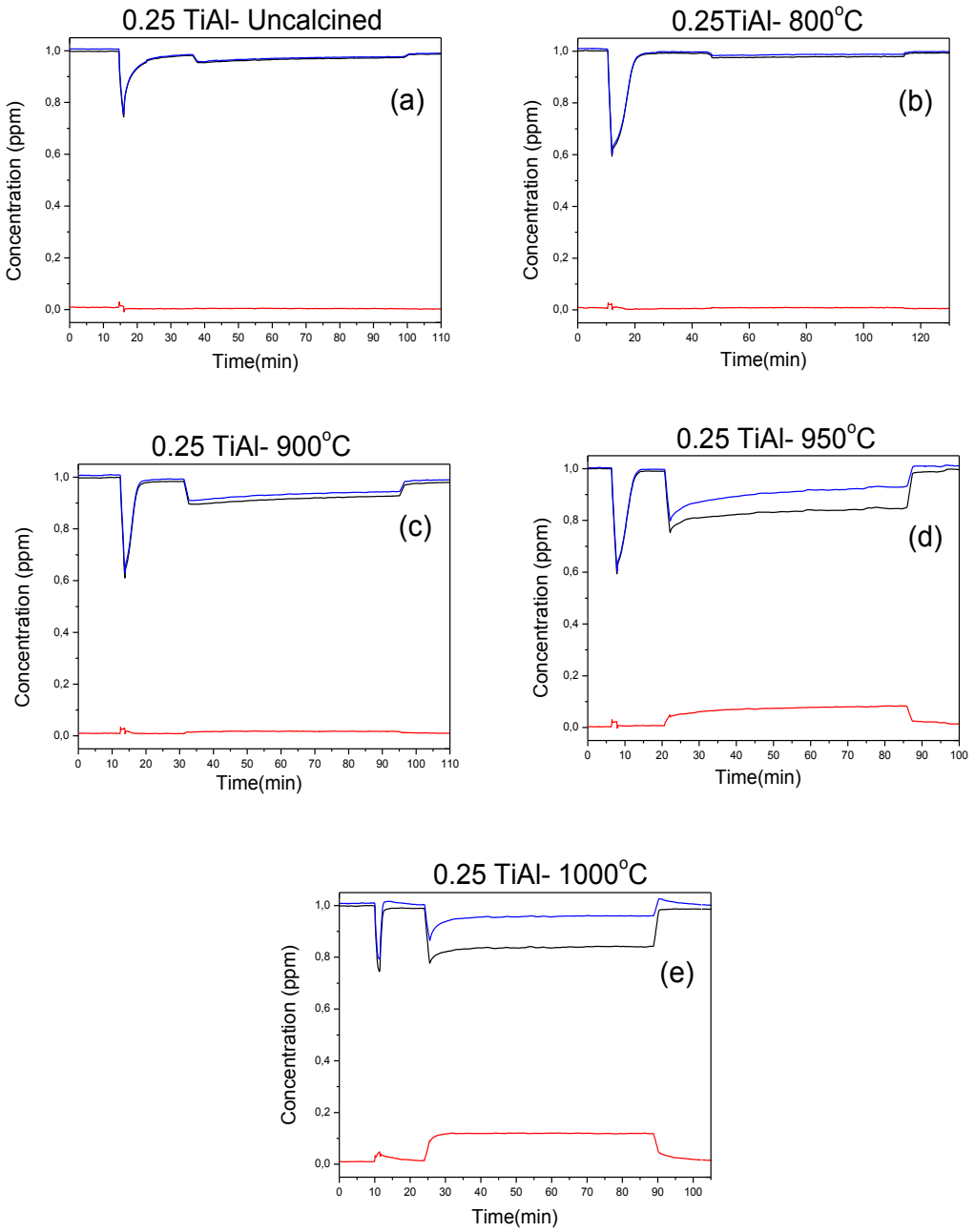

Figure 44. Performance plot s of 0.25 Ti/Al binary oxide samples:(a) uncalcined, calcined for 2h in air at (b)800°C, (c) 900°C, (d) 950°C, (e) 1000 °C.

Figure 45 presents the performance plots of thermally treated 0.5 Ti/Al samples. Similar to what is seen in 0.25 Ti/Al, amorphous 0.5 Ti/Al is not photocatalytically active. However, as observed in the corresponding XRD and Raman data, 0.5 Ti/Al suddenly crystallizes in rutile phase at 900^{o}C and the photocatalytic activity takes off immediately. At that temperature, NO_x abatement efficiency becomes more than 10-times higher than 0.5 Ti/Al-800. On the other hand, calcination to 1000^{o}C decreases both NO oxidation and NO_x storage efficiency, which is again similar to the behavior of 0.25 Ti/Al-1000 sample.

Finally in Figure 46, the performance plots of thermally treated 1.0 Ti/Al samples are given. As observed for other Ti:Al mole ratios, 1.0 Ti/Al samples that have amorphous titania are not photoactive either. 1.0 Ti/Al starts to present photocatalytic oxidation at around 800^{o}C. This is also the temperature where XRD and Raman measurements show the emergence of crystalline titania (27% anatase and 73% rutile). 1.0 Ti/Al-800 has a very strong oxidation ability and the NO_x abatement efficiency is 7-times higher than observed in 1.0 Ti/Al-600. Interestingly, the difference in the photocatalytic activity for 1.0 Ti/Al between 800^{o}C and 900^{o}C is less than that of the 0.5 Ti/Al-800 and 0.5 Ti/Al-900 samples, which shows that the amount of alumina in the Ti/Al composite has a direct effect in the NO_x storage capacity and efficiency. At 900^{o}C, 1.0 Ti/Al retains most its oxidative and absorptive efficiency, although the $NO_{2(g)}$ release is somewhat higher than in 800^{o}C sample. Ultimately, the 1.0 Ti/Al-1000 sample displays almost the same behavior with 0.5 Ti/Al-1000 and 0.25 Ti/Al-1000, in the sense that both of its oxidative and absorptive capacity become lower compared to 900^{o}C.

Figure 47 is a bar-graph of the photonic efficiencies of thermally treated 0.25 Ti/Al, 0.5 Ti/Al and 1.0 Ti/Al series for total NO_x abatement and $NO_{2(g)}$ production, in comparison with each other and also with Degussa P25 TiO_2. This graph simply reveals that first of all the addition of alumina definitely has a positive effect on the NO_x storage ability of Ti/Al binary oxides and secondly in all three Ti/Al mole ratios the best working samples (0.25 Ti/Al-950, 0.5 Ti/Al-900, 1.0 Ti/Al-800) are the ones that are calcined at temperatures where titania starts crystallization and possibly have intermediate crystallite sizes.

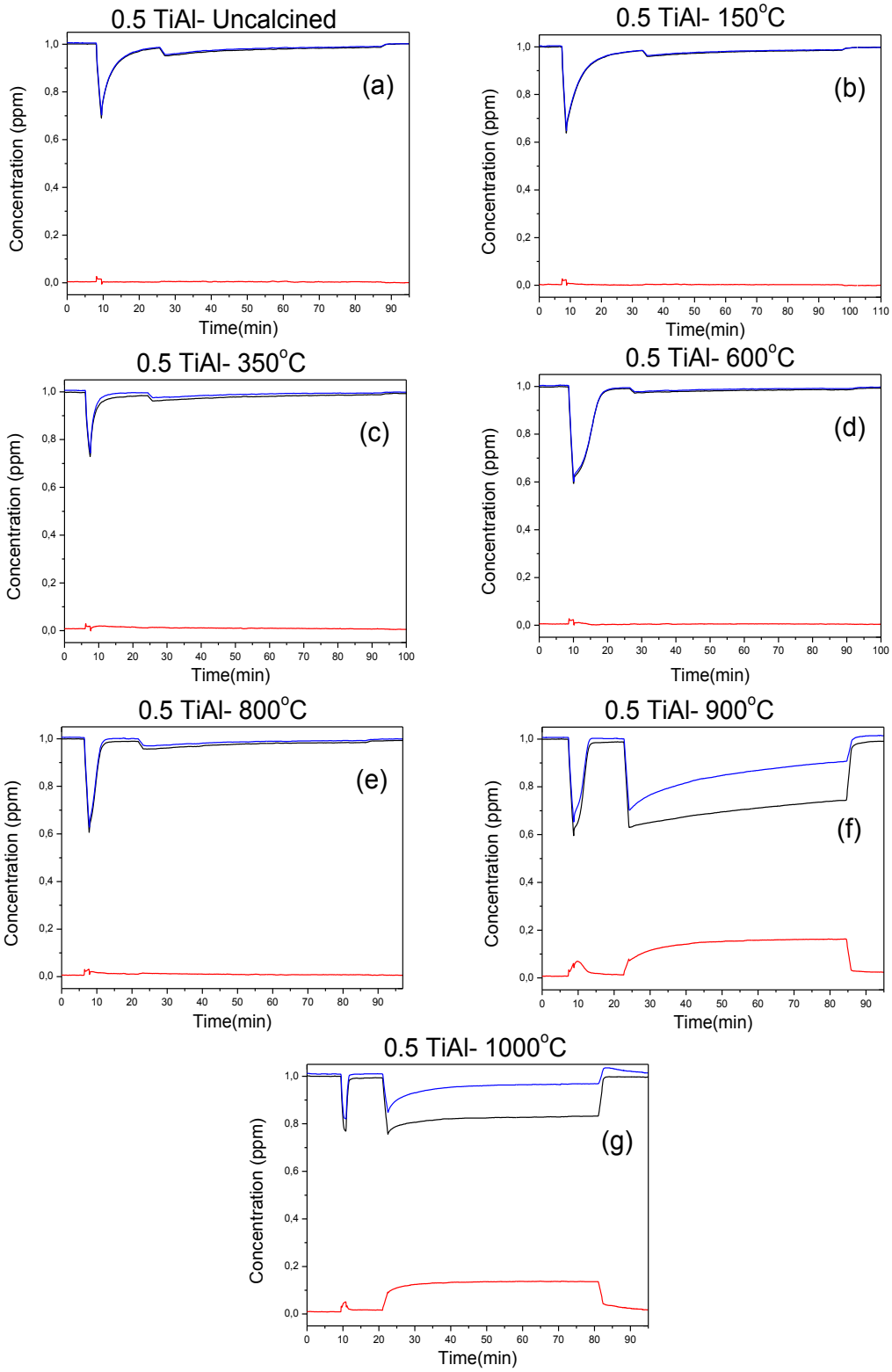

Figure 45. Performance plots of 0.5 Ti/Al binary oxide: (a) uncalcined and calcined for 2h in air at (b)150^{o}C, (c) 350^{o}C, (d) 600^{o}C, (e)800^{o}C, (f) 900^{o}C, (g) 1000^{o}C.

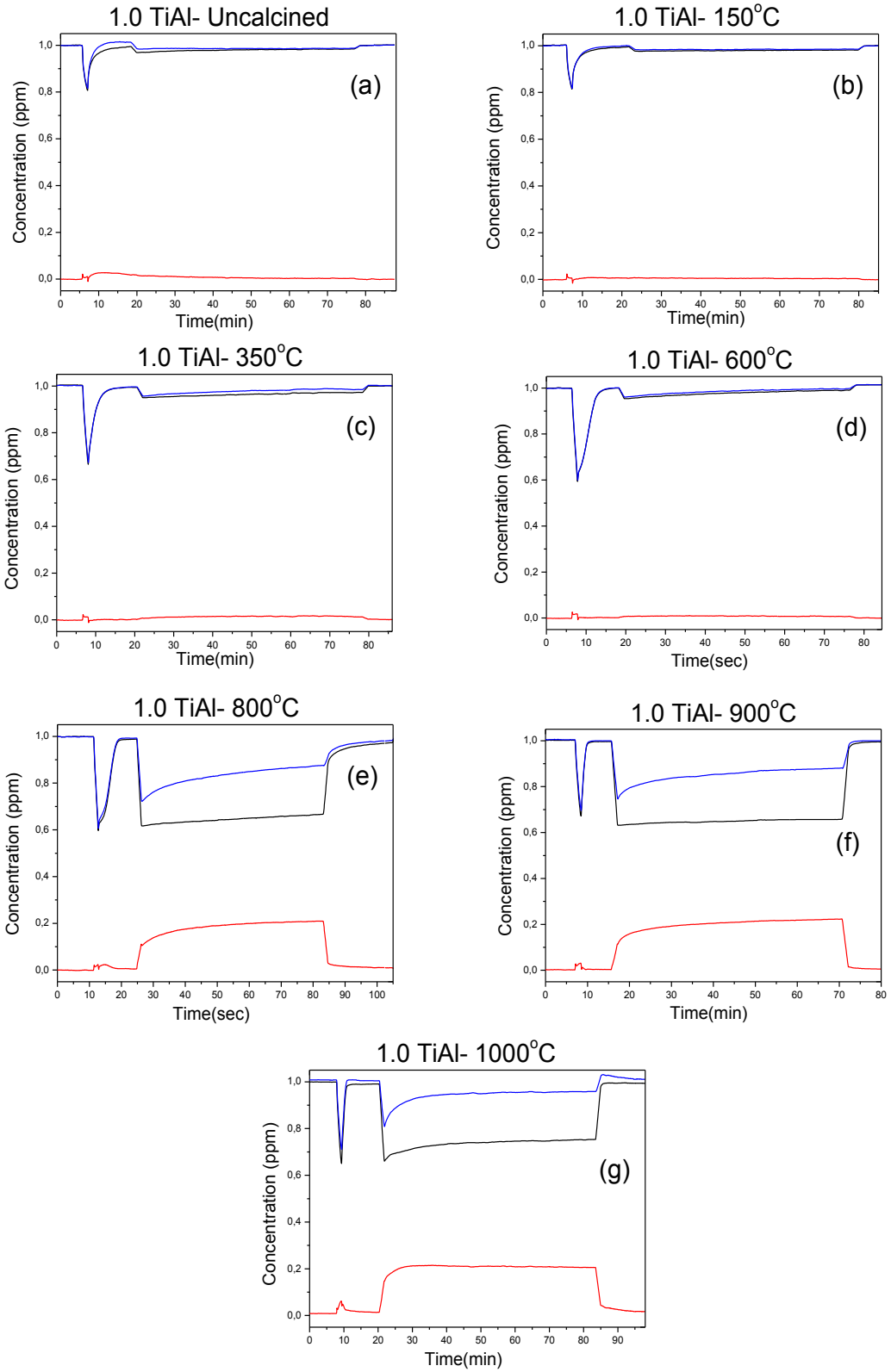

Figure 46. Performance plots of 1.0 Ti/Al binary oxide: (a) uncalcined and calcined for 2h in air at (b)150°C, (c) 350°C, (d) 600°C, (e)800°C, (f) 900°C (g) 1000°C.

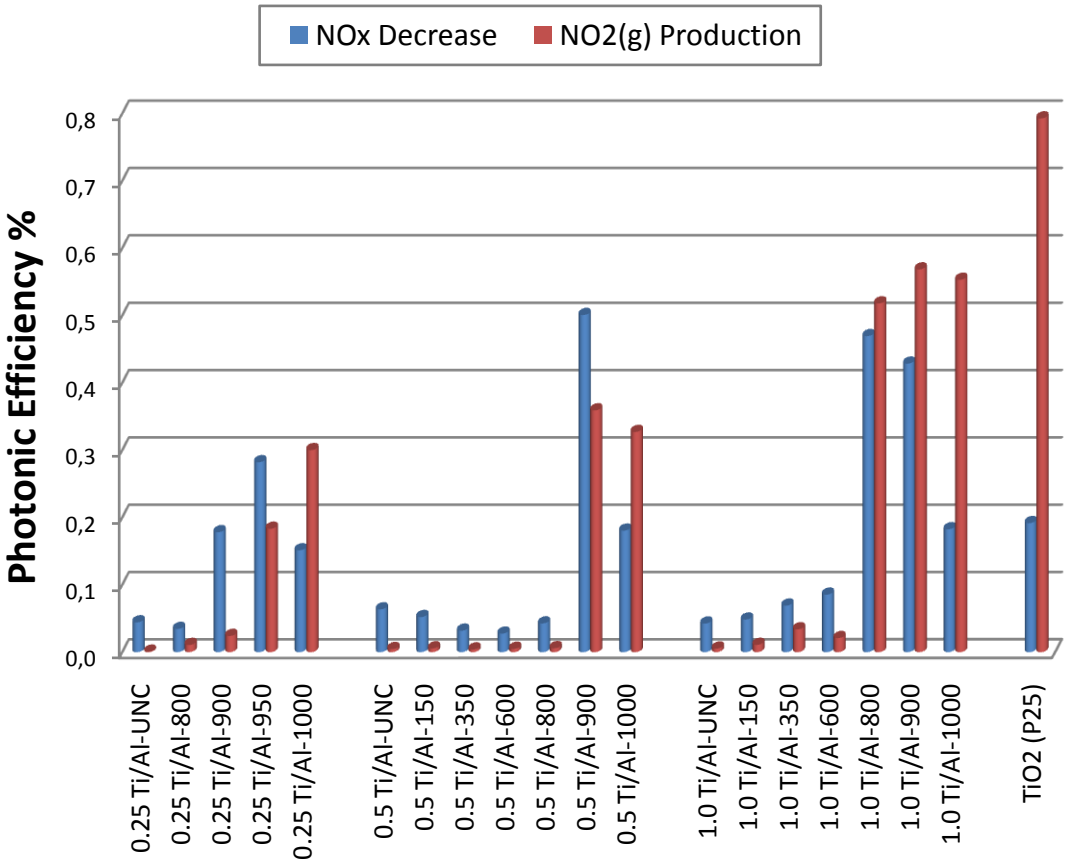

Figure 47. The photonic efficiencies of thermally treated 0.25 Ti/Al, 0.5 Ti/Al and 1.0 Ti/Al series for total NO_x abatement and $NO_{2(g)}$ production, in comparison with Degussa P25 TiO_2.

Figure 47 also shows that calcination at 1000^{o}C results in a drastic decrease in the absorptive capacities of Ti/Al samples and the total NO_x abatement efficiencies of all three Ti: Al mole ratios are cut down to half. It can be argued that this decrease occurs as a result of the drop in the specific surface areas, the γ–Al_2O_3 to α–Al_2O_3 phase transition and the growth in the TiO_2 crystallite sizes as a result of sintering and/or phase transformation. Among the photoactive samples, the highest NO_x absorption efficiency belongs to the ***0.5 Ti/Al-900*** sample and it can store total NO_x 2.6 times better than P25, while it emits less than half of the $NO_{2(g)}$ produced by the same amount of P25. These results clearly indicate that among the currently used Ti loadings, 0.5 Ti:Al mole ratio is an optimum point in terms of enhancing NO_x storage while hindering $NO_{2(g)}$ release into the atmosphere. Note that ***1.0 Ti/Al-800*** and ***1.0 Ti/Al-900*** samples also work much better than P25. Nonetheless, their $NO_{2(g)}$ release values are still unfavorably higher than that of 0.5 Ti/Al-900.

3.2 $M_xO/TiO_2/Al_2O_3$ Ternary oxides prepared via Impregnation

3.2.1 Structural Characterization of the $M_xO/TiO_2/Al_2O_3$ Ternary oxides

After evaluating the photocatalytic performances of Ti/Al binary oxides, it was seen that the addition of alumina had an enhancing effect on the NO_x storage capacity. The next step was the addition of an alkali/alkaline earth oxide NO_x storage component to the composite. Along these lines, the Ti/Al binary oxides were impregnated with 5 and 10% (w/w) alkali (Li, Na, K, Cs)/alkaline earth (Ca, Sr, Ba) metal nitrate salts. The freshly prepared samples were calcined at 700^oC for 4 h to decompose and desorb the nitrates and produce metal oxide domains. The calcination steps were perfromed under $Ar_{(g)}$ flow, rather than air, to prevent the formation of metal carbonates instead of oxides.

Among the Ti/Al series; ***0.5 Ti/Al-900***, ***1.0 Ti/Al-800*** and ***1.0 Ti/Al-900*** were chosen to be loaded with the metal oxides since these three photocatalysts showed the top three performances in terms of higher NO_x abatement and lower NO_2 production efficiencies compared to Degussa P25 (Figure 47).

3.2.1.1 XRD Analysis

X-ray diffraction patterns of the calcined Ti/Al+5/10M samples were examined to understand the crystal structures of these photocatalysts. Figure 48 shows the XRD data for 0.5 Ti/Al-900+5Ba and 0.5 Ti/Al-900+10Ba in comparison with the non-impregnated 0.5 Ti/Al-900.

First of all, $Ba(NO_3)_2$ seems to be generating cubic $BaTiO_3$ on top of titania domains after calcination at 700^oC and $BaTiO_3$ diffraction lines (JCPDS 00-005-0626) can be observed with even 5% $Ba(NO_3)_2$ loading. As the amount of Ba loading is increased to 10% (w/w), more lines belonging to the $BaTiO_3$ emerge, while the existing signals get sharper and more defined.

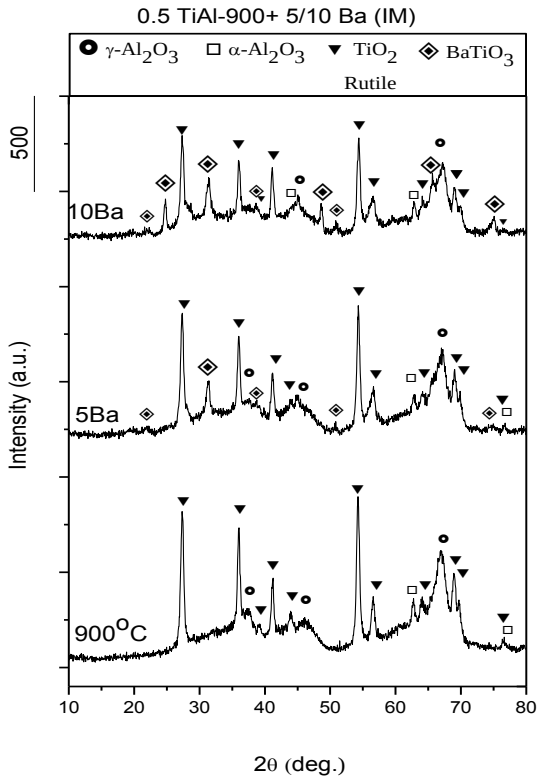

Figure 48. XRD patterns of 0.5 Ti/Al-900 sample that was impregnated with 5 and 10% (w/w) $Ba(NO_3)_2$ and calcined for 4 h at 700°C under Ar(g) atmosphere.

Since the $BaTiO_3$ formation consumes photocatalytically active TiO_2 domains of the Ti/Al binary oxide, its generation may not favor the photocatalytic oxidation ability of the sample. Similarly, ***1.0Ti/Al-800*** and ***1.0Ti/Al-900*** samples were impregnated with seven different alkali/alkaline earth metal salts (of Li, Na,K, Cs, Ca, Sr and Ba), in order to observe the behavior of each metal and to examine the effect of titanate formation on the photocatalytic performances of higher Ti mole ratio samples.

Figures 49 to 52 show the XRD patterns of 5 and 10% (w/w) alkali metal nitrate impregnated 1.0 Ti/Al-800/900 samples (Li, Na, K, Cs respectively) while Figures 53 to 55 give the XRD patterns of 5 and 10% (w/w) alkaline earth metal nitrate impregnated 1.0 Ti/Al-800/900 samples (Ca, Sr, and Ba respectively).

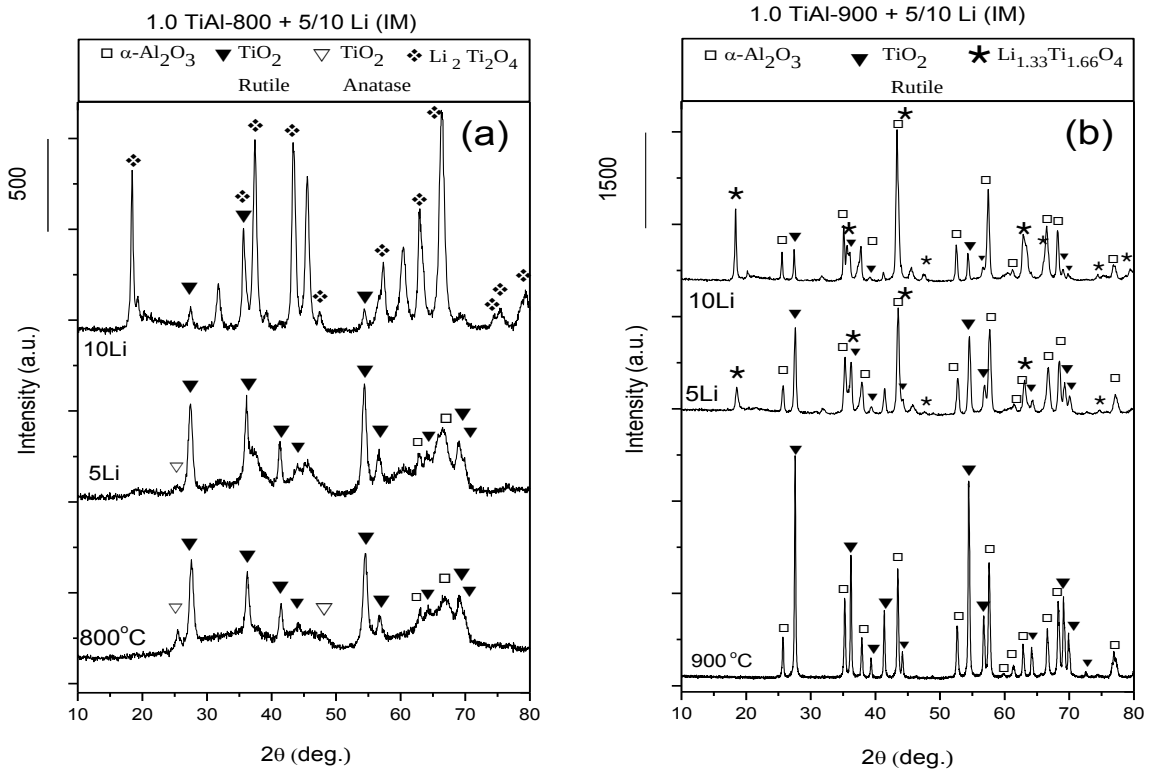

Figure 49. XRD patterns of (a) 1.0 Ti/Al-800 (b) 1.0 Ti/Al-900 samples that were impregnated with 5 and 10% (w/w) $LiNO_3$ and calcined for 4 h at 700°C under Ar(g) atmosphere.

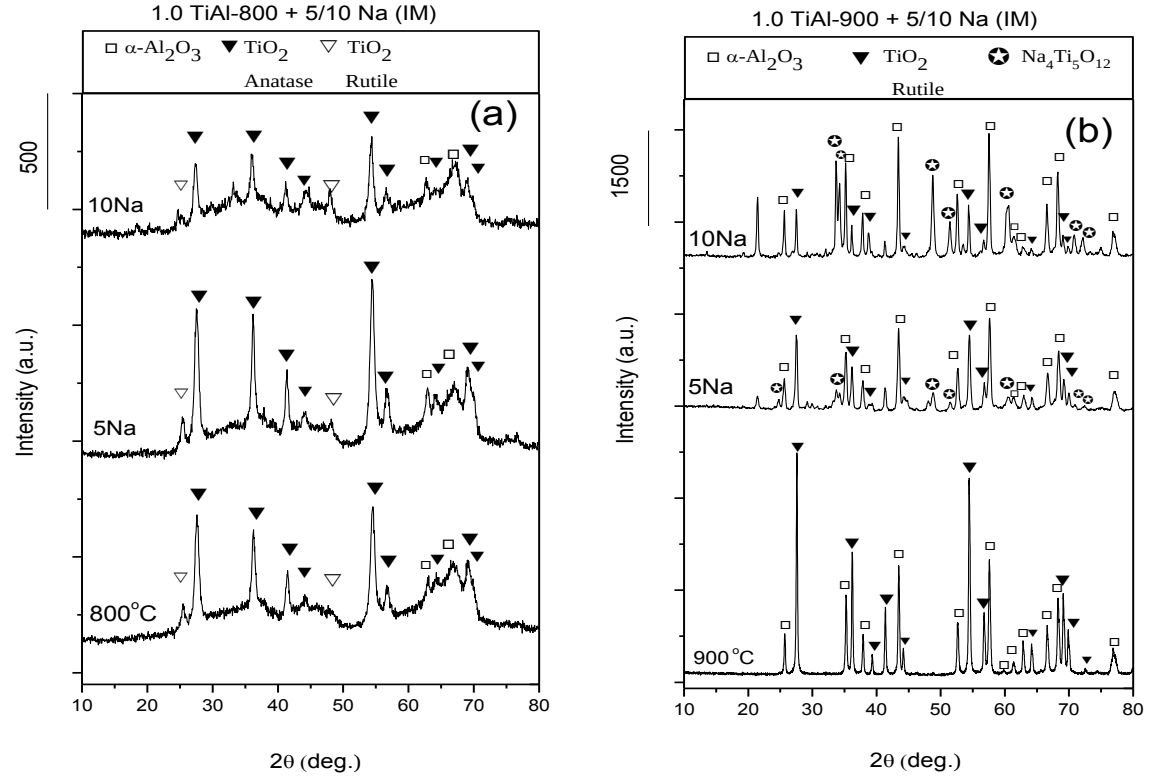

Figure 50. XRD patterns of (a) 1.0 Ti/Al-800 (b) 1.0 Ti/Al-900 samples that were impregnated with 5 and 10% (w/w) $NaNO_3$ and calcined for 4 h at 700°C under Ar(g) atmosphere.

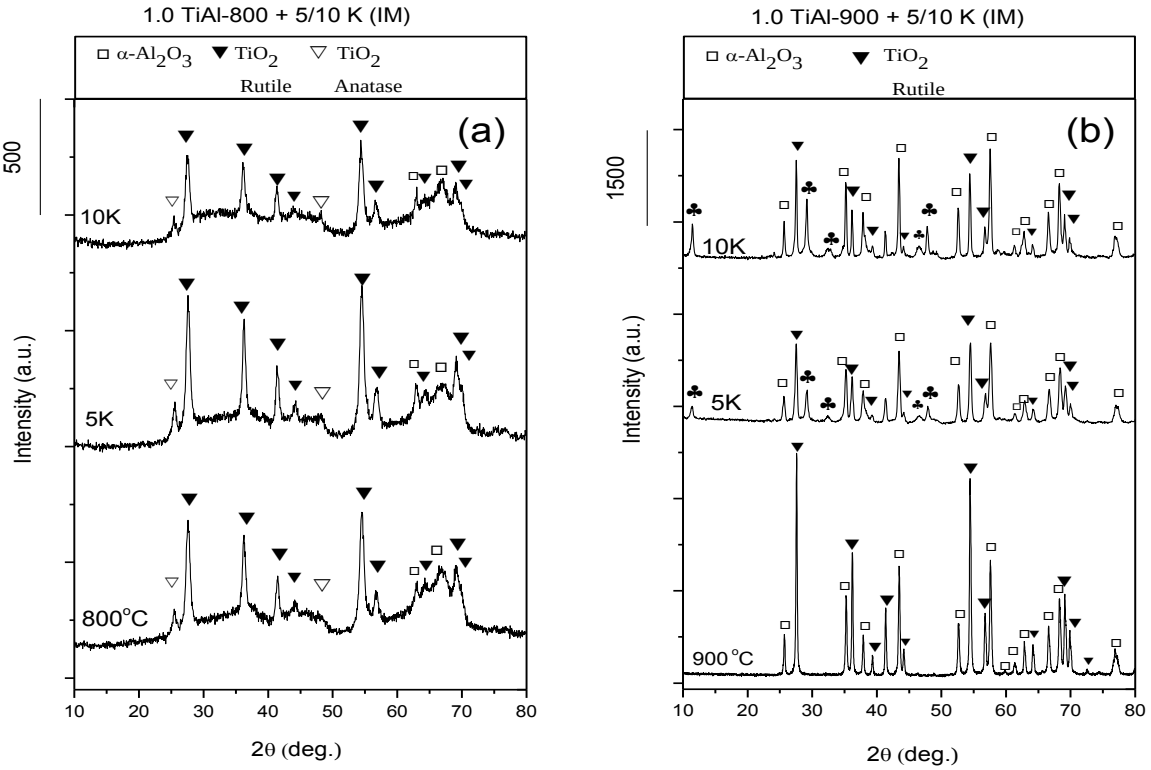

Figure 51. XRD patterns of (a) 1.0 Ti/Al-800 (b) 1.0 Ti/Al-900 samples that were impregnated with 5 and 10% (w/w) KNO_3 and calcined for 4 h at 700°C under Ar(g) atmosphere.

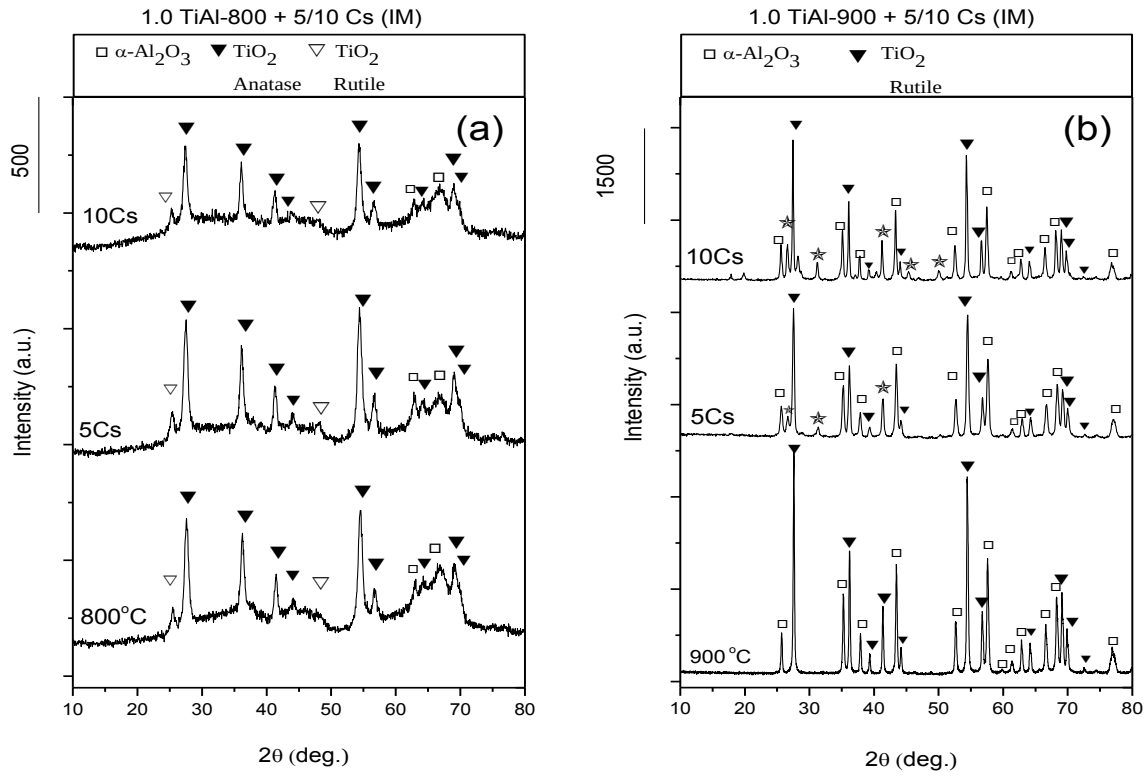

Figure 52. XRD patterns of (a) 1.0 Ti/Al-800 (b) 1.0 Ti/Al-900 samples that were impregnated with 5 and 10% (w/w) $CsNO_3$ and calcined for 4 h at 700°C under Ar(g) atmosphere.

In general, the addition of 5% (w/w) alkali metal nitrates to ***1.0 Ti/Al-800*** (Panel (a) in Figures 49-52) did not seem to affect the titania crystal structure to a great extend and no new diffraction lines could be discerned. In 10% addition, the intensities of titanium crystalline phase signals slightly decrease for Na, K and Cs. However, $LiNO_3$ addition completely diminishes the titanium crystalline phase by resulting in the formation of $Li_2Ti_2O_4$ (Figure 49-a, JCPDS 00-038-0270).

On the other hand, metal nitrate impregnation on ***1.0 Ti/Al-900*** (Panel (b) in Figures 49-52) has a more distinctive effect and the formation of metal titanates is visible even at 5% metal nitrate addition. For both 5 and 10% (w/w) addition, TiO_2 domains are mostly covered by the formation of $Li_{1.33}Ti_{1,66}O_4$ (Figure 49-b, JCPDS 00-026-1198) and $Na_4T_5O_{12}$ (Figure 50-b, JCPDS 00-037-0273). For potassium and cesium nitrates, the titanium diffraction patterns are also disturbed by the formation of new lines (marked by spade and star symbols in Figure 51 and Figure 52), however, these signals could not be assigned to any potassium or cesium nitrate/ oxide/titanate phase.

In Panel (a) of Figures 53-55, XRD patterns resulting from alkaline earth metal (Ca, S, Ba) nitrate impregnation on ***1.0 Ti/Al-800*** are given. Similar to what is seen in alkali metal nitrates, the addition of 5% (w/w) alkaline earth metal nitrates did not seem to affect the crystal structure to a great extend; however, 10% loading of $Ca(NO_3)_2$, $Sr(NO_3)_2$ and $Ba(NO_3)_2$ led to the formation of $CaTiO_3$ (Figure 53a, JCPDS 00-022-0153), $SrTiO_3$ (Figure 54a, JCPDS 00-005-0634) and $BaTiO_3$ (Figure 55a, JCPDS 00-005-0626), respectively.

Finally, XRD patterns resulting from the alkaline earth metal (Ca, S, Ba) nitrate impregnation on ***1.0 Ti/Al-900*** are shown in panel (b) of Figures 53-55. Here, the data tell that impregnation with both 5 and 10% (w/w) alkaline earth metal nitrate results in the generation of $CaTiO_3$ (Figure 53-b, JCPDS 00-022-0153), $SrTiO_3$ (Figure 54-b, JCPDS 00-005-0634) and $BaTiO_3$ (Figure 55-b, JCPDS 00-005-0626).

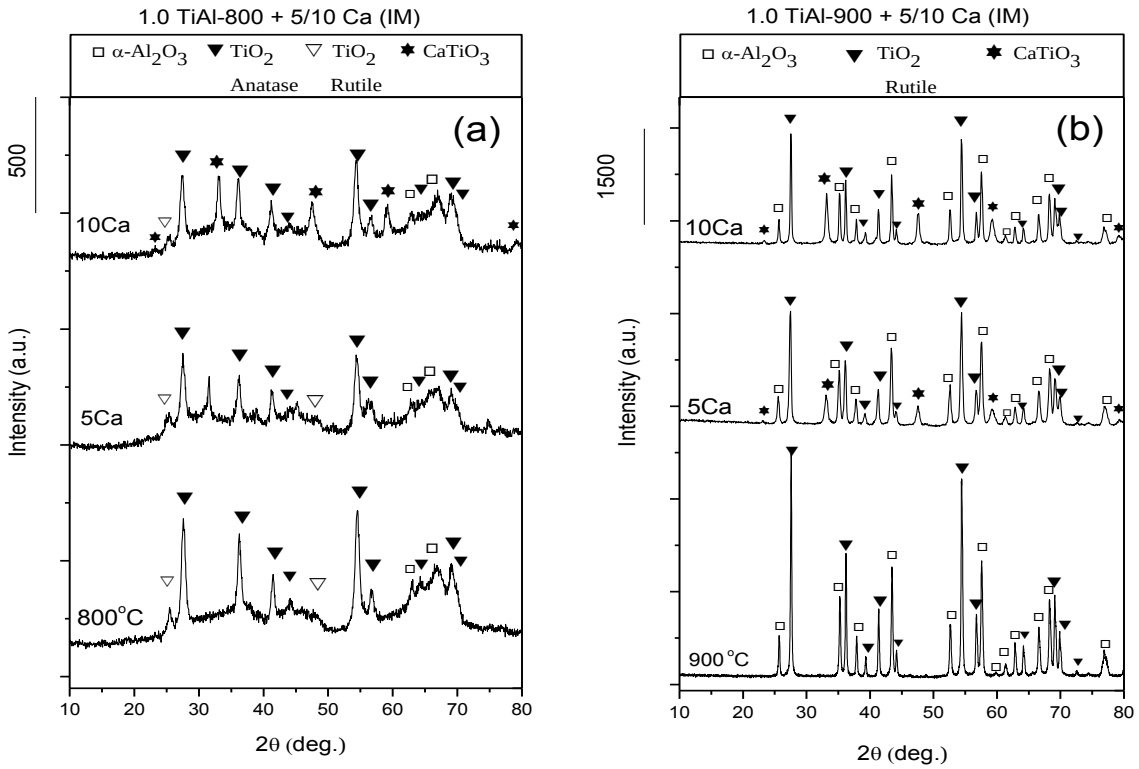

Figure 53. XRD patterns of (a) 1.0 Ti/Al-800 (b) 1.0 Ti/Al-900 samples that were impregnated with 5 and 10% (w/w) $Ca(NO_3)_2$ and calcined for 4 h at 700°C under Ar(g) atmosphere.

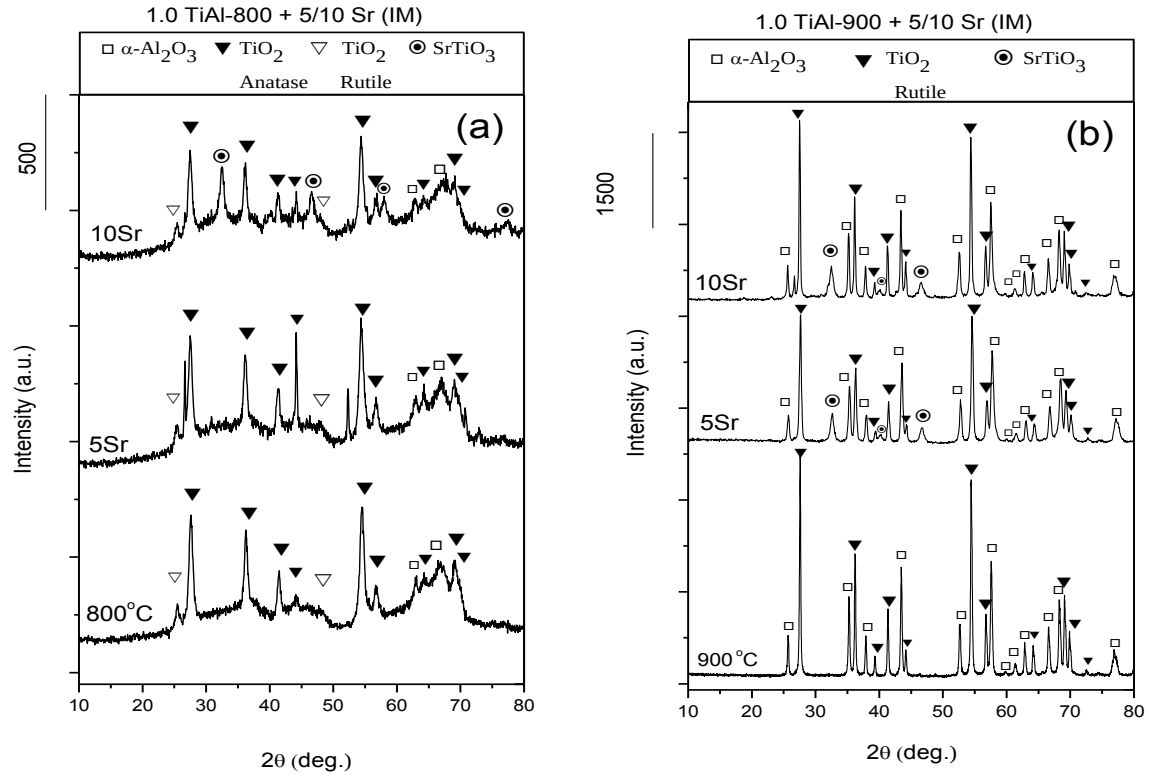

Figure 54. XRD patterns of (a) 1.0 Ti/Al-800 (b) 1.0 Ti/Al-900 samples that were impregnated with 5 and 10% (w/w) $Sr(NO_3)_2$ and calcined for 4 h at 700°C under Ar(g) atmosphere.

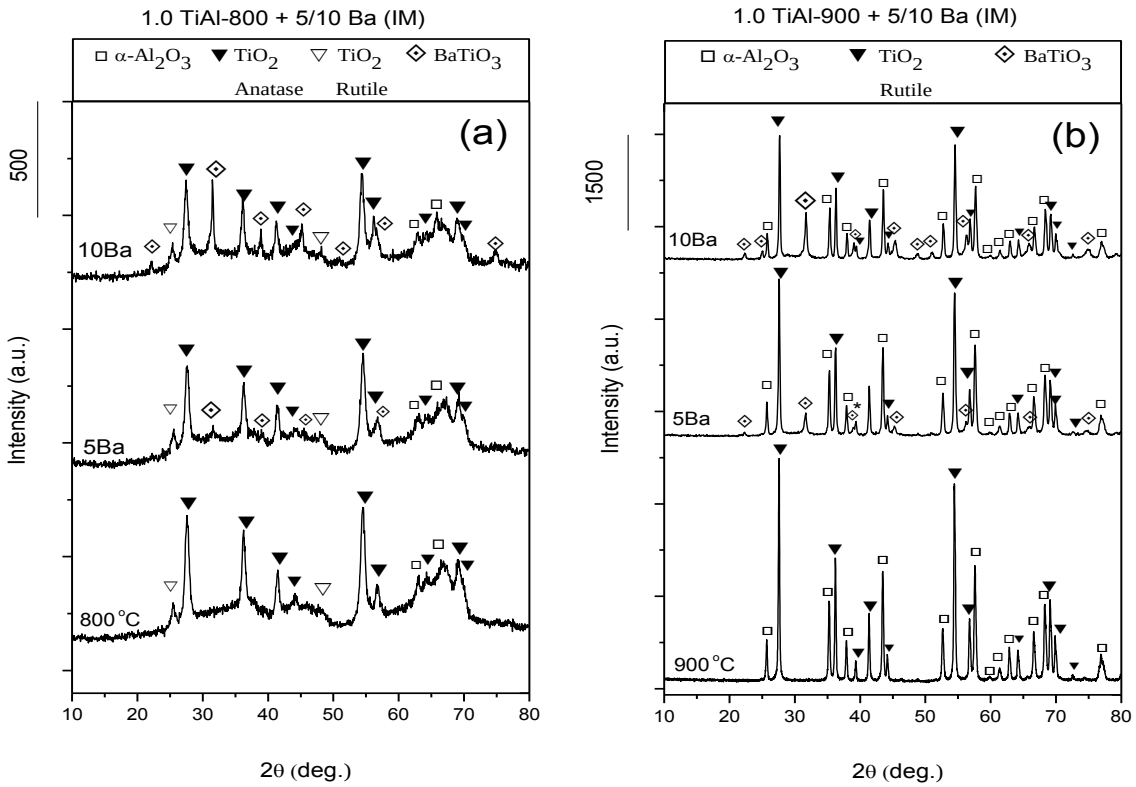

Figure 55. XRD patterns of (a) 1.0 Ti/Al-800 (b) 1.0 Ti/Al-900 samples that were impregnated with 5 and 10% (w/w) $Ba(NO_3)_2$ and calcined for 4 h at 700^oC under Ar(g) atmosphere.

3.2.1.2 Raman Experiments

In general, Raman measurements on the metal nitrate impregnated samples support the XRD findings and show that after calcination at 700^oC for four hours, the symmetric stretching vibration band of NO_3 around 1044-1069 cm^{-1} region (Figure 56) completely vanishes, meaning that the metal nitrate salts decompose into metal oxide.

The Raman spectra for ***0.5 Ti/Al-900+5Ba(IM)*** and ***0.5 Ti/Al-900+10Ba(IM)*** in comparison with the non-metal nitrate added 0.5 Ti/Al-900 are given in Figure 57. From these spectra, it is observed that even at 10% loading of $Ba(NO_3)_2$, Raman instrument cannot detect $BaTiO_3$ formation and only the rutile phase signals coming from crystalline TiO_2 are observed without much interference.

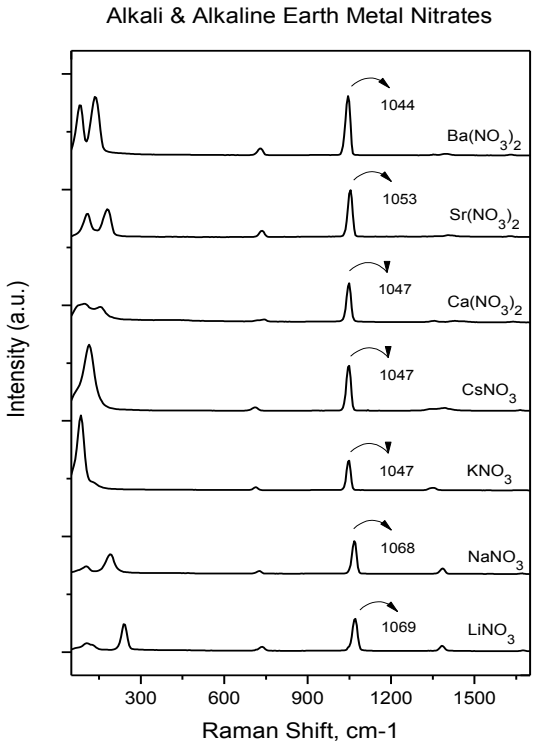

Figure 56. Raman spectra of the reference pure nitrate salts; $LiNO_3$, $NaNO_3$, KNO_3, $CsNO_3$, $Ca(NO_3)_2$, $Sr(NO_3)_2$, $Ba(NO_3)_2$.

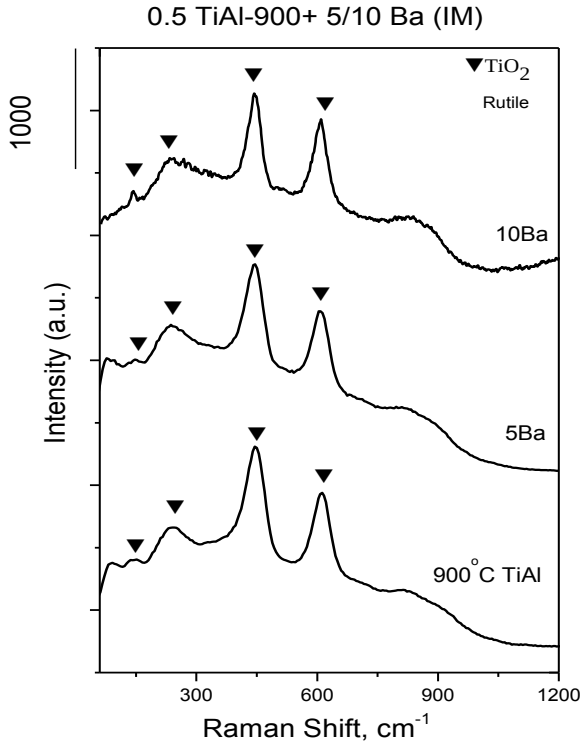

Figure 57. Raman spectra corresponding to the 1.0 Ti/Al samples that were impregnated with 5 and 10% (w/w) $Ba(NO_3)_2$ and calcined for 4 h at 700°C under Ar(g) atmosphere.

Figure 58 shows the Raman spectra corresponding to the ***1.0 Ti/Al-800/900*** samples that have been impregnated with 5 and 10% (w/w) $M(NO_3)_x$ and calcined for 4 h at 700^oC under $Ar_{(g)}$ atmosphere. Firstly, Panel (a) shows 5% addition of both alkali and alkaline earth metal nitrates to ***1.0 Ti/Al-800***. In this set of data, co-existing anatase and rutile phases of 1.0 Ti/Al-800 seems to remain intact. Only in 5% Li addition, the 144 cm^{-1} (E_g) and 516 cm^{-1} (A_{1g}+ B_{1g}) bands of the anatase phase are suppressed, which correlates with the XRD data (Figure 49a). Panel (b) shows that 10% addition of both alkali & alkaline earth metal nitrates to ***1.0 Ti/Al-800*** and here the disintegration of titania crystalline phase in Li loaded sample is even more apparent. In this spectrum, no bands for anatase can be detected and the rutile signals are pretty much disturbed by a newly emerging band around 670 cm^{-1}. The XRD data of 1.0 Ti/Al-800+10Li (IM), had displayed $Li_2Ti_2O_4$ formation which made almost all titania diffraction lines disappear, except for three signals at 27.4^o, 36.6 ^{o}, 54.3 ^{o} *2θ,* coming from the (110), (101) and (211) planes [106] of rutile (Figure 49b). Combining these two characterization techniques, one can argue that $Li_2Ti_2O_4$ formation starts either on anatase surfaces and consume them preferably or it can form on both types of titania crystalline surfaces but anatase signals are decreased earlier in the process since ***1.0 Ti/Al-800*** contains only a small amount of anatase. Figure 58b shows that for 10% loading of other metal oxides, TiO_2 crystalline structure in 1.0 Ti/Al-800 remains the same, which was also justified in XRD.

Figure 58c and 58d are the Raman spectra for ***1.0 Ti/Al-900*** and similar to the XRD results, these samples reveal mostly rutile phase before the metal nitrate impregnation but after metal loading, TiO_2 crystallinity in these samples is more disrupted than that was observed in 1.0 Ti/Al-800. Hence, the formation of metal titanates are possibly facilitated on highly ordered crystalline titania surfaces. Even at 5% loading, spectra of 1.0 Ti/Al-800+5Li(IM), +5Na(IM) and +5K(IM) show structural differences compared to the reference spectrum and at 10% loading, these three almost lose the characteristic rutile structure while several other Raman bands start to be detected. The inherent structure of 1.0 Ti/Al-900 is completely disrupted especially in 1.0 Ti/Al-900+10Na(IM) upon $Na_4Ti_5O_{12}$ formation. On the other hand, the addition of Cs, Ca, Sr and Ba nitrates do not change the Raman spectra of 1.0

Ti/Al-900 significantly although XRD data shows formation of metal titanates in these samples, too.

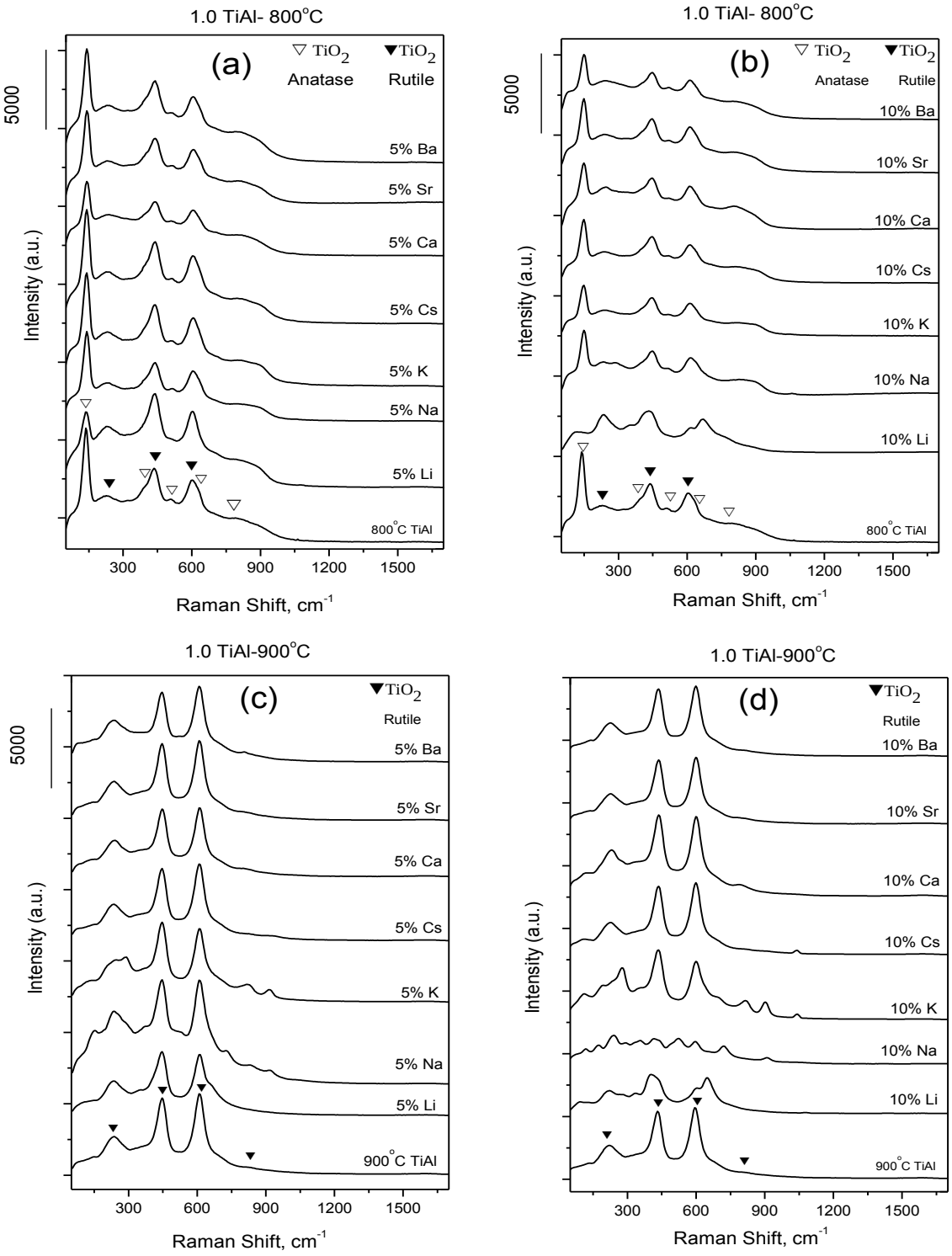

Figure 58. Raman spectra corresponding to the 1.0 Ti/Al samples that were impregnated with 5 and 10% (w/w) $M(NO_3)_x$ and calcined for 4 h at 700°C under Ar(g) atmosphere; (a) 1.0 Ti/Al-800+5%M (b) 1.0 Ti/Al-800+10%M (c) 1.0 Ti/Al-900+5%M (d) 1.0 Ti/Al-900+10%M

3.2.2 Photocatalytic Performance Experiments

Photocatalytic performance results of metal nitrate impregnated Ti/Al binary oxides for NO oxidation and storage were evaluated against Ti/Al binary oxides and Degussa P25. The interpretation of the performances have been achieved by comparing the photonic efficiencies of the samples towards total NO_x abatement and $NO_{2(g)}$ production/release.

Figure 59a and 59b gives the preformance plots of 0.5 Ti/Al-900 impregnated with 5 and 10% (w/w) $Ba(NO_3)_2$, respectively. The photonic efficiencies in NO_x abatement and $NO_{2(g)}$ production are also given in Figure 59c, where these values are compared with non-impregnated 0.5 Ti/Al-900 and Degussa P25. In terms of total NO_x abatement (storage), the metal-oxide impregnated samples achieve a better efficiency than Degussa P25 where 0.5 Ti/Al-900+5Ba(IM) stores 1.4 times and 0.5 Ti/Al-900-10Ba(IM) stores 1.2 times more NO_x than P25. What is better is that these samples produce a very limited amount of in return; such that 0.5 Ti/Al-900 +5Ba(IM) releases only 20% and 0.5 Ti/Al-900+10Ba(IM) emits only 15% of $NO_{2(g)}$ that P25 produces. From this perspective, one can argue that alkaline earth metal nitrate impregnation on Ti/Al is a progress on enhancing the NO_x storage capacity of pure titania. However, when compared with non-impregnated 0.5 Ti/Al-900, it is apparent that these samples have only half of the storage efficiency of the former material (Figure 59c). This phenomenon can be explained in the following way; barium titanate formation, detected in XRD, diminishes the oxidative activity of these samples since $BaTiO_3$ consumes the crystalline titania in Ti/Al composite and possibly covers these photocatalytically active sites. Without the oxidation, the catalyst cannot store much $NO_{(g)}$ directly from the gas phase and as a consequence, the NO_x abatement efficiency drops significantly. The much lower $NO_{2(g)}$ production efficiencies of the impregnated samples can also be based on their rather diminished oxidative power, instead of an extremely effective nitrate storage on $BaTiO_3$.

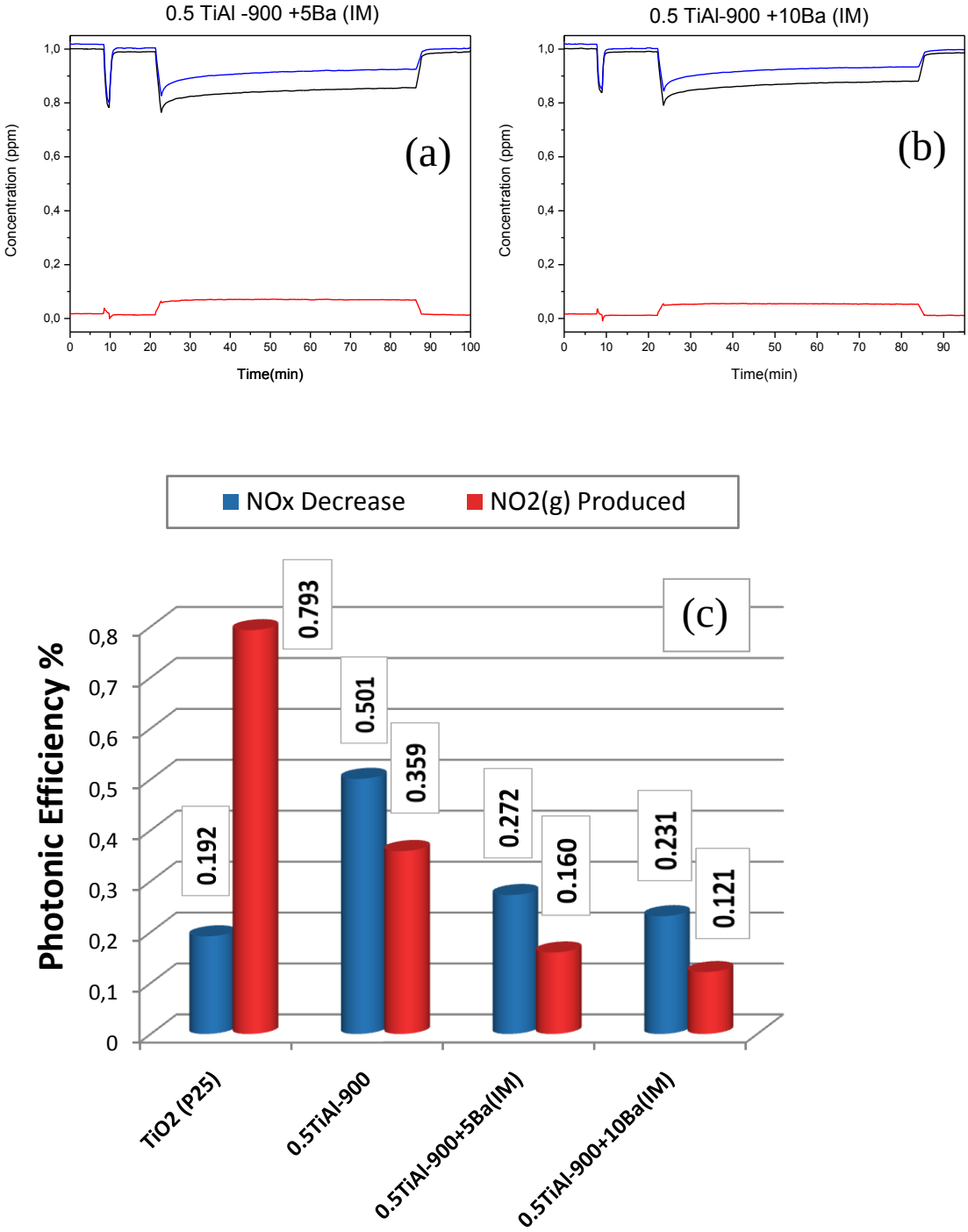

Figure 59. Performance plots of 0.5 Ti/Al-900 binary oxides that have been impregnated with (a) 5% (w/w) $Ba(NO_3)_2$, (b) 10 % (w/w) $Ba(NO_3)_2$ and calcined for 4 h at 700^{o}C under $Ar_{(g)}$ atmosphere. (c) The photonic efficiencies for total NO_x abatement and $NO_{2(g)}$ production in 1.0 Ti/Al-900 binary oxides that have been impregnated with 5 and 10% (w/w) $Ba(NO_3)_2$. The graph also presents the efficiencies of non-impregnated 0.5 Ti/Al-900 and Degussa P25 for comparison.

Next, the photocatalytic NO_x oxidation and storage efficiencies of 1.0 Ti/Al-800 and 900 that are impregnated with seven different alkali/alkaline earth metal nitrates are tested. Figures 60-61 belong to the preformance plots of ***1.0 Ti/Al-800+5/10M*** samples which are impregnated with either 5% or 10% (w/w) nitrate salts, while Figures 62-63 give the preformance plots of metal-nitrate impregnated ***1.0 Ti/Al-900+5/10M*** samples. The photonic efficiencies of ***1.0 Ti/Al-800+5/10M*** for total NO_x abatement and $NO_{2(g)}$ production in comparison with non-impregnated 1.0 Ti/Al-800 and Degussa P25 are also given as bar-graphs in Figure 64. Figure 65 is the comperative graph of photonic efficiencies of ***1.0 Ti/Al-900+5/10M*** for total NO_x abatement and $NO_{2(g)}$ production.

Similar to the 0.5 Ti/Al-900 case, metal nitrate impregnated samples performed worse than the non-impregnated referance Ti/Al samples (1.0 Ti/Al-800 and 1.0 Ti/Al-900) in terms of NO_x storage efficiency, which again might be attributed to the change in TiO_2 crystalline structure upon metal addition (metal titanate formation) and the loss of the active titania sites due to blocking by an alkali/alkaline earth metal oxide overlayer leading to a decrease in the photocatalytic oxidative capacity. Other than that, the photocatalytic activity of these series are also evaluated in three more respects:

I. Comparison of Group IA and Group IIA metals
II. Comparison of metal nitrate loading percentages
III. Comparison of 1.0 Ti/Al-800 and 1.0 Ti/Al-900 samples

When the behaviour of each metal is examined, alkaline earth metal (Ca, Sr, and especially Ba) impregnated samples are observed to have much higher NO_x storage capacities than alkali metal oxides (Li, Na, K, Cs) in both 1.0 Ti/Al-800/900 (Figures 64-65). Especially with 5%(w/w) addition, the alkaline earth metal group have much higher NO_x storage along with significantly lower $NO_{2(g)}$ production compared to Degussa P25. For these samples, the ease of $NO_{2(g)}$ storage as $NO_3^-{}_{(s)}$ ions depends on the standard Gibbs free energy of bulk $M(NO_3)_{x(s)}$ formation on the nitrate storing metal oxide. Therefore, the more negative Gibbs free energy of $M(NO_3)_{x(s)}$ formation on Group IIA metals compared to Group IA metals [107] may support our observation.

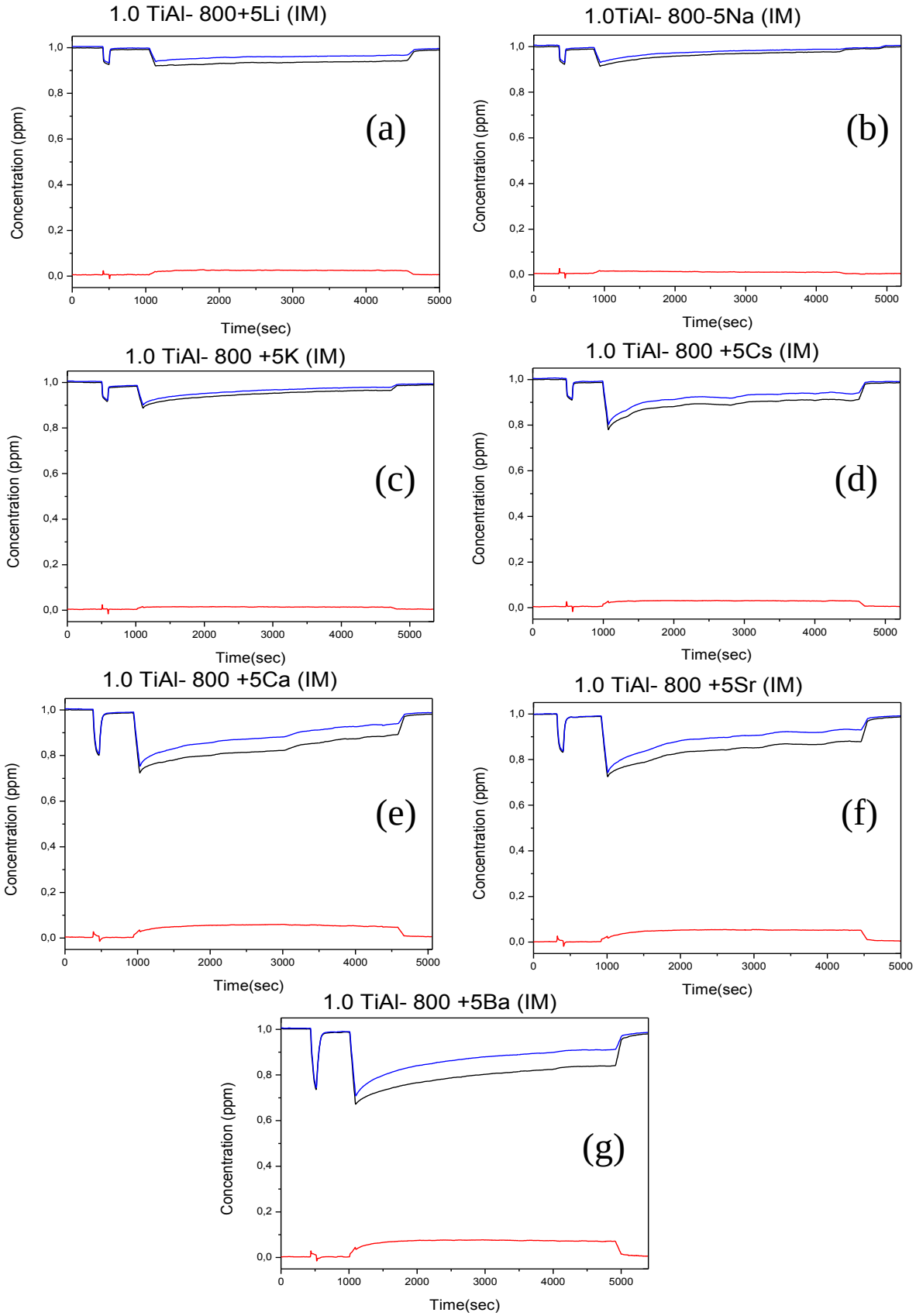

Figure 60. Performance plots of 1.0 Ti/Al-800 binary oxides that were impregnated with 5% (w/w) $M(NO_3)_x$ and calcined for 4 h at 700°C under Ar(g) atmosphere; (a) $LiNO_3$, (b) $NaNO_3$, (c) KNO_3, (d) $CsNO_3$, (e) $Ca(NO_3)_2$, (f) $Sr(NO_3)_2$, (g) $Ba(NO_3)_2$.

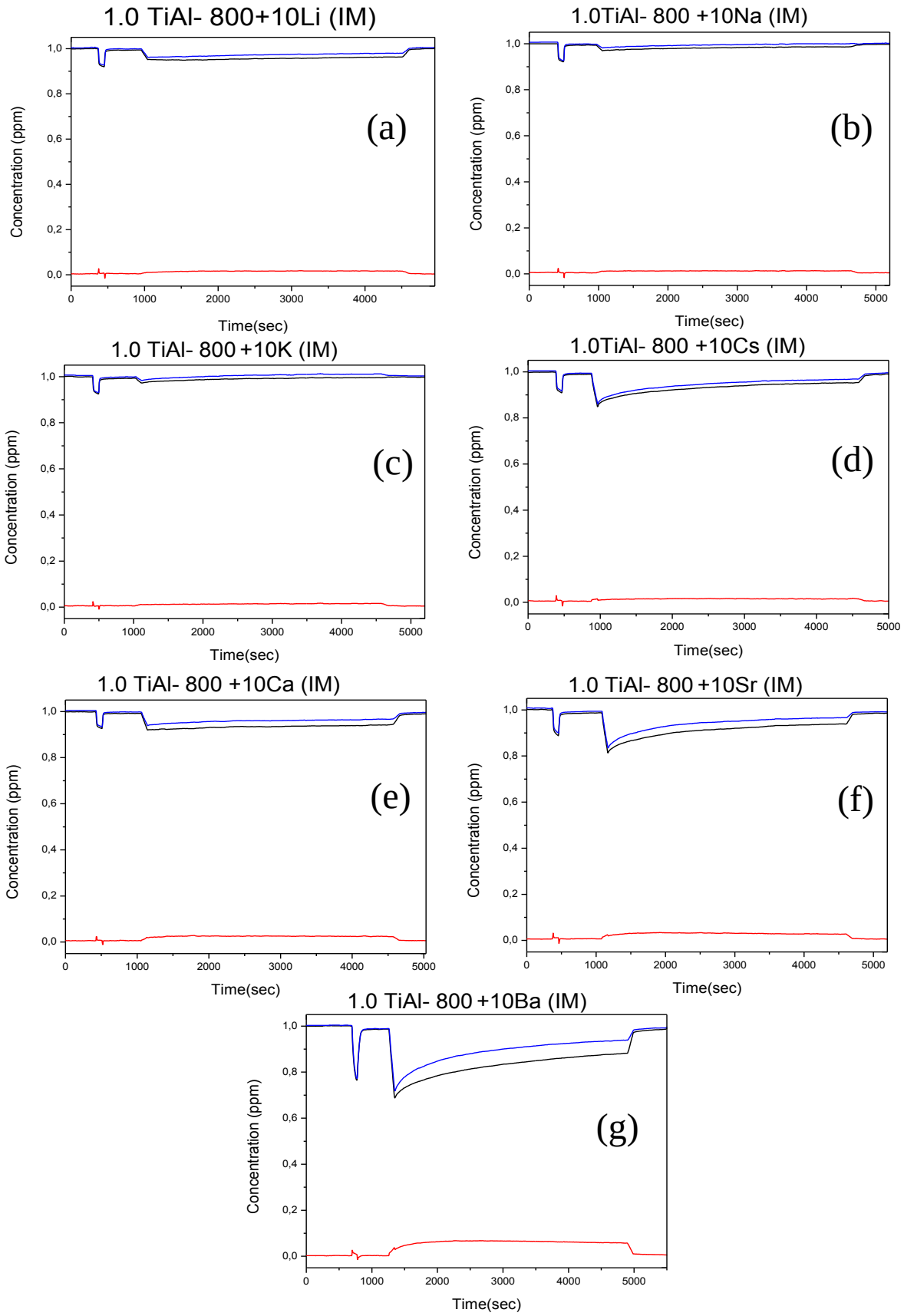

Figure 61. Performance plots of 1.0 Ti/Al-800 binary oxides that were impregnated with 10% (w/w) $M(NO_3)_x$ and calcined for 4 h at 700^oC under Ar(g) atmosphere; (a) $LiNO_3$, (b) $NaNO_3$, (c) KNO_3, (d) $CsNO_3$, (e) $Ca(NO_3)_2$, (f) $Sr(NO_3)_2$, (g) $Ba(NO_3)_2$.

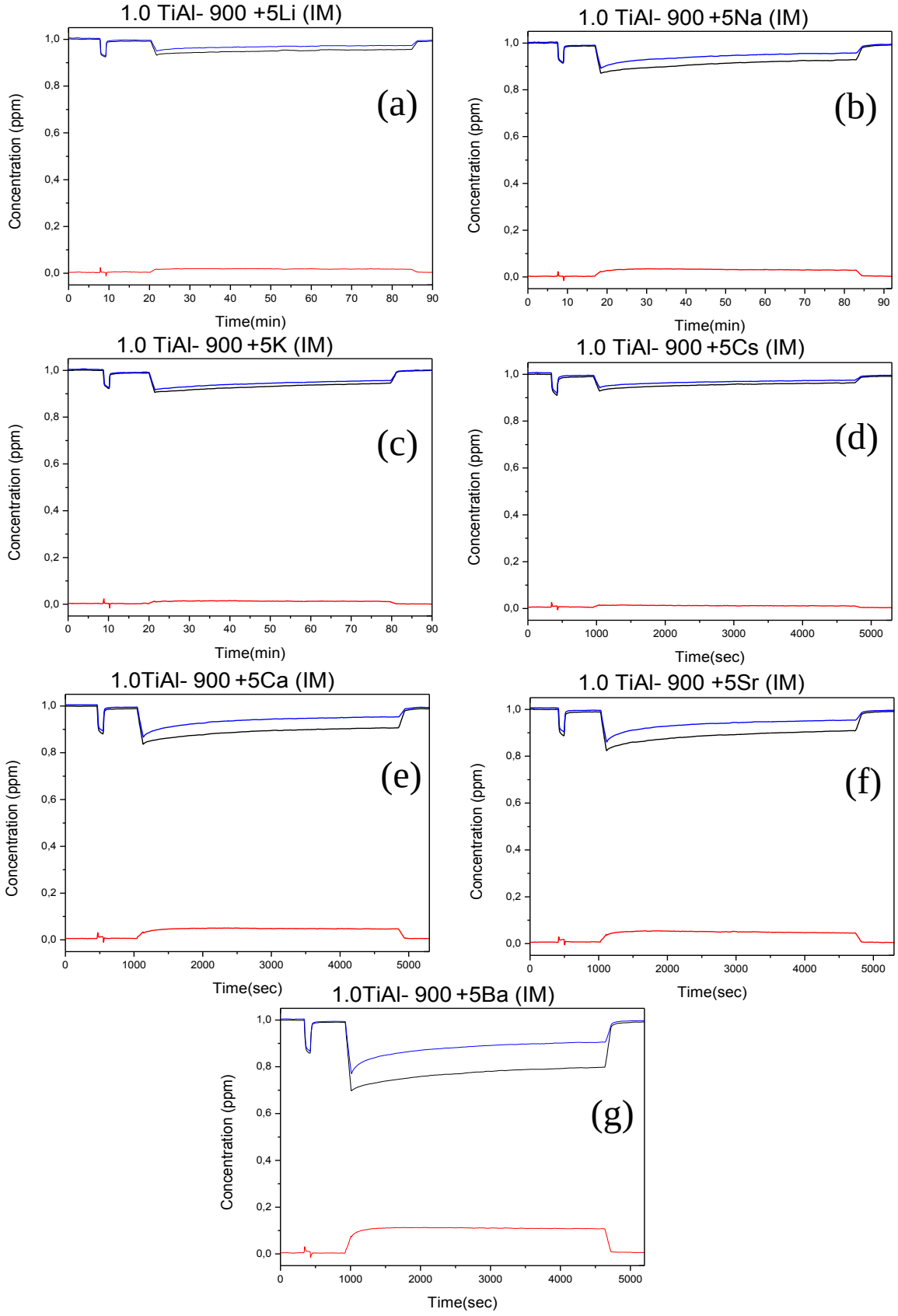

Figure 62. Performance plots of 1.0 Ti/Al-900 binary oxides that were impregnated with 5% (w/w) $M(NO_3)_x$ and calcined for 4 h at 700^{o}C under Ar(g) atmosphere; (a) $LiNO_3$, (b) $NaNO_3$, (c) KNO_3, (d) $CsNO_3$, (e) $Ca(NO_3)_2$, (f) $Sr(NO_3)_2$, (g) $Ba(NO_3)_2$.

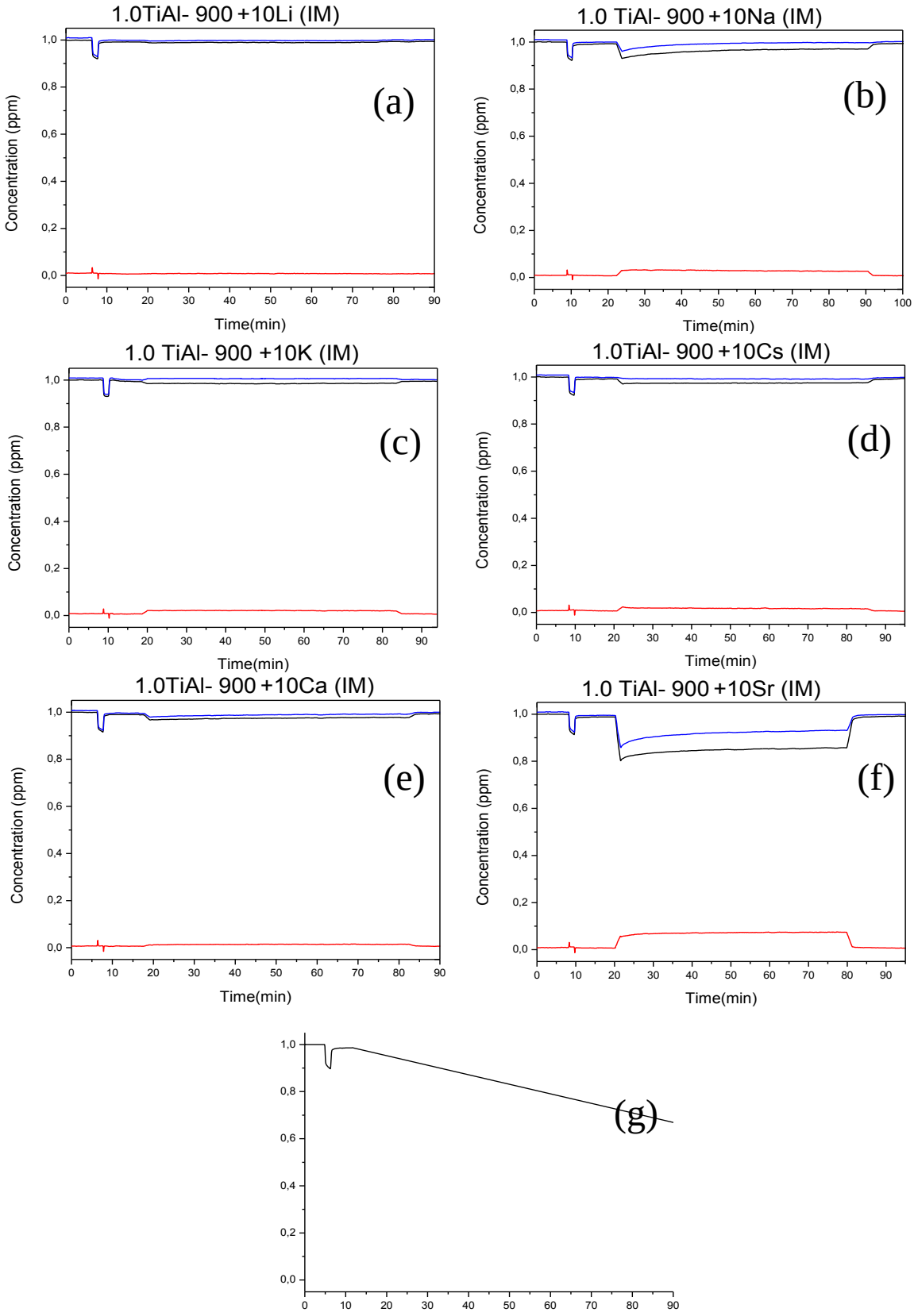

Figure 63. Performance plots of 1.0 Ti/Al-900 binary oxides that were impregnated with 5% (w/w) $M(NO_3)_x$ and calcined for 4 h at 700^{o}C under Ar(g) atmosphere; (a) $LiNO_3$, (b) $NaNO_3$, (c) KNO_3, (d) $CsNO_3$, (e) $Ca(NO_3)_2$, (f) $Sr(NO_3)_2$, (g) $Ba(NO_3)_2$.

When the metal nitrate loading percentages are compared, the data show that both ***1.0 Ti/Al-800+10M (IM)*** and ***1.0 Ti/Al-900+10M (IM)*** perform much poorer than ***1.0 Ti/Al-800/900+5M (IM)*** in NO_x abatement. This measurement is reasonable since when the loading of alkali/alkaline earth metal in the composite increases, the amount of metal titanate formation and the extent of the burial/blocking of active titania sites also increase, hindering the photooxidation reaction.

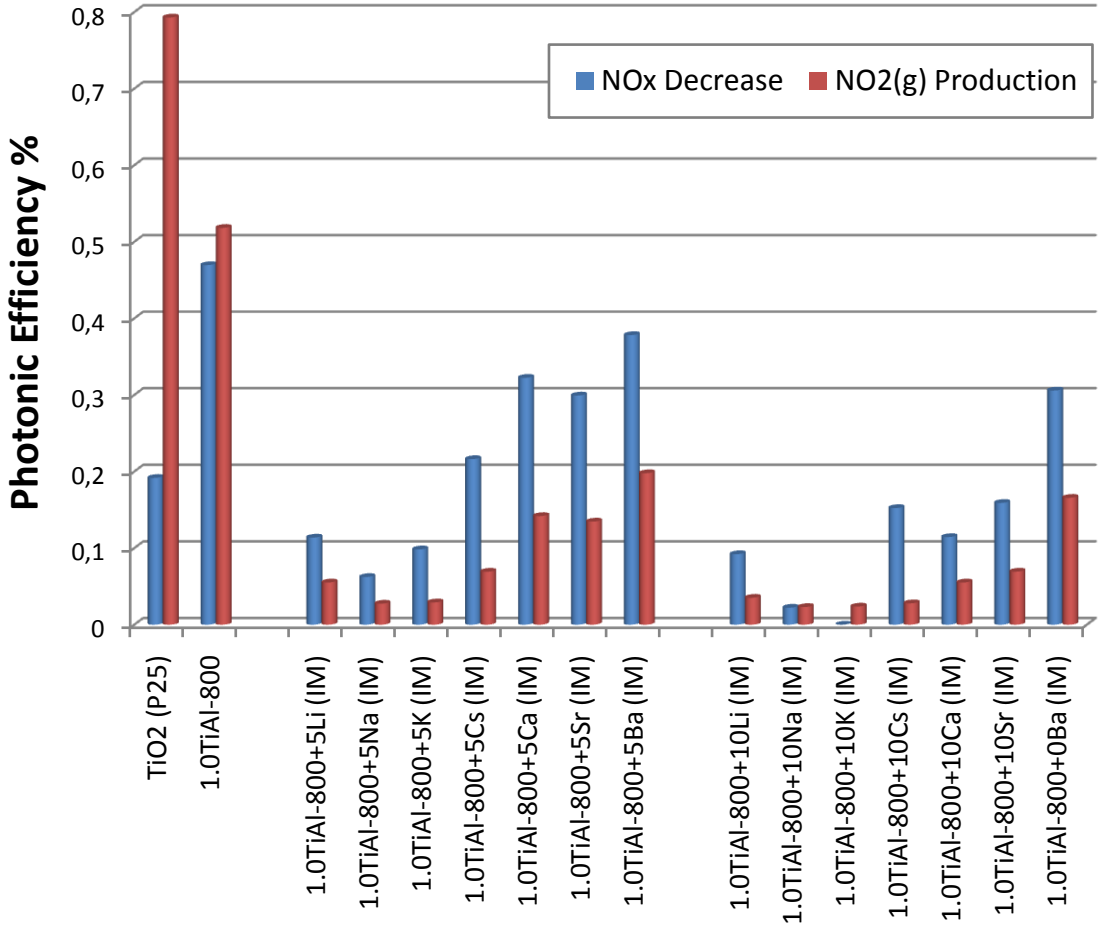

Figure 64. The photonic efficiencies for total NO_x abatement and $NO_{2(g)}$ production in 1.0 Ti/Al-800 binary oxides that were impregnated with 5 and 10% (w/w) $M(NO_3)_x$ and calcined for 4 h at 700°C under $Ar_{(g)}$ atmosphere. The graph also presents the photonic efficiencies of non-impregnated 1.0 Ti/Al-800 and Degussa P25 for comparison.

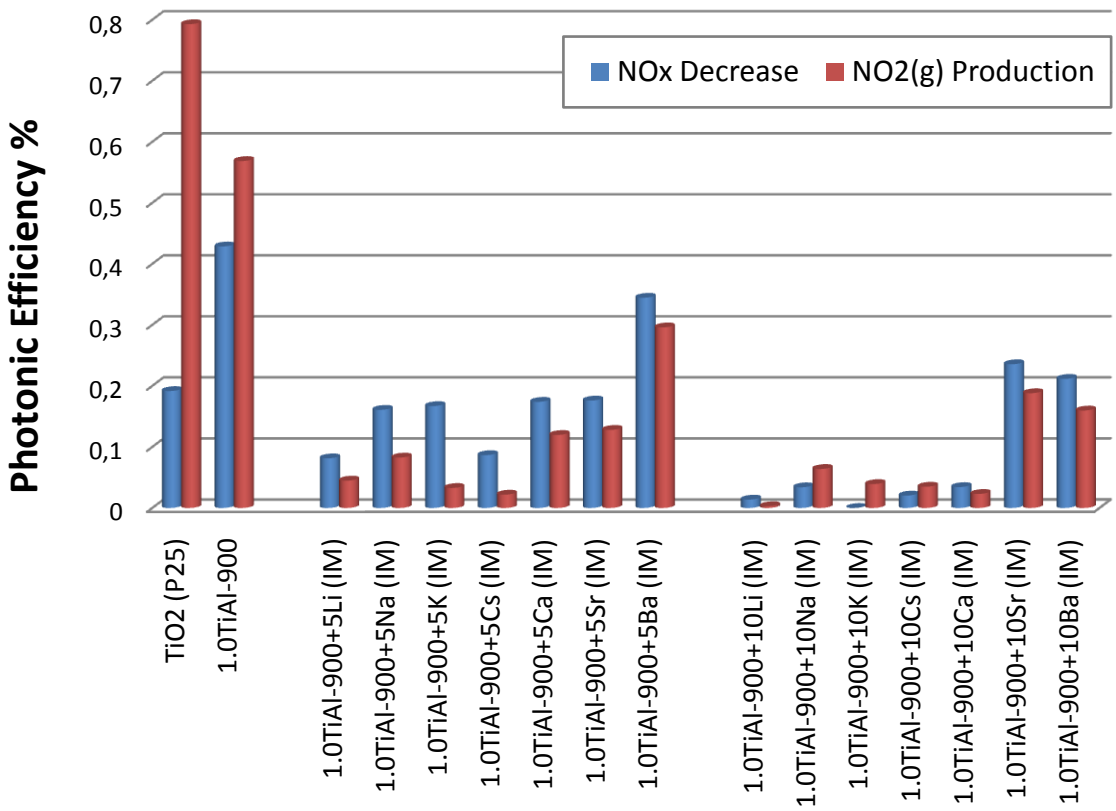

Figure 65. The photonic efficiencies for total NO_x abatement and $NO_{2(g)}$ production in 1.0 Ti/Al-900 binary oxides that were impregnated with 5 and 10% (w/w) $M(NO_3)_x$ and calcined for 4 h at 700°C under $Ar_{(g)}$ atmosphere. The graph also presents the efficiencies of non-impregnated 1.0 Ti/Al-900 and Degussa P25 for comparison.

Finally, the comparison between the impregnated ***1.0-Ti/Al-800+5/10M (IM)*** and ***1.0-Ti/Al+900-5/10M (IM)*** samples (Figures 64 vs. 65) suggests that photocatalytic NO_x oxidation and storage is better in 1.0-Ti/Al-800+5/10M (IM), especially on the Group IIA metal oxides. This observation may have multiple roots. First, even the non-impregnated 1.0-Ti/Al-800 is a better catalyst than 1.0-Ti/Al-900, probably as a result of its anatase-rutile mixed phase structure (Figures 39c and 41d) and/or its higher surface area (Table 13). Thus, the impregnated samples may be simply reflecting this trend. Other than that, a larger amount of metal titanate formation upon metal nitrate impregnation on 1.0-Ti/Al-900 (justified by both XRD and Raman measurements) may also be leading to a lower NO_x oxidation and storage capacity compared to the 1.0-Ti/Al-800 samples.

3.3 $M_xO/TiO_2/Al_2O_3$ Ternary oxides prepared via Physical Mixing

3.3.1 Photocatalytic Performance Experiments

When the performance tests of the metal-nitrate impregnated Ti/Al failed to produce higher NO_x storage efficiencies compared to the non-impregnated Ti/Al, it was inferred that the metal titanate formation on top of the photocatalytically active titania domains impeded the photocatalytic oxidation and thus storage of the atmospheric $NO_{x(g)}$. Consequently, another route of adding the nitrate adsorbing storage component to the Ti/Al binary oxide have been investigated and in this regard, physical mixture of an alkaline earth metal oxide with the photoactive Ti/Al binary oxide has been proposed as an alternative pathway to obtain the three-component photocatalyst. BaO has been chosen as the representative metal oxide for physical mixing since $Ba(NO_3)_2$ impregnated Ti/Al yielded the best storage activity among the metal oxide added samples. As the base photocatalyst 0.5-Ti/Al-900, 1.0-Ti/Al-800, 1.0-Ti/Al-900 have been utilized and mixed with 5 and 10% (w/w) BaO powder (>99%, Sigma Aldrich). Apart from the sol-gel synthesized Ti/Al samples, Degussa P25 has also been mixed with commercially available alumina in 0.5 TiO_2:Al_2O_3 mole ratio and finally this mixture was also combined with either 5 or 10% (w/w) BaO powder. This preparation route was chosen in order to provide a physical interface between TiO_2 and BaO domains, so that the $NO_{(g)}$ that is oxidized on TiO_2 surface can subsequently be stored on the nearby BaO sites without any hinderance.

Figures 66 and 67 show the performance plots of Ti/Al + BaO, P25+γ-Al_2O_3 and P25+γ-Al_2O_3+BaO physical mixtures while Figure 68 displays their photonic efficiencies in total NO_x abatement and $NO_{2(g)}$ production. As expected, the photocatalytic oxidation and storage performances of these mixed-oxide samples are much better than both Degussa P25 and the Ti/Al.

Among the physically mixed Ti/Al samples, 0.5Ti/Al-900+5BaO(PM) shows both a very high NO_x storage efficiency (1.5 times higher than 0.5Ti/Al-900 and 3.8 times higher than Degussa P25) while releasing a significantly low amount of $NO_{2(g)}$ (about 37% of 0.5Ti/Al-900 and 17% of Degussa P25) .

Samples 1.0Ti/Al-800+5/10BaO(PM) and 1.0Ti/Al-900+5/10BaO(PM) also purify NO pollution very effectively, numerically speaking, several times more efficiently than both Degussa 25 and 1.0Ti/Al-800-900 binary oxides. Similar to 0.5Ti/Al-900+5BaO(PM), these photocatalysts also emit very limited amounts of gaseous NO_2, not as a result of hindered oxidative activity but owing to their substancial NO_x storage capacities.

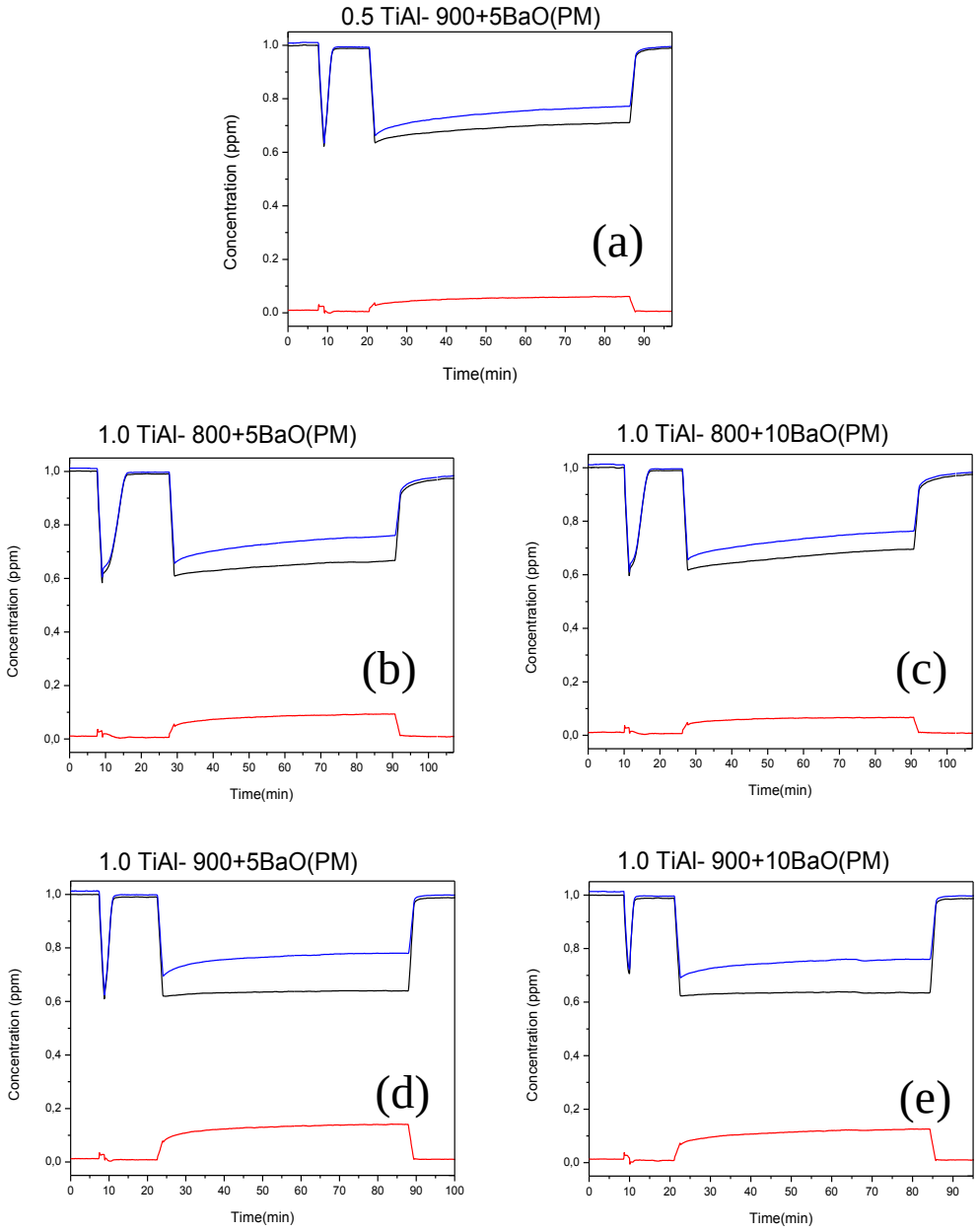

Figure 66. Performance plots of Ti/Al and BaO physical mixtures in the following compositions (a) 0.5-Ti/Al-900+ 5BaO(PM), (b) 1.0-Ti/Al-800+ 5BaO(PM), (c) 1.0-Ti/Al-900+ 10BaO(PM) , (d) 1.0-Ti/Al-900+ 5BaO(PM), (e) 1.05-Ti/Al-900+ 10% BaO(PM)

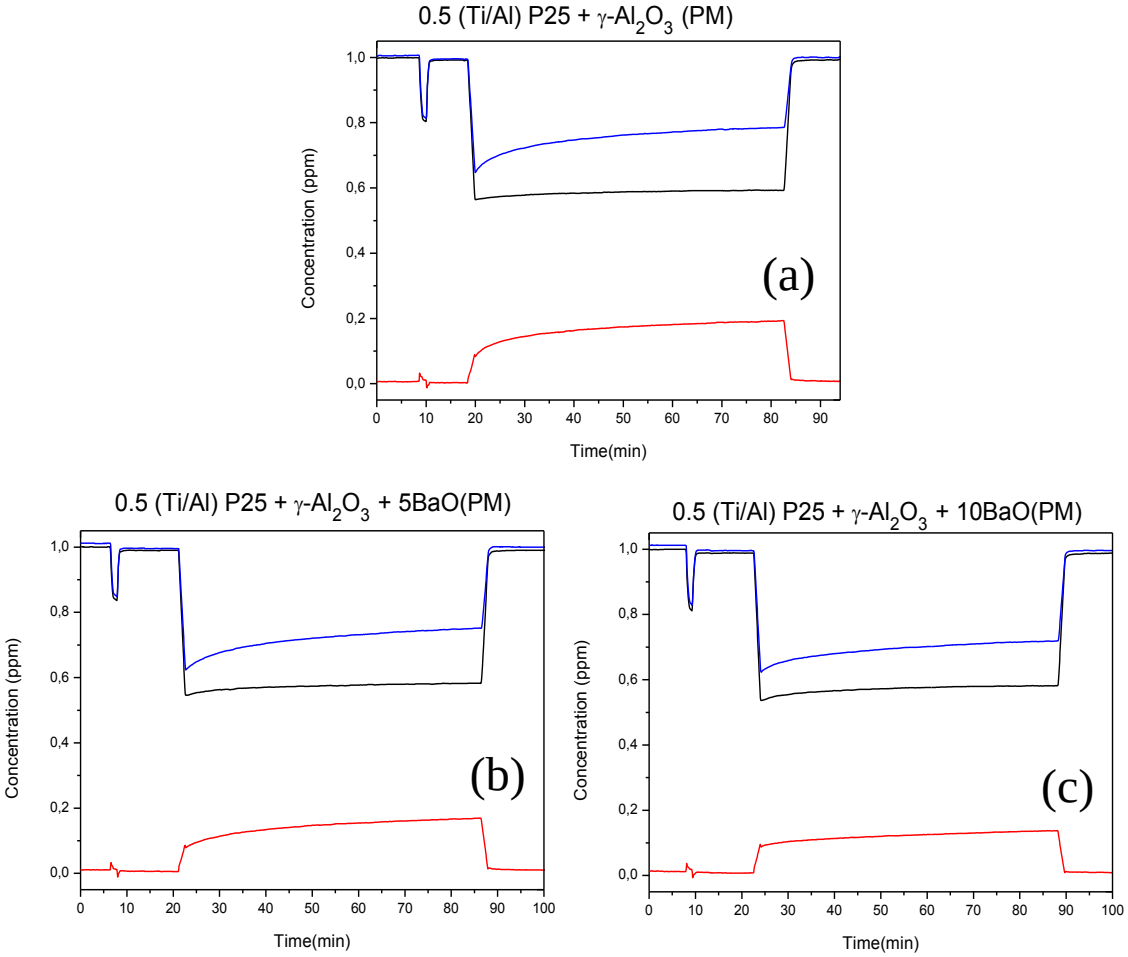

Figure 67. Performance plots of Degussa P25 TiO2, γ-Al_2O_3 and BaO physical mixtures in the following compositions (a) 0.5-P25: γ-Al_2O_3 mole ratio, (b) 0.5-P25: γ-Al_2O_3 + 5% (w/w) BaO, (c) 0.5-P25: γ-Al_2O_3 + 10% (w/w) BaO

Similar physical mixtures have also been prepared using P25 directly, and as can be seen in Figure 67a and Figure 68, mixing P25 with alumina in 0.5 TiO_2:Al_2O_3 mole ratio increased its NO_x abatement capacity immensely (4.6 times higher than P25) by reducing the amount of emitted $NO_{2(g)}$. The addition of 5% (w/w) alkaline earth metal oxide (BaO) storage component continued to increase the NO_x abatement by further decreasing released $NO_{2(g)}$ levels and finally mixing 10% (w/w) BaO with 0.5 P25-Al_2O_3 resulted in the most successful NO_x abatement catalyst among all tested candidates.

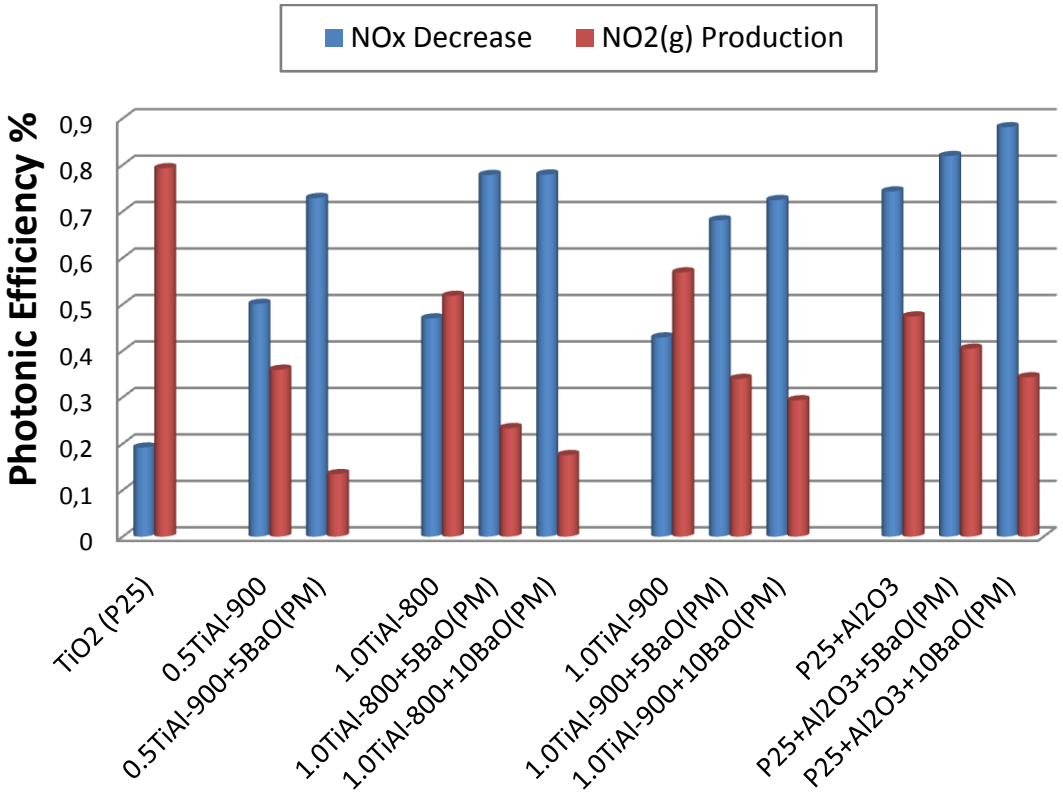

Figure 68. The photonic efficiencies for total NO_x abatement and $NO_{2(g)}$ production in physically mixed Ti/Al/BaO samples, compared with the efficiencies of Degussa P25, 0.5 Ti/Al-900, 1.0 Ti/Al-800 and 1.0 Ti/Al-900.

However as can be observed in Figure 68, P25 based photocatalytic mixtures still produce unfavorably more $NO_{2(g)}$ compared to sol-gel Ti/Al based mixtures. Thus in order to have a more balanced view on the general effectiveness of the photocatalysts, the ratio of total NO_x abatement efficiency to gaseous $NO_{2(g)}$ production efficiency have been calculated and displayed in Figure 69. By comparing the NO_x storage : $NO_{2(g)}$ production efficiency ratios of these samples, it is observed that 0.5 Ti/Al-900+5Ba(PM) is the most useful photocatalyst, better than all the others, and in general Ti/Al (sol-gel) based-mixtures have a higher affinity towards nitrate deposition than P25 based mixtures and all in all, BaO added samples in general work several times better than their non-BaO mixed counterparts.

Also in these physically mixed samples, the incorporation of 10% (w/w) storage component (BaO) decreases $NO_{2(g)}$ emission more effectively than 5%(w/w) addition and increases the total NO_x abatement efficiency. It can be argued that in the physical mixing route, the added BaO domains do not cover and bury the photocatalytically active TiO_2 domains, thus the increase of the storage component loading helps enhancing the absorbtion of $NO_{2(g)}$ in solid phase. Comparing with "the wetness impregnation" method, these physical mixtures display an opposite behavior because in the impregnation method, increasing the metal nitrate loading from 5% to 10% (w/w) had detoriated the NO_x abatement by causing more metal titanates to form, consume and bury the TiO_2 domains and as a result, the oxidative power of the photocatalyst was attenuated.

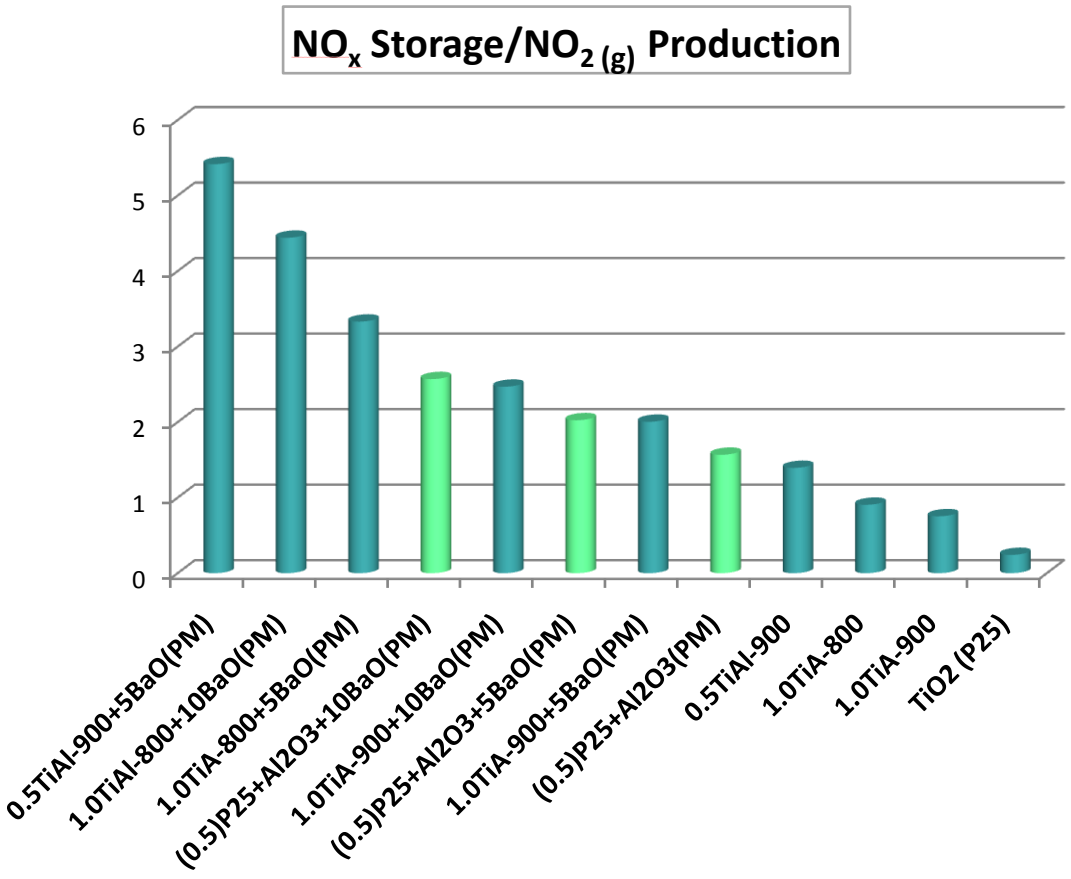

Figure 69. The ratio of NOx abatement (storage) and $NO_{2(g)}$ production photonic efficiencies for physically mixtured samples, compared with Degussa P25, 0.5 Ti/Al-900, 1.0 Ti/Al-800 and 1.0 Ti/Al-900. Dark green bars represent Ti/Al (sol-gel) based mixtures and light green bars identify P25-based mixtures.

3.4 Photonic Efficiencies of the PhoNOS Catalysts in Comparison to Literature Data

Photonic efficiencies of the sol-gel Ti/Al binary oxides and Ti/Al+M_xO ternary oxides in NO_x storage and $NO_{2(g)}$ production have been evaluated with the following formula:

$$\zeta\% = \frac{n \text{ (stored } NO_x \text{ or produced } NO_2)}{n \text{ (available photons)}} \text{x}100 = \frac{\Delta n \dot{N}O_x \text{ (or } \Delta n \dot{N}O_2)}{\phi x \Delta T} \text{x}100$$

The number available photons is the number of moles of incident photons on the catalyst surface during the reaction and it is related to the photon flux of the lamp (ϕ), which can be determined according to:

$$\phi = \frac{I'' \lambda S}{N h c}$$

Here, I'' is the photon power density for the UV lamp (~5 W/m^2), λ is the representative emission wavelength of the UV lamp (i.e. 350 nm), S is UV illuminated area (i.e. 16 cm^2); N is Avagadro's number, h is Planck's constant and c is the speed of light.

By inserting the photon flux formula into the photonic efficiency formula, ζ% can be defined as:

$$\zeta\% = \frac{Nhc \text{ x } \Delta n \dot{N}O_x \text{ (or } \Delta n \dot{N}O_2)}{I'' \lambda S x \Delta T} \text{x}100$$

Examining this equation shows that the photonic efficiency of $NO_{x(g)}$ abatement depends significantly on the reaction conditions, and when one varies the initial $NO_{(g)}$ concentration (thus $\Delta n \dot{N}O_x$ or $\Delta n \dot{N}O_2$) , photon power density of the lamp (I'') or the total geometric area of UV- irradiation (S), one can change the maximum photonic efficiency of the reaction.

For instance, in our case, the total amount of NO that is sent to the reactor is $2.45x10^{-6}$ mol/h, and this number is calculated for 1 ppm $NO_{(g)}$ in 1 L/min N_2+O_2 mixture. If a photocatalyst is able to completely oxidize and consequently store the initial 1 ppm NO in the first hour (100% oxidation to $NO_3^-{}_{(s)}$), then $\Delta n\ NO_x$ would be $2.45x10^{-6}$ mol, which gives a maximum theoretical photonic efficiency 2.91 % for NO_x storage. Note that this percentage is not only depending on the inherent oxidation/storage capacity of the photocatalyst (i.e. TiO_2 crystalline phase, storage component loading etc.) but is also closely related to the photon flux of the lamp ($8.4x10^{-5}$ einstein/h = $0.23x10^{-5}$ einstein/s), the flow rate (1L/min) and the area of the photocatalyst that is exposed to the UV light (16 cm^2).

Bannat et al. [108] have explained that the maximum theoretical photonic efficiency of NO degredation is 0.45% for 0.1 ppm NO in 3 L/min air under 10W/m^2 UV light, on a TiO_2 film whose geometric area is 15.5 cm^2. Similarly, Kalousek et al. [109] stated that the maximum theoretical photonic efficiency of NO degredation is 0.14% for 0.1 ppm NO in 3 L/min air under 10W/m^2 UV light, on a TiO_2 film whose geometric area is 20 cm^2. These examples prove that a direct comparison of the photonic efficiencies in different experimental conditions is not plausible, and unless the photonic efficiencies are determined in the same photocatalytic system, a photonic efficiency of 1% may not mean a better PhoNOS catalyst than a photonic efficiency of 0.5%.

In addition, since the photocatalytic NO_x abatement field is generally focused on NO oxidation while the storage of the oxidized NO in the solid state is usually overlooked, some articles just present photonic efficiencies for NO oxidation (or degredation) and ignore the amount of $NO_{2(g)}$ that is released into the atmosphere. However, comparing NO oxidation efficiencies is ineffective in understanding the total NO_x abatement in each system. This statement is especially true when evaluating the activity of PhoNOS catalysts (presented in this thesis) with respect to pure titania samples, because pure titania is a powerful oxidant and although NO oxidation efficiency of such a sample may be higher than that of a PhoNOS catalyst, the total NO_x abatement efficiency may prove to be much poorer. When $NO_{2(g)}$ production efficiency of a photocatalyst is not presented in an article, comparing NO oxidation efficiencies alone would not be conclusive. It is important evaluate NO

oxidation (degredation), $NO_{2(g)}$ production and total NO_x abatement seperately. One should be very careful when comparing photonic efficiencies of total NO_x abatement (and $NO_{2(g)}$ production) in variant conditions.

In order to be able to compare different photocatalysts, Bannat et al.[108] defined photocatalytic activity as the ratio of measured photonic efficiency ζ (for NO degredation) to theoretical photonic efficiency ζ_{th}. In their study, the authors prepared pure mesoporous TiO_2 films on glass substrates and on ITO-coated glass substrates. Their results have shown that the activity on glass substrate is 9% (ζ= 0.0405%) of the theoretical photonic efficiency (ζ_{th} = 0.45%) whereas on ITO-coated glass, the activity increases to 14% (ζ= 0.063%) of the theoretical value. Next, the authors loaded TiO_2 with Au nanoparticles smaller than 5 nm in size via impregnation method and claimed that this increased the activity to 26% (ζ= 0.117%) of the theoretical value for films on glass slides and to 40% (ζ= 0.18%) for films on ITO-coated glass. These NO oxidation efficiencies are much lower than that of our best PhoNOS catalysts; 0.5 Ti/Al-900+5BaO (PM) (ζ_{NO} = 0.86%), 1.0 Ti/Al-800+5BaO (PM) (ζ_{NO} = 0.99%) , 1.0 Ti/Al-800+10BaO (PM) (ζ_{NO} = 0.94%), although as stated above, it is difficult to compare catalysts under different conditions (contaminant concentration, flow rate, photon flux, etc.) and catalysts with different physical structures (powder vs. film). Also, the authors do not mention how much $NO_{2(g)}$ is produced by each sample and how much total NO_x abatement is achieved in each case, so evaluation on NO oxidation(degredation) efficiency alone is not plausible.

A more closely related study has been performed by Giannakopoulou et al.[110] very recently and in that study the authors prepared powder TiO_2 samples mixed with HA (calcium phosphate tribasic, 34–40% Ca, Alfa Aesar) powder in different HA/TiO_2 weight ratios (between 0.25 and 4, designated as HT-0.25, HT-0.5, HT-1, HT-2, and HT-4), and these powders were stirred together in 30 ml distilled water for 2 h at ambient conditions. Their best photocatalyst turned out to be HT-2 composite and that sample had a total NO_x abatement efficiency of ~0.77% and a $NO_{2(g)}$ production efficiency of ~0.23%. With respect to to our most effective catalysts, 0.5 Ti/Al-900+5BaO (PM) (ζ_{NO_x}= 0.73% $\zeta_{NO_{2(g)}}$= 0.13%), 1.0 Ti/Al-

800+5BaO (PM) (ζ NO_x= 0.78% ζ $NO_{2(g)}$= 0.21%) and 1.0 Ti/Al-800+10BaO (PM) (ζ NO_x= 0.78% ζ $NO_{2(g)}$= 0.16%), the results of Giannakopoulou et al. is comparable, yet their best catalyst seems to be producing sligtly more $NO_{2(g)}$. Also note that, there is again a difference between two systems in terms of experimental conditions, since in that study the authors use a total flow rate of 3.0 L, 10 W/m^2 photon flux and a sample holder with 25 cm^2 geometrical area.

All in all, the theoretical maximum photonic efficiency does not have a constant value and changes in each experimental set-up with respect to the initial reaction conditions. Therefore a direct comparison of the numerical efficiecies is not a conclusive method to choose the most effective PhoNOS catalyst. Calculating the ratio of measured photonic efficiency ζ to theoretical photonic efficiency ζ_{th}, (ζ/ζ_{th}) may prove to be a better method to evaluate the activities PhoNOS catalysts in different experimental conditions, though this comparison may still not be completely accurate. It is much more convenient to compare each candidate catalyst with a benchmark sample (such as Degussa P25®) that have been tested under the same conditions.

4. CONCLUSIONS

In this thesis, a hybrid technology for the photocatalytic oxidation and storage of gas phase NO_x species was proposed and photocatalytically activated NO_x oxidation and storage materials were obtained by combining photocatalytically activated NO_x oxidation catalyst TiO_2 with the NO_x storage components of thermally activated NO_x Storage/Reduction (NSR) system. In this regard, three different set of samples were prepared, characterized and tested:

A) TiO_2/Al_2O_3 binary oxides were synthesized by "sol-gel co-precipitation" method in three different Ti:Al mole ratios: **(i)** 0.25 **(ii)** 0.5 and **(iii)** 1.0. These samples were calcined in air for 2 hours, at different temperatures between 150-1000^oC and characterized by X-ray diffraction (XRD), Raman Spectroscopy and BET.

For these binary oxides, the effects of specific surface area, calcination temperature, the crystallinity of TiO_2 and Ti:Al mole ratio of the sample were investigated in NO_x oxidation/storage reaction.

B) $M_yO/TiO_2/Al_2O_3$ ternary oxides were prepared by "incipient wetness impregnation" of 5 or 10% (w/w) metal nitrate [$M(NO_3)_x$] salts on TiO_2-Al_2O_3 binary oxides (0.5 Ti/Al-900, 1.0 Ti/Al-800, 1.0 Ti/Al-900) and subsequently calcined to obtain alkali/alkaline earth oxides [M_yO].

C) $BaO/TiO_2/Al_2O_3$ ternary oxides were prepared by physically grinding 5 or 10% (w/w) BaO powder with;

- **i.** sol-gel TiO_2-Al_2O_3 binary oxides (0.5 Ti/Al-900, 1.0 Ti/Al-800, 1.0 Ti/Al-900)
- **ii.** Degussa P25+γ-Al_2O_3 physical mixture (Ti:Al mole ratio =0.5)

For these ternary oxides, the effects of metal oxide incorporation route (impregnation vs. physical mixture), the type of the metal oxide storage component (alkali vs. alkaline earth metal) and the percentage of alkali/alkaline metal oxide loading (5% vs. 10%, w/w) were examined in NO_x oxidation and storage reaction.

A continuous flow system, composed of mass flow controllers, a custom-made UVA-illuminated reaction cell and an ambient chemiluminescence NO_x analyzer has been assembled for the photocatalytic performance tests of these photocatalysts. 1 ppmv $NO_{(g)}$ in 1.0 SLM (standard litre/minute) of $N_{2(g)}$+$O_{2(g)}$ mixture was run over the catalyst in the flow reactor, which was irradiated with a UVA lamp (with a photon power density of approximately 5 W/m^2). For each sample, the photonic efficiency of total NO_x abatement (storage) and of $NO_{2(g)}$ production (emission) were calculated and these photonic efficiencies were evaluated against those of Degussa P25, the benchmark sample.

After sample characterization, the addition of Al_2O_3 was observed to be impeding the crystallization of TiO_2 in TiO_2/Al_2O_3 binary oxides and the crystallization temperature of titania increased from 350^{o}C (in pure TiO_2) to 800^{o}C in 1.0 Ti/Al, to 900^{o}C in 0.5 Ti/Al and to 950^{o}C in 0.25 Ti/Al. Furthermore, the photocatalytic activity tests showed that the photooxidation abilities of TiO_2-Al_2O_3 binary oxides were directed by their crystalline structure and while amorphous samples (that were calcined at lower temperatures) showed no photoreactivity, crystalline TiO_2-Al_2O_3 samples oxidized $NO_{(g)}$ and had much higher NO_x abatement (storage) efficiencies compared to Degussa P25. Especially, the samples that were calcined at a temperature where TiO_2 crystallization just initiated showed the best NO_x storage performances, possibly as a result of smaller TiO_2 crystallite sizes and relatively larger surface areas. In addition, 0.5 Ti/Al-900 sample was observed to have the most effective NO_x storage among all TiO_2-Al_2O_3 binary oxides and thus 0.5 proved to be an optimum mole ratio of Ti:Al, in terms of enhancing the total NO_x storage and preventing gaseous NO_2 release into the atmosphere.

Further addition of an alkali/alkaline earth oxide NO_x storage component on TiO_2-Al_2O_3 binary oxides had different effects, based on the incorporation method. The “incipient wetness impregnation” of metal nitrates resulted in metal titanate ($M_xTi_yO_z$) formation on TiO_2-Al_2O_3 binary oxides and diminished the photooxidation ability of the catalyst. In terms of metal oxide loading, higher mass fraction, 10% (w/w), perforrmed much worse in NO_x abatement than 5%(w/w) loading since it caused a higher amount of metal titanate to form, which probably consumed and buried the TiO_2 domains and as a result, the oxidative power of the

photocatalyst was attenuated. Finally, among this set of samples, alkaline earth metal group performed slightly better than the alkali metal group, possibly as a result of easier nitrate formation on Group IIA metals.

On the other hand, adding BaO storage sites on TiO_2-Al_2O_3 by physical mixing significantly enhanced the NO_x capture in solid state and decreased gaseous NO_2 emission to an almost negligible level. Among the physically mixed photocatalysts, *sol-gel* Ti/Al binary oxide+BaO mixtures proved to be more effective in diminishing $NO_{2(g)}$ production and increasing NO_x storage compared to Degussa P25+γ-Al_2O_3+BaO ternary mixtures. In terms of BaO loading, 10%(w/w) addition worked better than 5% (w/w) addition of the NO_x storage component, contrary to what was observed in the impregnated samples.

Ultimately, the photocatalytic NO_x oxidation and storage (PhoNOS) catalysts proposed in this study was shown to display higher NO_x abatement efficiencies with respect to the gold standard Degussa P25, and specifically, the physically mixed ternary oxide samples stand out in terms of NO_x storage efficiencies. 0.5 Ti/Al-900+5BaO is the most efficient catalyst, storing four times more NO_x per hour and releasing less than one-fifth of $NO_{2(g)}$ compared to Degussa P25. As a future work, the reactions taking place on the surface of these materials can be explored via FT-IR spectroscopy and also the TiO_2 domains can be enriched with various intra-band gap dopants to enable absorption of sub-band gap (low energy) visible light.

5. REFERENCES

1. www.learner.org, *Atmospheric Pollution*, in *The Habitable Planet, a systems approach to environmental science*.

2. http://www.epa.gov/airquality/sulfurdioxide/.

3. http://www.epa.gov/airquality/nitrogenoxides/.

4. http://www.epa.gov/airquality/carbonmonoxide/.

5. http://www.epa.gov/pm/basic.html.

6. http://www.osha.gov/SLTC/metalsheavy/index.html.

7. http://www.nc-climate.ncsu.edu/edu/k12/.ozonelayer.

8. http://www.epa.gov/air/ozonepollution/health.html.

9. http://www.epa.gov/air/caa/.

10. http://www.saglikbakanligi.com/html_files/bilgi/CEVRE_VE_SAGLIK/CVS-5.htm.

11. Atkinson, R., *Atmospheric chemistry of VOCs and NO_x.* Atmospheric Environment, 2000. **34**(12–14): p. 2063-2101.

12. ATSDR. *ToxFAQs for Nitrogen Oxides*. Available from: http://www.atsdr.cdc.gov/toxfaqs/tf.asp?id=396&tid=69.

13. Peterson, J.S. *Nitrous Dioxide Toxicity, (Pathophysiology)* Available from: http://emedicine.medscape.com/article/820431-overview#a0104.

14. Skalska, K., J.S. Miller, and S. Ledakowicz, *Trends in NO_x abatement: A review.* Science of The Total Environment, 2010. **408**(19): p. 3976-3989.

15. Klingstedt, F., et al., *Toward Improved Catalytic Low-Temperature NO_x Removal in Diesel-Powered Vehicles.* Accounts of Chemical Research, 2006. **39**(4): p. 273-282.

16. Haagen-Smit, A.J., *Chemistry and Physiology of Los Angeles Smog.* Industrial & Engineering Chemistry, 1952. **44**(6): p. 1342-1346.

17. Muzio, L.J. and G.C. Quartucy, *Implementing NO_x control: Research to application.* Progress in Energy and Combustion Science, 1997. **23**(3): p. 233-266.

18. Granger, P. and V.I. Parvulescu, *Catalytic NO_x Abatement Systems for Mobile Sources: From Three-Way to Lean Burn after-Treatment Technologies.* Chemical Reviews, 2011. **111**(5): p. 3155-3207.

19. http://www.aecc.be/en/Publications/Publications.html.

20. http://openlearn.open.ac.uk.

21. Matsumoto, S.i., *Catalytic Reduction of Nitrogen Oxides in Automotive Exhaust Containing Excess Oxygen by NO_x Storage-Reduction Catalyst.* CATTECH, 2000. **4**(2): p. 102-109.

22. *Air Quality Index, A Guide to Air Quality and Your Health*. 2009; Available from: http://www.epa.gov/airnow/aqi_brochure_08-09.pdf.

23. Smadi, B.M.A., K.K. Al-Zboon, and K.M. Shatnawi, *Assessment of Air Pollutants Emissions from a Cement Plant: A Case Study in Jordan.* Jordan Journal of Civil Engineering, 2009. **3**: p. 265-282.

24. Fujishima, A. and K. Honda, *Electrochemical Photolysis of Water at a Semiconductor Electrode.* Nature, 1972. **238**(5358): p. 37-38.

25. Henderson, M.A., *A surface science perspective on TiO_2 photocatalysis.* Surface Science Reports, 2011. **66**(6-7): p. 185-297.

26. Hanaor, D.A.H. and C.C. Sorrell, *Review of the anatase to rutile phase transformation.* Journal of Materials Science, 2011. **46**(4): p. 855-874.

27. Addamo, M., et al., *Preparation and photoactivity of nanostructured anatase, rutile and brookite TiO_2 thin films.* Chemical Communications, 2006(47): p. 4943-4945.

28. Štengl, V. and D. Králová, *Photoactivity of brookite–rutile TiO_2 nanocrystalline mixtures obtained by heat treatment of hydrothermally prepared brookite.* Materials Chemistry and Physics, 2011. **129**(3): p. 794-801.

29. Di Paola, A., et al., *Preparation of photocatalytic brookite thin films.* Thin Solid Films, 2007. **515**(7-8): p. 3527-3529.

30. Carp, O., C.L. Huisman, and A. Reller, *Photoinduced reactivity of titanium dioxide.* Progress in Solid State Chemistry, 2004. **32**(1–2): p. 33-177.

31. Burdett, J.K., et al., *Structural-electronic relationships in inorganic solids: powder neutron diffraction studies of the rutile and anatase polymorphs of titanium dioxide at 15 and 295 K.* Journal of the American Chemical Society, 1987. **109**(12): p. 3639-3646.

32. Matthews, A., *The crystallization of anatase and rutile from amorphous titanium dioxide under hydrothermal conditions.* Am Miner 1976. **61**(419).

33. Penn, R. and J. Banfield, *Formation of rutile nuclei at anatase {112} twin interfaces and the phase transformation mechanism in nanocrystalline titania.* Am Miner 1999. **84**: p. 871.

34. Hyoung, G. and J. Zuo, *Growth and Phase Transformation of Nanometer-Sized Titanium Oxide Powders Produced by the Precipitation Method* J Am Ceram Soc 2004. **87**: p. 473.

35. Shannon, R.D. and J.A. Pask, *Kinetics of the Anatase-Rutile Transformation.* Journal of the American Ceramic Society, 1965. **48**(8): p. 391-398.

36. Criado, J. and C. Real, *Mechanism of the inhibiting effect of phosphate on the anatase-rutile transformation induced by thermal and mechanical treatment*

of TiO2. Journal of the Chemical Society, Faraday Transactions 1: Physical Chemistry in Condensed Phases, 1983. **79**(12): p. 2765-2771.

37. Hirano, M., et al., *Photoactivity and phase stability of ZrO_2-doped anatase-type TiO_2 directly formed as nanometer-sized particles by hydrolysis under hydrothermal conditions.* Journal of Solid State Chemistry, 2003. **170**(1): p. 39-47.

38. Zhang, H. and J. Banfield, *Phase transformation of nanocrystalline anatase-to-rutile via combined interface and surface nucleation.* Journal of Materials Research, 2000. **15**: p. 437.

39. Reidy, D.J., J.D. Holmes, and M.A. Morris, *The critical size mechanism for the anatase to rutile transformation in TiO_2 and doped-TiO_2.* Journal of the European Ceramic Society, 2006. **26**(9): p. 1527-1534.

40. Yu, J.C., et al., *Effects of F- Doping on the Photocatalytic Activity and Microstructures of Nanocrystalline TiO_2 Powders.* Chemistry of Materials, 2002. **14**(9): p. 3808-3816.

41. Ihara, T., et al., *Visible-light-active titanium oxide photocatalyst realized by an oxygen-deficient structure and by nitrogen doping.* Applied Catalysis B: Environmental, 2003. **42**(4): p. 403-409.

42. Lim, M., et al., *Development and potential of new generation photocatalytic systems for air pollution abatement: an overview.* Asia-Pacific Journal of Chemical Engineering, 2009. **4**(4): p. 387-402.

43. Asahi, R., et al., *Electronic and optical properties of anatase TiO_2.* Physical Review B, 2000. **61**(11): p. 7459-7465.

44. Chen, X. and S.S. Mao, *Titanium Dioxide Nanomaterials: Synthesis, Properties, Modifications, and Applications.* Chemical Reviews, 2007. **107**(7): p. 2891-2959.

45. Wang, H. and J.P. Lewis, *Second-generation photocatalytic materials: anion-doped TiO2.* Journal of Physics-Condensed Matter, 2006. **18**(2): p. 421-434.

46. Linsebigler, A.L., G.Q. Lu, and J.T. Yates, *Photocatalysis on TiO_2 Surfaces-Principles, Mechanisms, and Selected Results.* Chemical Reviews, 1995. **95**(3): p. 735-758.

47. Diebold, U., *The surface science of titanium dioxide.* Surface Science Reports, 2003. **48**(5–8): p. 53-229.

48. Kavan, L., et al., *Electrochemical and Photoelectrochemical Investigation of Single-Crystal Anatase.* Journal of the American Chemical Society, 1996. **118**(28): p. 6716-6723.

49. Fujihara, K., T. Ohno, and M. Matsumura, *Splitting of water by electrochemical combination of two photocatalytic reactions on TiO_2 particles.* Journal of the Chemical Society, Faraday Transactions, 1998. **94**(24): p. 3705-3709.

50. Ni, M., et al., *A review and recent developments in photocatalytic water-splitting using for hydrogen production.* Renewable and Sustainable Energy Reviews, 2007. **11**(3): p. 401-425.

51. Huang, S.Y., et al., *Charge Recombination in Dye-Sensitized Nanocrystalline TiO_2 Solar Cells.* The Journal of Physical Chemistry B, 1997. **101**(14): p. 2576-2582.

52. O'Regan, B. and M. Gratzel, *A low-cost, high-efficiency solar cell based on dye-sensitized colloidal TiO_2 films.* Nature, 1991. **353**(6346): p. 737-740.

53. Paz, Y., *Application of TiO_2 photocatalysis for air treatment: Patents' overview.* Applied Catalysis B-Environmental, 2010. **99**(3-4): p. 448-460.

54. Matthews, R.W., *Photooxidation of organic impurities in water using thin films of titanium dioxide.* The Journal of Physical Chemistry, 1987. **91**(12): p. 3328-3333.

55. Baram, N., et al., *Enhanced photo-efficiency of immobilized TiO_2 catalyst via intense anodic bias.* Electrochemistry Communications, 2007. **9**(7): p. 1684-1688.

56. Pozzo, R.L., M.A. Baltanás, and A.E. Cassano, *Supported titanium oxide as photocatalyst in water decontamination: State of the art.* Catalysis Today, 1997. **39**(3): p. 219-231.

57. Okamoto, K.-i., et al., *Heterogeneous Photocatalytic Decomposition of Phenol over TiO_2 Powder.* Bulletin of the Chemical Society of Japan, 1985. **58**(7): p. 2015-2022.

58. Bondioli, F., R. Taurino, and A.M. Ferrari, *Functionalization of ceramic tile surface by sol-gel technique.* Journal of Colloid and Interface Science, 2009. **334**(2): p. 195-201.

59. Mills, A., et al., *Characterisation of the photocatalyst Pilkington Activ™: a reference film photocatalyst?* Journal of Photochemistry and Photobiology A: Chemistry, 2003. **160**(3): p. 213-224.

60. Mitoraj, D., et al., *Visible light inactivation of bacteria and fungi by modified titanium dioxide.* Photochemical & Photobiological Sciences, 2007. **6**(6): p. 642-648.

61. Kisch, H., G. Burgeth, and W. Macyk, *Visible Light Photocatalysis by a Titania Transition Metal Complex*, in *Advances in Inorganic Chemistry*, R.v. Eldik, Editor. 2004, Academic Press. p. 241-259.

62. Tanaka, K., M.F.V. Capule, and T. Hisanaga, *Effect of crystallinity of TiO_2 on its photocatalytic action.* Chemical Physics Letters, 1991. **187**(1–2): p. 73-76.

63. Gerischer, H. and A. Heller, *Photocatalytic Oxidation of Organic Molecules at TiO_2 Particles by Sunlight in Aerated Water.* Journal of The Electrochemical Society, 1992. **139**(1): p. 113-118.

64. Bickley, R.I., et al., *A structural investigation of titanium dioxide photocatalysts.* Journal of Solid State Chemistry, 1991. **92**(1): p. 178-190.

65. Muggli, D.S. and L. Ding, *Photocatalytic performance of sulfated TiO2 and Degussa P-25 TiO_2 during oxidation of organics.* Applied Catalysis B: Environmental, 2001. **32**(3): p. 181-194.

66. Ohno, T., et al., *Morphology of a TiO_2 Photocatalyst (Degussa, P-25) Consisting of Anatase and Rutile Crystalline Phases.* Journal of Catalysis, 2001. **203**(1): p. 82-86.

67. Devahasdin, S., et al., *TiO_2 photocatalytic oxidation of nitric oxide: transient behavior and reaction kinetics.* Journal of Photochemistry and Photobiology A: Chemistry, 2003. **156**(1–3): p. 161-170.

68. Fujishima, A. and X. Zhang, *Titanium dioxide photocatalysis: present situation and future approaches.* Comptes Rendus Chimie, 2006. **9**(5–6): p. 750-760.

69. İnel, Y. and A.N. Ökte, *Photocatalytic degradation of malonic acid in aqueous suspensions of titanium dioxide: an initial kinetic investigation of CO2 photogeneration.* Journal of Photochemistry and Photobiology A: Chemistry, 1996. **96**(1–3): p. 175-180.

70. Assabane, A., et al., *Photocatalytic degradation of polycarboxylic benzoic acids in UV-irradiated aqueous suspensions of titania.: Identification of intermediates and reaction pathway of the photomineralization of trimellitic acid (1,2,4-benzene tricarboxylic acid).* Applied Catalysis B: Environmental, 2000. **24**(2): p. 71-87.

71. Fox, M.A. and M.T. Dulay, *Heterogeneous photocatalysis.* Chemical Reviews, 1993. **93**(1): p. 341-357.

72. Herrmann, J.-M., *Heterogeneous photocatalysis: fundamentals and applications to the removal of various types of aqueous pollutants.* Catalysis Today, 1999. **53**(1): p. 115-129.

73. Kiwi, J., *Direct observation of the variation of energy levels in powdered titanium dioxide as a function of temperature. Beneficial effects for energy conversion through semiconductor devices.* The Journal of Physical Chemistry, 1985. **89**(12): p. 2437-2439.

74. Ollis, D.F., E. Pelizzetti, and N. Serpone, *Photocatalyzed destruction of water contaminants.* Environmental Science & Technology, 1991. **25**(9): p. 1522-1529.

75. Jacoby, W.A., et al., *Kinetics of the Oxidation of Trichloroethylene in Air via Heterogeneous Photocatalysis.* Journal of Catalysis, 1995. **157**(1): p. 87-96.

76. Wang, Y.-P., et al., *Studies on the Interaction of DNA and a Novel of Water-soluble Polymer-bound Schiff Base Complex.* Chemistry Letters, 1998. **27**(3): p. 271-272.

77. Braun, A.M. and E. Oliveros, *How to evaluate photochemical methods for water treatment.* Water Science and Technology, 1997. **35**(4): p. 17-23.

78. Wu, J.C.S. and Y.-T. Cheng, *In situ FTIR study of photocatalytic NO reaction on photocatalysts under UV irradiation.* Journal of Catalysis, 2006. **237**(2): p. 393-404.

79. Komazaki, Y., H. Shimizu, and S. Tanaka, *A new measurement method for nitrogen oxides in the air using an annular diffusion scrubber coated with titanium dioxide.* Atmospheric Environment, 1999. **33**(27): p. 4363-4371.

80. Matsuda, S., H. Hatano, and A. Tsutsumi, *Ultrafine particle fluidization and its application to photocatalytic NO_x treatment.* Chemical Engineering Journal, 2001. **82**(1–3): p. 183-188.

81. Yu, Q.L. and H.J.H. Brouwers, *Indoor air purification using heterogeneous photocatalytic oxidation. Part I: Experimental study.* Applied Catalysis B-Environmental, 2009. **92**(3-4): p. 454-461.

82. Dalton, J.S., et al., *Photocatalytic oxidation of NO_x gases using TiO_2: a surface spectroscopic approach.* Environmental Pollution, 2002. **120**(2): p. 415-422.

83. Anpo, M., *Applications of titanium oxide photocatalysts and unique second-generation TiO_2 photocatalysts able to operate under visible light irradiation for the reduction of environmental toxins on a global scale,* in *Studies in*

Surface Science and Catalysis, F.V.M.S.M. Avelino Corma and G.F. José Luis, Editors. 2000, Elsevier. p. 157-166.

84. http://www.mmc.co.jp/corporate/en/product/construct/10.html.

85. Frazer, L., *Titanium Dioxide: Environmental White Knight?* , in *Environmental Health Perspectives* 2001. p. A 174–177.

86. http://www.italcementigroup.com/ENG/Research+and+Innovation/Innovative+Products/TX+Active/TX+Active.htm.

87. http://www.italcementigroup.com/NR/rdonlyres/1F30E487-C0A2-4D6F-AB6D-C14555FD866F/0/Scientificresults.pdf.

88. ISO22197-1Standard: http://www.iso.org/iso/home/store/catalogue_tc/catalogue_detail.htm?csnumber=40761.

89. Hashimoto, K., et al., *Photocatalytic oxidation of nitrogen oxide over titania–zeolite composite catalyst to remove nitrogen oxides in the atmosphere.* Applied Catalysis B: Environmental, 2001. **30**(3–4): p. 429-436.

90. Andonova, S.M., G.S. Senturk, and E. Ozensoy, *Fine-Tuning the Dispersion and the Mobility of BaO Domains on NO_x Storage Materials via TiO_2 Anchoring Sites.* Journal of Physical Chemistry C, 2010. **114**(40): p. 17003-17016.

91. http://www.matbase.com/material/polymers/commodity/pmma/properties.

92. Ezrin, M., *Plastics Failure Guide: Cause and Prevention*. 1996, Ohio: Hanser/Gardner Publications Inc. 473.

93. *HORIBA APNA 370 User Manual*.

94. Mitsionis, A., et al., *Hydroxyapatite/titanium dioxide nanocomposites for controlled photocatalytic NO oxidation.* Applied Catalysis B-Environmental, 2011. **106**(3-4): p. 398-404.

95. Spurr, R.A. and H. Myers, *Quantitative Analysis of Anatase-Rutile Mixtures with an X-Ray Diffractometer.* Analytical Chemistry, 1957. **29**(5): p. 760-762.

96. Li, G., et al., *Synergistic effect between anatase and rutile TiO_2 nanoparticles in dye-sensitized solar cells.* Dalton Transactions, 2009(45): p. 10078-10085.

97. Sakthivel, S., et al., *Solar photocatalytic degradation of azo dye: comparison of photocatalytic efficiency of ZnO and TiO_2.* Solar Energy Materials and Solar Cells, 2003. **77**(1): p. 65-82.

98. Bickmore, C.R., et al., *Ultrafine titania by flame spray pyrolysis of a titanatrane complex.* Journal of the European Ceramic Society, 1998. **18**(4): p. 287-297.

99. Ohno, T., K. Sarukawa, and M. Matsumura, *Photocatalytic Activities of Pure Rutile Particles Isolated from TiO_2 Powder by Dissolving the Anatase Component in HF Solution.* The Journal of Physical Chemistry B, 2001. **105**(12): p. 2417-2420.

100. Szczepankiewicz, S.H., A.J. Colussi, and M.R. Hoffmann, *Infrared Spectra of Photoinduced Species on Hydroxylated Titania Surfaces.* The Journal of Physical Chemistry B, 2000. **104**(42): p. 9842-9850.

101. Andonova, S.M., et al., *Nature of the Ti−Ba Interactions on the $BaO/TiO_2/Al_2O_3$ NO_x Storage System.* The Journal of Physical Chemistry C, 2009. **113**(25): p. 11014-11026.

102. Wang, Z. and X. Deng, *Al2O3 composite agent effects on phase transformation of nanometer TiO_2 powder*. Materials Science and Engineering: B, 2007. **140**(1–2): p. 109-113.

103. Ohsaka, T., F. Izumi, and Y. Fujiki, *Raman spectrum of anatase, TiO_2.* Journal of Raman Spectroscopy, 1978. **7**(6): p. 321-324.

104. Ma, H.L., et al., *Raman study of phase transformation of TiO2 rutile single crystal irradiated by infrared femtosecond laser.* Applied Surface Science, 2007. **253**(18): p. 7497-7500.

105. Raj, K.J.A. and B. Viswanathan, *Effect of surface area, pore volume and particle size of P25 titania on the phase transformation of anatase to rutile.* Indian Journal of Chemistry Section a-Inorganic Bio-Inorganic Physical Theoretical & Analytical Chemistry, 2009. **48**(10): p. 1378-1382.

106. Thamaphat, K., P. Limsuwan, and B. Ngotawornchai, *Phase Characterization of TiO_2 Powder by XRD and TEM.* Nat Sci, 2008. **42**: p. 357-361.

107. *CRC Handbook of Chemistry and Physics, 82th ed*, ed. D.R. Lide. 2002, Boca Raton, FL.: CRC Press.

108. Bannat, I., et al., *Improving the Photocatalytic Performance of Mesoporous Titania Films by Modification with Gold Nanostructures.* Chemistry of Materials, 2009. **21**(8): p. 1645-1653.

109. Kalousek, V., et al., *Mesoporous layers of TiO_2 as highly efficient photocatalysts for the purification of air.* Superlattices and Microstructures, 2008. **44**(4-5): p. 506-513.

110. Giannakopoulou, T., et al., *Composite hydroxyapatite/TiO_2 materials for photocatalytic oxidation of NO_x.* Materials Science and Engineering: B, 2012. **177**(13): p. 1046-1052.

111. Samantaray, C.B., H. Sim, and H. Hwang, *The electronic structures and optical properties of $BaTiO_3$ and $SrTiO_3$ using first-principles calculations.* Microelectronics Journal, 2005. **36**(8): p. 725-728.

112. Wemple, S.H., *Polarization Fluctuations and the Optical-Absorption Edge in $BaTiO_3$.* Physical Review B, 1970. **2**(7): p. 2679-2689.

6. APPENDIX

6.1 Pretreatment of the Samples: The Effect of Activation Time

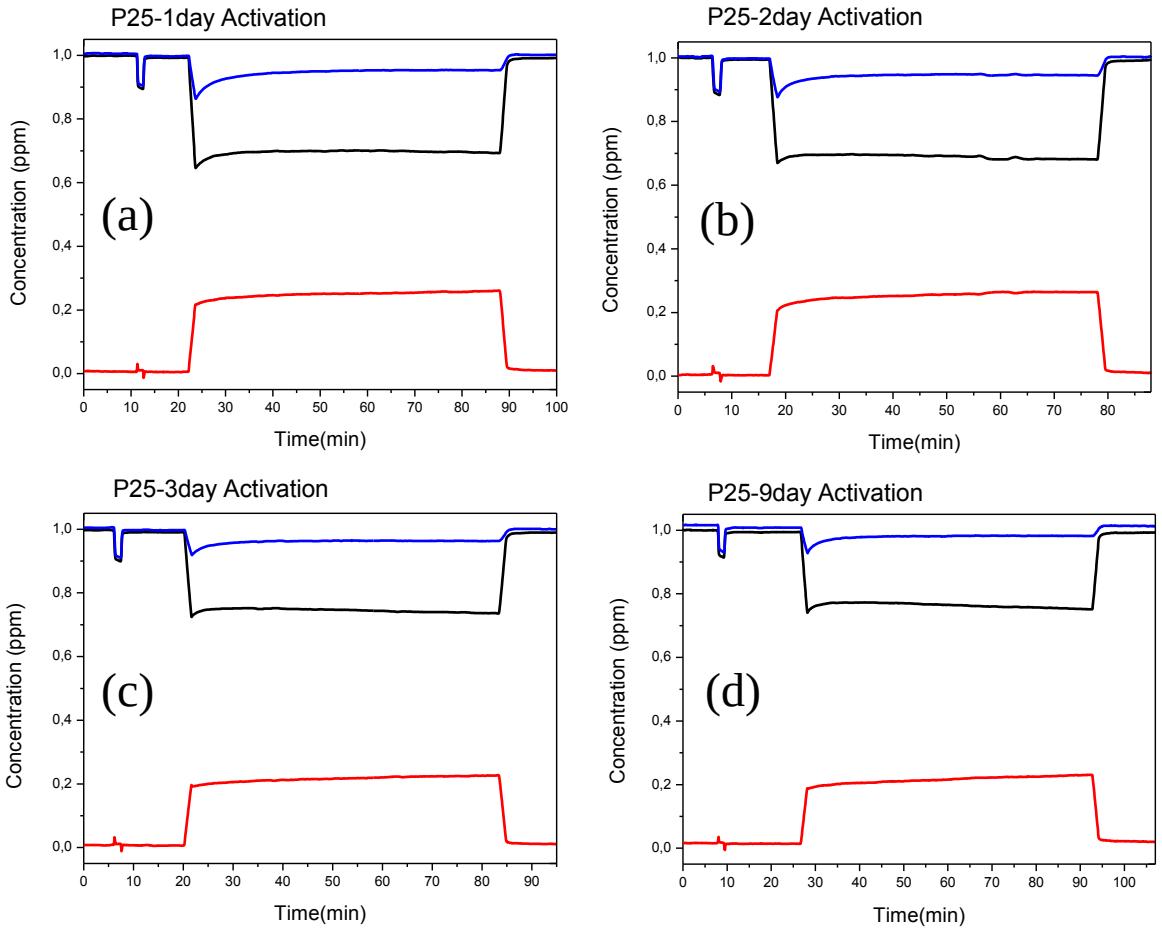

Figure 70. Performance plots of 300 mg Degussa P25 that has been pretreated under UV light for (a) 1 day (a) 2 days (a) 3 days (a) 9 days.

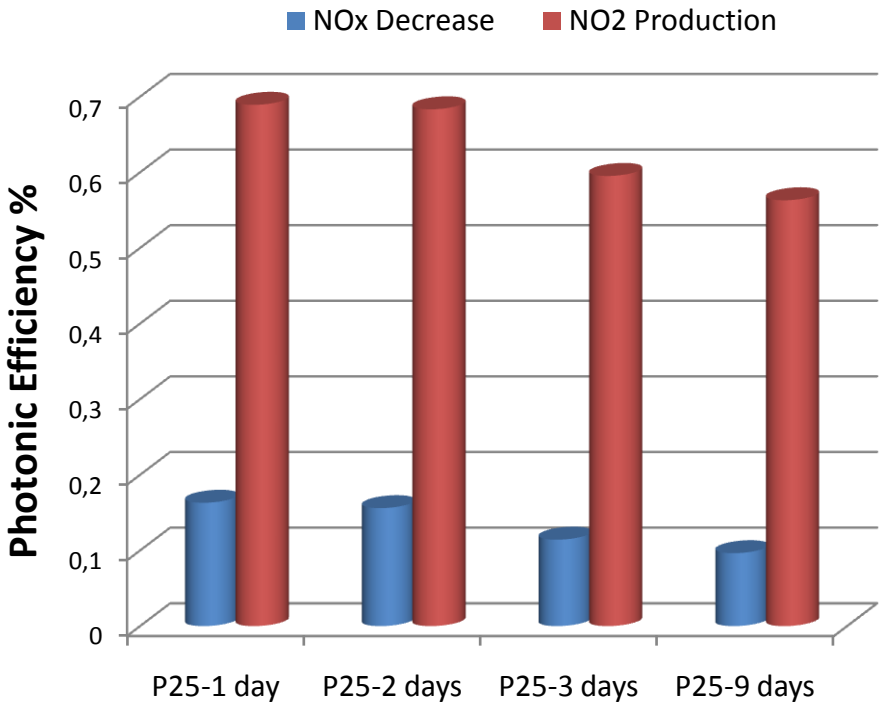

Figure 71. The photonic efficiencies of 300 mg Degussa P25 that has been pretreated under UV light for 1 day, 2 days, 3 days, 9 days.

6.2 Regeneration of the PhoNOS catalysts

A 0.5-Ti/Al-900+5BaO(PM) sample was taken out of the reactor after the 60 minute-photocatalytic NO_x abatement test, washed in 10 ml de-ionized water and filtered with Millipore 0.22 μm filter paper. The powder was dried under ambient conditions and pressed into the sample holder after most of the water was evaporated. Next, the sample was placed inside a custom designed UVA cabinet for an 18 h activation period and at the end of the UV-pretreatment, the PhoNOS perfomance of the regenerated sample, 0.5-Ti/Al-900+5BaO(PM-R), was tested in the usual way.

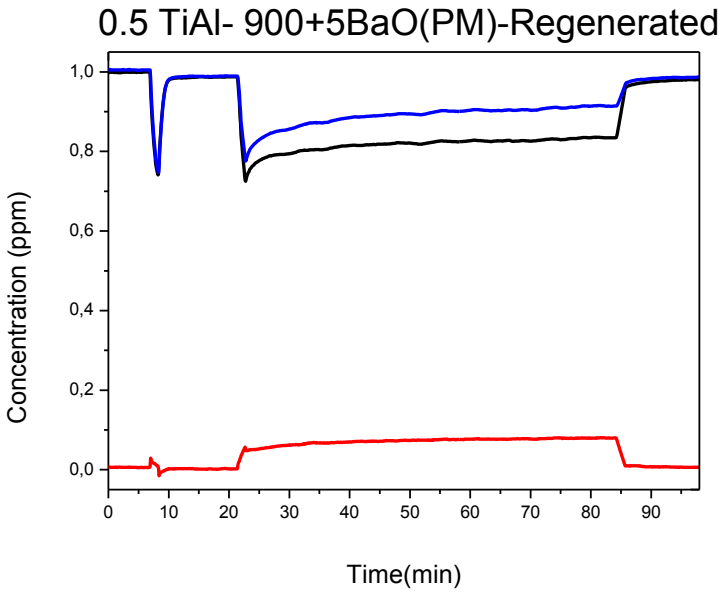

Figure 72. Performance plot of regenerated 0.5-Ti/Al-900+5BaO (PM), which was washed in water, filtered and dried at room temperature, after the initital performance experiment.

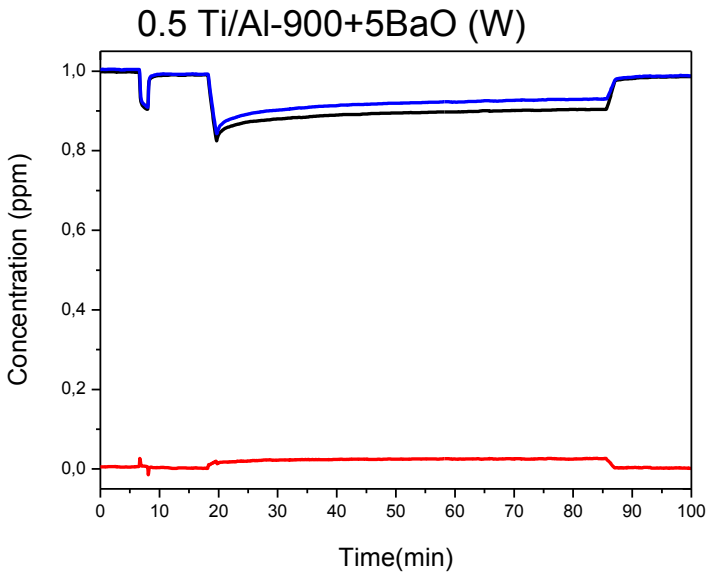

Figure 73. Performance plot of fresh 0.5-Ti/Al-900+5BaO (W), which was prepared by mixing 0.5-Ti/Al-900 and 5% (w/w) BaO in 50 ml water. The resulting suspension was stirred for 4 h at 80^{o}C until the water evaporated and the remaining powder was dried at 150^{o}C for 1 h.

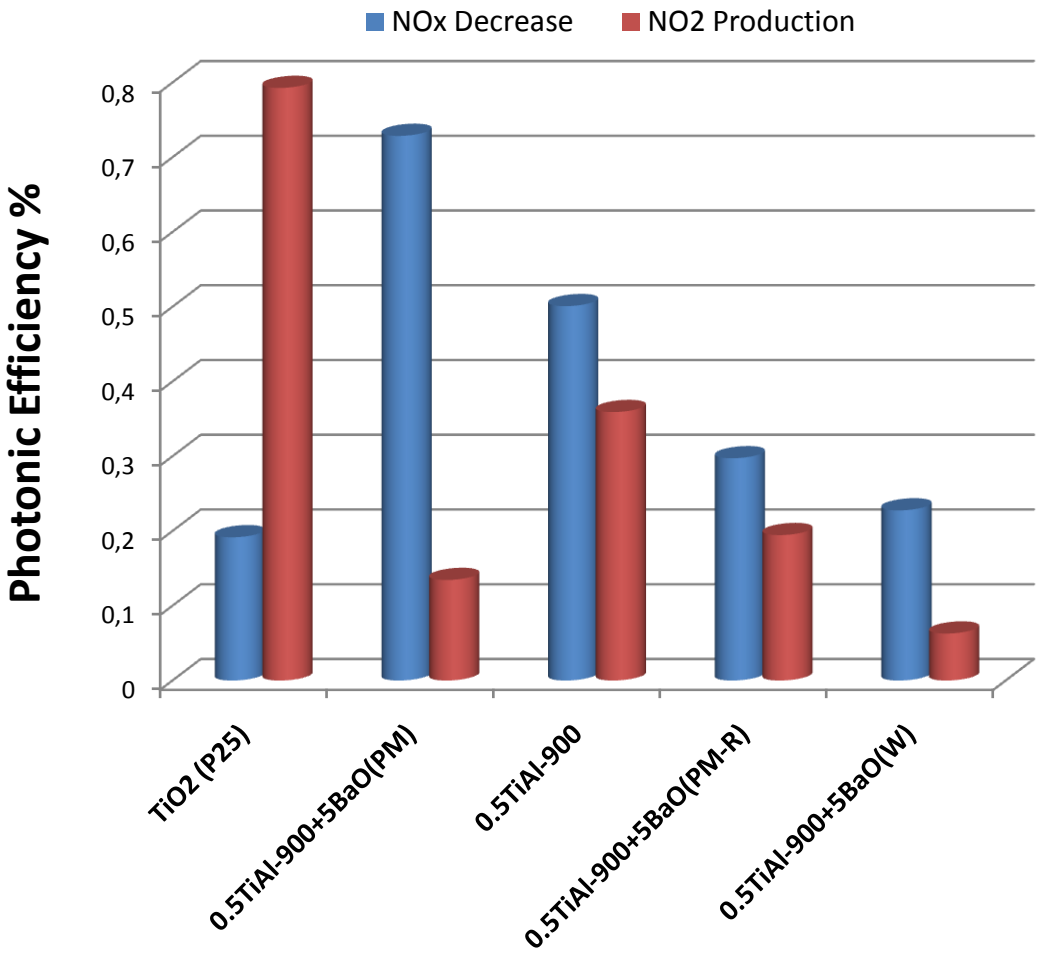

Figure 74. The photonic efficiencies of 0.5 Ti/Al-900+5BaO(PM), 0.5 Ti/Al-900, 0.5 Ti/Al-900+5BaO(PM-R) which was washed (regenerated) with water and 0.5 Ti/Al-900+5BaO(W) which was prepared in water is shown, in comparison with Degussa P25 TiO_2.

6.3 Photonic Efficiencies of PhoNOS catalysts

Table 14. The photonic efficiency percentages for all tested samples (calculated for the first hour of UVA irradiation).

Sample Name	**NO Abatement (Oxidation) Efficiency %**	**NO_x Abatement (Storage) Efficiency %**	**$NO_{2(g)}$ Production Efficiency %**
Reference			
γ-Al_2O_3	0,060	0,049	0,014
Al_2O_3+10BaO	0,069	0,052	0,017
Degussa P25	0,983	0,192	0,793
Thermally Treated 0.25 Ti/Al Samples			
0.25 Ti/Al -UNC	0,046	0,044	0,001
0.25 Ti/Al -800	0,045	0,034	0,011
0.25 Ti/Al -900	0,203	0,178	0,024
0.25 Ti/Al -950	0,469	0,283	0,184
0.25 Ti/Al -1000	0,445	0,151	0,300
Thermally Treated 0.5 Ti/Al Samples			
0.5 Ti/Al -UNC	0,077	0,064	0,005
0.5 Ti/Al -150	0,061	0,052	0,006
0.5 Ti/Al -350	0,044	0,032	0,004
0.5 Ti/Al -600	0,031	0,028	0,005
0.5 Ti/Al -800	0,053	0,043	0,006
0.5 Ti/Al -900	0,850	0,501	0,359
0.5 Ti/Al -1000	0,509	0,180	0,327
Thermally Treated 1.0 Ti/Al Samples			
1.0 Ti/Al -UNC	0,062	0,042	0,005

Sample Name	**NO Abatement (Oxidation) Efficiency %**	**NO_x Abatement (Storage) Efficiency %**	**$NO_{2(g)}$ Production Efficiency %**
1.0 Ti/Al -150	0,062	0,048	0,011
1.0 Ti/Al -350	0,109	0,069	0,034
1.0 Ti/Al -600	0,109	0,085	0,021
1.0 Ti/Al -800	1,018	0,470	0,518
1.0 Ti/Al -900	0,994	0,429	0,569
1.0 Ti/Al -1000	0,748	0,183	0,553
Metal Nitrate Impregnated 0.5 Ti/Al-900 Samples			
0.5TiAl-900 +5Ba(IM)	0,436	0,273	0,160
0.5TiAl-900 +10Ba(IM)	0,356	0,231	0,121
5% Metal Nitrate Impregnated 1.0 Ti/Al-800 Samples			
1.0TiAl-800 +5Li(IM)	0,168	0,114	0,055
1.0TiAl-800 +5Na(IM)	0,087	0,062	0,027
1.0TiAl-800 +5K(IM)	0,126	0,098	0,029
1.0TiAl-800 +5Cs(IM)	0,285	0,216	0,069
1.0TiAl-800 +5Ca(IM)	0,466	0,322	0,142
1.0TiAl-800 +5Sr(IM)	0,437	0,299	0,135
1.0TiAl-800 +5Ba(IM)	0,577	0,378	0,198
10% Metal Nitrate Impregnated 1.0 Ti/Al-800 Samples			
1.0TiAl-800+10Li(IM)	0,127	0,092	0,035

Sample Name	NO Abatement (Oxidation) Efficiency %	NO_x Abatement (Storage) Efficiency %	$NO_{2(g)}$ Production Efficiency %
1.0TiAl-800 +10Na(IM)	0,045	0,022	0,023
1.0TiAl-800 +10K(IM)	0,024	-0,002	0,024
1.0TiAl-800 +10Cs(IM)	0,181	0,152	0,028
1.0TiAl-800 +10Ca(IM)	0,168	0,114	0,055
1.0TiAl-800 +10Sr(IM)	0,227	0,159	0,069
1.0TiAl-800 +10Ba(IM)	0,466	0,306	0,166
5% Metal Nitrate Impregnated 1.0 Ti/Al-900 Samples			
1.0TiAl-900 +5Li(IM)	0,126	0,081	0,045
1.0TiAl-900 +5Na(IM)	0,242	0,161	0,083
1.0TiAl-900 +5K(IM)	0,200	0,167	0,033
1.0TiAl-900 +5Cs(IM)	0,110	0,087	0,022
1.0TiAl-900 +5Ca(IM)	0,293	0,174	0,120
1.0TiAl-900 +5Sr(IM)	0,302	0,176	0,128
1.0TiAl-900 +5Ba(IM)	0,642	0,345	0,296
10% Metal Nitrate Impregnated 1.0 Ti/Al-900 Samples			
1.0TiAl-900 +10Li(IM)	0,014	0,014	0,003
1.0TiAl-900 +10Na(IM)	0,096	0,034	0,064

Sample Name	NO Abatement (Oxidation) Efficiency %	NO_x Abatement (Storage) Efficiency %	$NO_{2(g)}$ Production Efficiency %
1.0TiAl-900 +10K(IM)	0,029	-0,011	0,039
1.0TiAl-900 +10Cs(IM)	0,056	0,020	0,035
1.0TiAl-900 +10Ca(IM)	0,056	0,034	0,023
1.0TiAl-900 +10Sr(IM)	0,420	0,236	0,188
1.0TiAl-900 +10Ba(IM)	0,367	0,212	0,160
Physical Mixtures of Ti/Al and BaO			
0.5TiAl-900 +5BaO(PM)	0,861	0,729	0,135
0.5TiAl-900 +5BaO(PM)-Regenerated	0.498	0.297	0.195
1.0TiAl-800 +5BaO(PM)	0,996	0,778	0,215
1.0TiAl-800 +10BaO(PM)	0,938	0,779	0,157
1.0TiAl-900 +5BaO(PM)	1,020	0,681	0,339
1.0TiAl-900 +10BaO(PM)	1,018	0,724	0,293
Physical Mixtures of Degussa P25 TiO_2, γ-Al_2O_3 and BaO			
P25+ γ-Al_2O_3(PM)	1,201	0,743	0,474
P25+ γ-Al_2O_3 +5BaO(PM)	1,202	0,819	0,383
P25+ γ-Al_2O_3 +10BaO(PM)	1,202	0,881	0,322

Table 15. The number of moles of oxidized $NO_{(g)}$, stored NO_x and produced $NO_{2(g)}$ by all tested samples (calculated for the first hour of UVA irradiation).

Sample Name	**NO Abatement (Oxidation) μmol/h**	**NO_x Abatement (Storage) μmol/h**	**$NO_{2(g)}$ Production μmol/h**
Reference			
γ-Al_2O_3	0,050	0,041	0,011
Al_2O_3+10BaO	0,058	0,044	0,014
Degussa P25	0,827	0,161	0,666
Thermally Treated 0.25 Ti/Al Samples			
0.25 Ti/Al -UNC	0,038	0,037	0,001
0.25 Ti/Al -800	0,037	0,029	0,009
0.25 Ti/Al -900	0,170	0,150	0,020
0.25 Ti/Al -950	0,394	0,237	0,154
0.25 Ti/Al -1000	0,374	0,127	0,252
Thermally Treated 0.5 Ti/Al Samples			
0.5 Ti/Al -UNC	0,065	0,053	0,004
0.5 Ti/Al -150	0,051	0,044	0,005
0.5 Ti/Al -350	0,037	0,027	0,003
0.5 Ti/Al -600	0,026	0,023	0,004
0.5 Ti/Al -800	0,044	0,036	0,005
0.5 Ti/Al -900	0,714	0,421	0,302
0.5 Ti/Al -1000	0,428	0,152	0,275
Thermally Treated 1.0 Ti/Al Samples			
1.0 Ti/Al -UNC	0,052	0,036	0,004
1.0 Ti/Al -150	0,052	0,041	0,009

Sample Name	**NO Abatement (Oxidation) μmol/h**	**NO_x Abatement (Storage) μmol/h**	**$NO_{2(g)}$ Production μmol/h**
1.0 Ti/Al -350	0,091	0,058	0,028
1.0 Ti/Al -600	0,092	0,072	0,018
1.0 Ti/Al -800	0,855	0,394	0,435
1.0 Ti/Al -900	0,835	0,360	0,478
1.0 Ti/Al -1000	0,628	0,153	0,465
Metal Nitrate Impregnated 0.5 Ti/Al-900 Samples			
0.5TiAl-900 +5Ba(IM)	0,366	0,229	0,134
0.5TiAl-900 +10Ba(IM)	0,299	0,194	0,102
5% Metal Nitrate Impregnated 1.0 Ti/Al-800 Samples			
1.0TiAl-800 +5Li(IM)	0,141	0,096	0,046
1.0TiAl-800 +5Na(IM)	0,073	0,052	0,023
1.0TiAl-800 +5K(IM)	0,106	0,083	0,024
1.0TiAl-800 +5Cs(IM)	0,240	0,182	0,058
1.0TiAl-800 +5Ca(IM)	0,392	0,271	0,119
1.0TiAl-800 +5Sr(IM)	0,367	0,251	0,113
1.0TiAl-800 +5Ba(IM)	0,485	0,318	0,166
10% Metal Nitrate Impregnated 1.0 Ti/Al-800 Samples			
1.0TiAl-800+10Li(IM)	0,106	0,077	0,030
1.0TiAl-800 +10Na(IM)	0,038	0,019	0,019

Sample Name	NO Abatement (Oxidation) μmol/h	NO_x Abatement (Storage) μmol/h	$NO_{2(g)}$ Production μmol/h
1.0TiAl-800 +10K(IM)	0,020	-0,002	0,020
1.0TiAl-800 +10Cs(IM)	0,152	0,128	0,023
1.0TiAl-800 +10Ca(IM)	0,141	0,096	0,046
1.0TiAl-800 +10Sr(IM)	0,191	0,134	0,058
1.0TiAl-800 +10Ba(IM)	0,392	0,257	0,139
5% Metal Nitrate Impregnated 1.0 Ti/Al-900 Samples			
1.0TiAl-900 +5Li(IM)	0,106	0,068	0,038
1.0TiAl-900 +5Na(IM)	0,203	0,135	0,069
1.0TiAl-900 +5K(IM)	0,168	0,140	0,028
1.0TiAl-900 +5Cs(IM)	0,093	0,073	0,018
1.0TiAl-900 +5Ca(IM)	0,246	0,146	0,101
1.0TiAl-900 +5Sr(IM)	0,254	0,148	0,108
1.0TiAl-900 +5Ba(IM)	0,539	0,289	0,249
10% Metal Nitrate Impregnated 1.0 Ti/Al-900 Samples			
1.0TiAl-900 +10Li(IM)	0,012	0,012	0,002
1.0TiAl-900 +10Na(IM)	0,081	0,028	0,054
1.0TiAl-900 +10K(IM)	0,024	-0,010	0,033

Sample Name	**NO Abatement (Oxidation) μmol/h**	**NO_x Abatement (Storage) μmol/h**	**$NO_{2(g)}$ Production μmol/h**
1.0TiAl-900 +10Cs(IM)	0,047	0,017	0,029
1.0TiAl-900 +10Ca(IM)	0,047	0,029	0,019
1.0TiAl-900 +10Sr(IM)	0,353	0,198	0,158
1.0TiAl-900 +10Ba(IM)	0,309	0,178	0,134
Physical Mixtures of Ti/Al and BaO			
0.5TiAl-900 +5BaO(PM)	0,724	0,612	0,113
0.5TiAl-900 +5BaO(PM)-Regenerated	0.418	0.250	0.164
1.0TiAl-800 +5BaO(PM)	0,837	0,654	0,196
1.0TiAl-800 +10BaO(PM)	0,788	0,655	0,147
1.0TiAl-900 +5BaO(PM)	0,857	0,572	0,285
1.0TiAl-900 +10BaO(PM)	0,855	0,608	0,246
Physical Mixtures of Degussa P25 TiO_2, γ-Al_2O_3 and BaO			
P25+ γ-Al_2O_3(PM)	1,009	0,624	0,398
P25+ γ-Al_2O_3 +5BaO(PM)	1,010	0,688	0,339
P25+ γ-Al_2O_3 +10BaO(PM)	1,010	0,740	0,288

6.4 UV-VIS Absorption Spectra (Diffuse Reflectance) and Band Gap Measurements of Selected PhoNOS catalysts

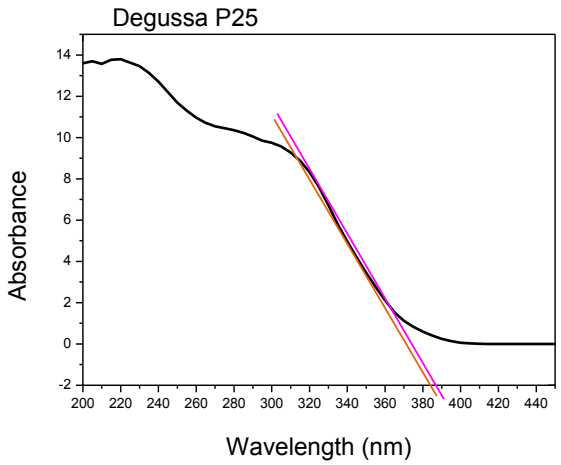

Figure 75. UV-VIS Absorption Spectrum (Diffuse Reflectance) of Degussa P25.

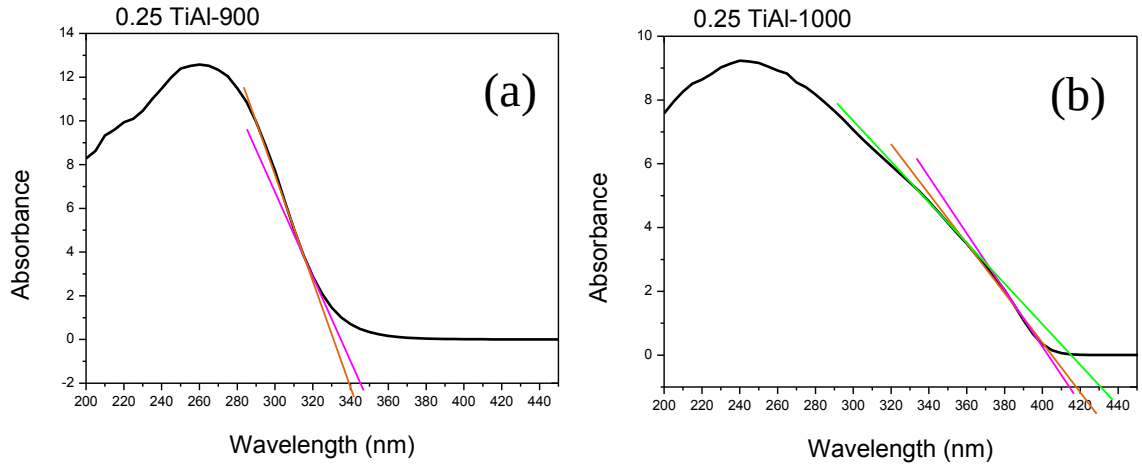

Figure 76. UV-VIS Absorption Spectra (Diffuse Reflectance) of (a) 0.25 Ti/Al-900 (b) 0.25 Ti/Al-1000.

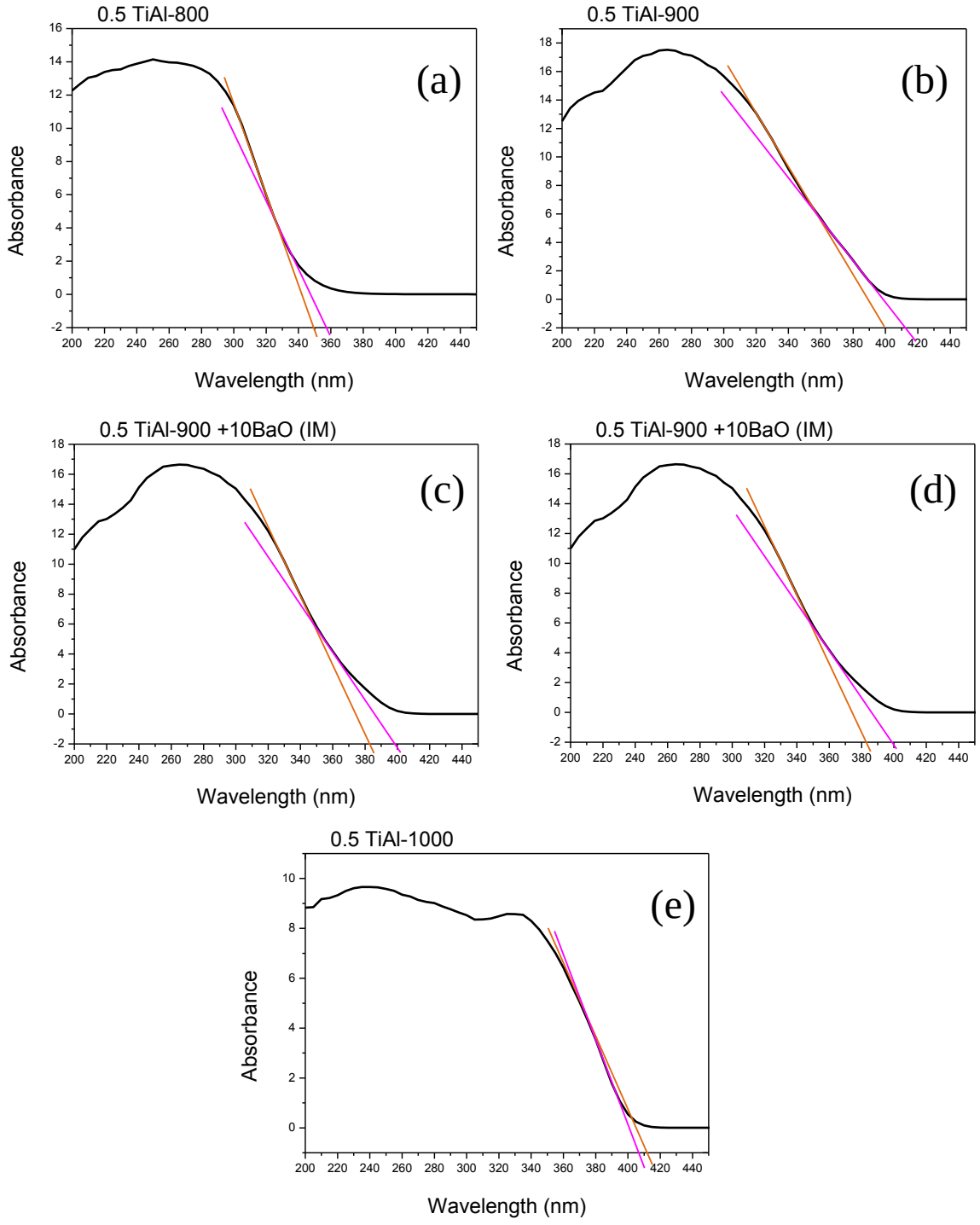

Figure 77. UV-VIS Absorption Spectra (Diffuse Reflectance) of (a) 0.5 Ti/Al-800 (b) 0.5 Ti/Al-900 (c) 0.5 Ti/Al-900 +10BaO (IM) (d) 0.5 Ti/Al-900+ 10BaO (PM) (e) 0.5 Ti/Al-1000

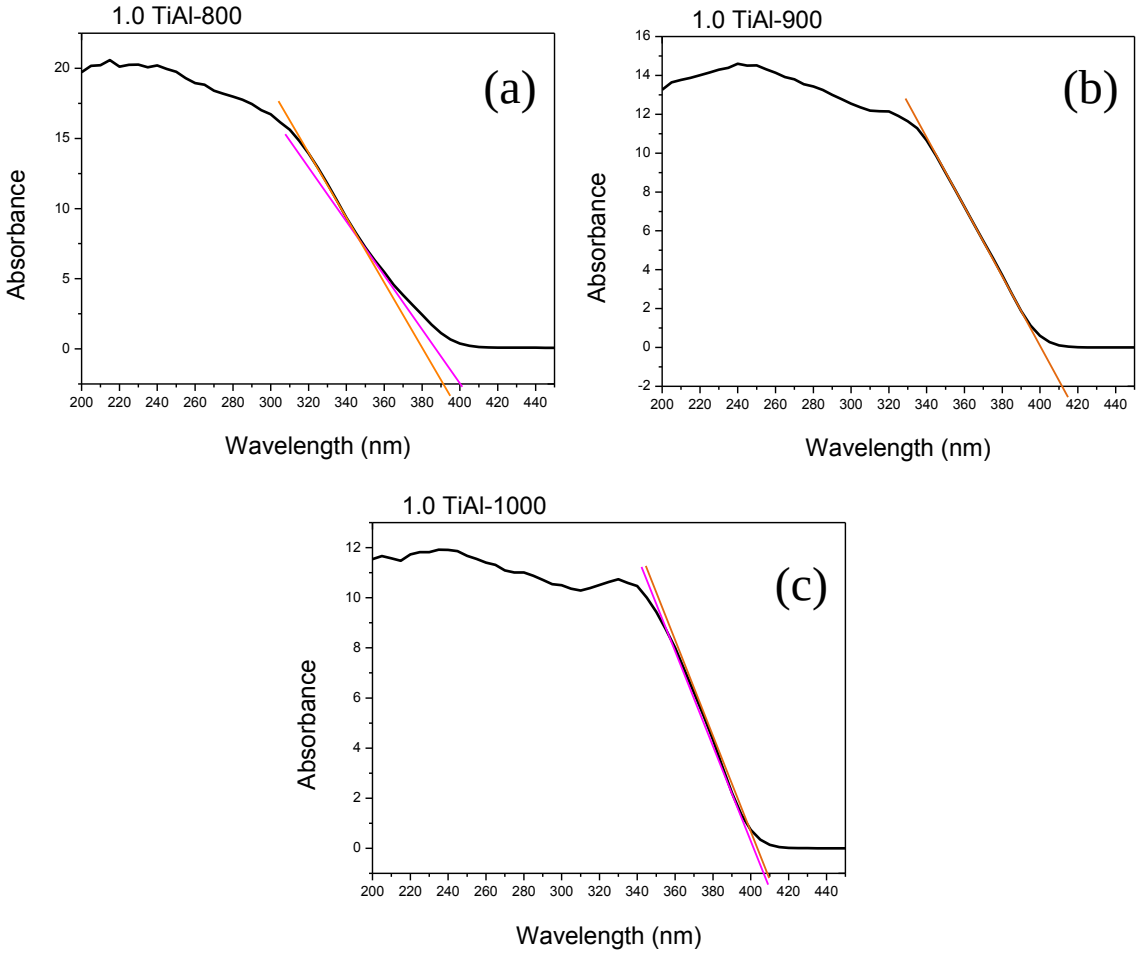

Figure 78. UV-VIS Absorption Spectra (Diffuse Reflectance) of (a) 1.0 Ti/Al-800 (b) 1.0 Ti/Al-900 (c) 1.0 Ti/Al-1000

Table 16. Absorption edge wavelengths (nm) and approximate band gap energies (eV) of the selected PhoNOS catalysts.

Sample Name	Absorption Edge Wavelength (nm)	Band gap (eV)
P25	386-394	3.18±0.03
0.25 Ti/Al-900	340-345	3.62±0.02
0.25 Ti/Al-1000	414-418	2.98±0.01
0.5 Ti/Al-800	350-357	3.51±0.04
0.5 Ti/Al-900	400-412	3.05± 0.05

Sample Name	Absorption Edge Wavelength (nm)	Band gap (eV)
0.5 Ti/Al-900+10BaO(PM)	403-413	3.04± 0.04
0.5 Ti/Al-900+10BaO(IM)	383-399	3.17± 0.06
0.5 Ti/Al-1000	406-412	3.04± 0.02
1.0 Ti/Al-800	391-400	3.14± 0.03
1.0 Ti/Al-900	411	3.02
1.0 Ti/Al-1000	406-409	3.04±0.01

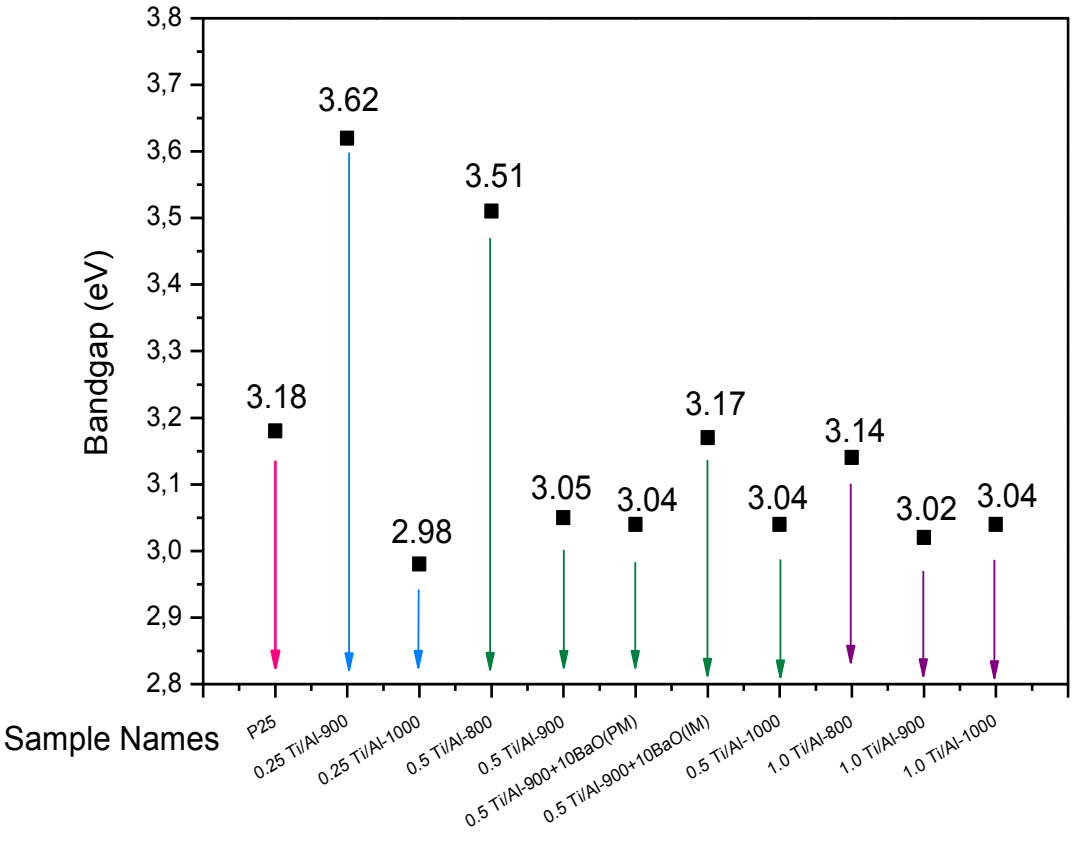

Figure 79. Approximate band gap energies (eV) of the selected PhoNOS catalysts. Blue arrow indicate 0.25 Ti/Al samples, green arrows show 0.5 Ti/Al samples and purple arrows indicate 1.0 Ti/Al samples.

In a classical semiconductor, photons with energies smaller than the band gap ($E_{ph} < E_g$) are mostly reflected from the top surface compared to photons with energies greater than the bandgap ($E_{ph} > E_g$), which are mostly absorbed in the material. As a result, a sharp increase in absorption is observed in the UV-Vis absorbance spectrum, at energies close to the band gap. This feature in the spectrum is defined as the absorption edge or reflection threshold.

Table 15 and Figure 76 show that when the Ti/Al binary oxide is mostly amorphous, the UV-Vis absorption edge (or reflection threshold) is observed at a smaller wavelength and consequently band gap of the sample is much larger than when titania is in crystalline structure. For example 0.25 Ti/Al-900 and 0.5 Ti/Al-800 which are amorphous according to their XRD patterns (Figure 39-a and b) display bandgap energies around 3.5 – 3.6 eV. However, when these binary oxides are calcined at higher temperatures, a significant decrease in the bandgap is observed, according to the TiO_2 crystalline phase that is formed. For instance, 0.25 Ti/Al-1000 is fully rutile (Figure 39-a) so the material has a band gap energy of approximately 3.0 eV. 0.5 Ti/Al-900 and 0.5 Ti/Al-1000 are also almost all rutile in structure (Figure 39-b), so their bandgaps are around 3.05 and 3.04 eV respectively, very close to the experimental band gap of pure rutile TiO_2. 1.0 Ti/Al-800, on the other hand, exhibits both anatase and rutilephases (Figure 39-c), so it has a band gap energy in between that of anatase and rutile TiO_2, around 3.14 eV. When 1.0 Ti/Al is heated further to 900 and 1000^oC, the crystalline phase transforms to completely rutile and the band gap of the sample decreases accordingly to 3.02 and 3.04 eV, for these samples, respectively.

The ternary oxides, 0.5 Ti/Al-900+10BaO (PM) and 0.5 Ti/Al-900+10BaO (IM), exhibit different behaviors; while the physically mixing 10% (w/w) BaO had almost no effect on the band gap of 0.5 Ti/Al-900, impregnation of 0.5 Ti/Al-900 with 10% $Ba(NO_3)_2$, increased its bandgap from 3.05 eV to 3.17 eV. This difference can be accounted for by the formation $BaTiO_3$, whose experimental band gap energy is around 3.15-3.2 eV[111, 112].

Some of the figures in this manuscript are reproduced from previous publications and their copyright permissions are presented below.

31 07 2012 Rightslink Printable License

ELSEVIER LICENSE
TERMS AND CONDITIONS

Jul 30, 2012

This is a License Agreement between Asli Melike Soylu ("You") and Elsevier ("Elsevier") provided by Copyright Clearance Center ("CCC"). The license consists of your order details, the terms and conditions provided by Elsevier, and the payment terms and conditions.

All payments must be made in full to CCC. For payment instructions, please see information listed at the bottom of this form.

Supplier	Elsevier Limited The Boulevard,Langford Lane Kidlington,Oxford,OX5 1GB,UK
Registered Company Number	1982084
Customer name	Asli Melike Soylu
Customer address	Bilkent Universitesi Fen Fakultesi Ankara, Turkey 06800
License number	2958971164863
License date	Jul 30, 2012
Licensed content publisher	Elsevier
Licensed content publication	Journal of Catalysis
Licensed content title	In situ FTIR study of photocatalytic NO reaction on photocatalysts under UV irradiation
Licensed content author	Jeffrey C.S. Wu,Yu-Ting Cheng
Licensed content date	25 January 2006
Licensed content volume number	237
Licensed content issue number	2
Number of pages	12
Start Page	393

End Page	404
Type of Use	reuse in a thesis/dissertation
Intended publisher of new work	other
Portion	figures/tables/illustrations
Number of figures/tables/illustrations	2
Format	print
Are you the author of this Elsevier article?	No
Will you be translating?	No
Order reference number	
Title of your thesis/dissertation	PHOTOCATALYTIC NOX OXIDATION AND STORAGE UNDER AMBIENT CONDITIONS FOR AIR PURIFICATION
Expected completion date	Jul 2012
Estimated size (number of pages)	150
Elsevier VAT number	GB 494 6272 12
Permissions price	0.00 USD
VAT/Local Sales Tax	0.0 USD / 0.0 GBP
Total	0.00 USD

Terms and Conditions

INTRODUCTION

1. The publisher for this copyrighted material is Elsevier. By clicking "accept" in connection with completing this licensing transaction, you agree that the following terms and conditions apply to this transaction (along with the Billing and Payment terms and conditions established by Copyright Clearance Center, Inc. ("CCC"), at the time that you opened your Rightslink account and that are available at any time at http://myaccount.copyright.com).

GENERAL TERMS

2. Elsevier hereby grants you permission to reproduce the aforementioned material subject to the terms and conditions indicated.

3. Acknowledgement: If any part of the material to be used (for example, figures) has appeared in our publication with credit or acknowledgement to another source, permission must also be sought from that source. If such permission is not obtained then that material may not be included in your publication/copies. Suitable

acknowledgement to the source must be made, either as a footnote or in a reference list at the end of your publication, as follows: “Reprinted from Publication title, Vol /edition number, Author(s), Title of article / title of chapter, Pages No., Copyright (Year), with permission from Elsevier [OR APPLICABLE SOCIETY COPYRIGHT OWNER].” Also Lancet special credit - “Reprinted from The Lancet, Vol. number, Author(s), Title of article, Pages No., Copyright (Year), with permission from Elsevier.”

4. Reproduction of this material is confined to the purpose and/or media for which permission is hereby given.

5. Altering/Modifying Material: Not Permitted. However figures and illustrations may be altered/adapted minimally to serve your work. Any other abbreviations, additions, deletions and/or any other alterations shall be made only with prior written authorization of Elsevier Ltd. (Please contact Elsevier at permissions@elsevier.com)

6. If the permission fee for the requested use of our material is waived in this instance, please be advised that your future requests for Elsevier materials may attract a fee.

7. Reservation of Rights: Publisher reserves all rights not specifically granted in the combination of (i) the license details provided by you and accepted in the course of this licensing transaction, (ii) these terms and conditions and (iii) CCC's Billing and Payment terms and conditions.

8. License Contingent Upon Payment: While you may exercise the rights licensed immediately upon 31 07 2012 Rightslink Printable License issuance of the license at the end of the licensing process for the transaction, provided that you have disclosed complete and accurate details of your proposed use, no license is finally effective unlessand until full payment is received from you (either by publisher or by CCC) as provided in CCC's Billing and Payment terms and conditions. If full payment is not received on a timely basis, then any license preliminarily granted shall be deemed automatically revoked and shall be void as if never granted. Further, in the event that you breach any of these terms and conditions or any of CCC's Billing and Payment terms and conditions, the license is automatically revoked and shall be void as if never granted. Use of materials as described in a revoked license, as well as any use of the materials beyond the scope of an unrevoked license, may constitute copyright infringement and publisher reserves the right to take any and all action to protect its copyright in the materials.

9. Warranties: Publisher makes no representations or warranties with respect to the licensed material.

10. Indemnity: You hereby indemnify and agree to hold harmless publisher and CCC, and their respective officers, directors, employees and agents, from and against any and all claims arising out of your use of the licensed material other than as specifically authorized pursuant to this license.

11. No Transfer of License: This license is personal to you and may not be sublicensed, assigned, or transferred by you to any other person without publisher's written permission.

12. No Amendment Except in Writing: This license may not be amended except in a writing signed by both parties (or, in the case of publisher, by CCC on publisher's behalf).

13. Objection to Contrary Terms: Publisher hereby objects to any terms contained in any purchase order, acknowledgment, check endorsement or other writing prepared by you, which terms are inconsistent with these terms and conditions or CCC's Billing and Payment terms and conditions.
These terms and conditions, together with CCC's Billing and Payment terms and conditions (which are incorporated herein), comprise the entire agreement between you and publisher (and CCC) concerning this licensing transaction. In the event of any conflict between your obligations established by these terms and conditions and those established by CCC's Billing and Payment terms and conditions, these terms and conditions shall control.

14. Revocation: Elsevier or Copyright Clearance Center may deny the permissions described in this License at their sole discretion, for any reason or no reason, with a full refund payable to you. Notice of such denial will be made using the contact information provided by you. Failure to receive such notice will not alter or invalidate the denial. In no event will Elsevier or Copyright Clearance Center be responsible or liable for any costs, expenses or damage incurred by you as a result of a denial of your permission request, other than a refund of the amount(s) paid by you to Elsevier and/or Copyright Clearance Center for denied permissions.

LIMITED LICENSE
The following terms and conditions apply only to specific license types:

15. Translation: This permission is granted for non-exclusive world English rights only unless your license was granted for translation rights. If you licensed translation rights you may onl translate this content into the languages you requested. A professional translator must perform all translations and reproduce the content word for word preserving the integrity of the article. If this license is to re-use 1 or 2 figures then permission is granted for non-exclusive world rights in all languages.

16. Website: The following terms and conditions apply to electronic reserve and author websites:
Electronic reserve: If licensed material is to be posted to website, the web site is to be password-protected and made available only to bona fide students registered on a relevant course
if:
This license was made in connection with a course,
This permission is granted for 1 year only. You may obtain a license for future website posting,
All content posted to the web site must maintain the copyright information line on the bottom of each image,

A hyper-text must be included to the Homepage of the journal from which you are licensing at http://www.sciencedirect.com/science/journal/xxxxx or the Elsevier homepage for books at http://www.elsevier.com , and
Central Storage: This license does not include permission for a scanned version of the material to be stored in a central repository such as that provided by Heron/XanEdu.

17. Author website for journals with the following additional clauses:
All content posted to the web site must maintain the copyright information line on the bottom of each image, and the permission granted is limited to the personal version of your paper. You are not allowed to download and post the published electronic version of your article (whether PDF or HTML, proof or final version), nor may you scan the printed edition to create an electronic version. A hyper-text must be included to the Homepage of the journal from which you are licensing at http://www.sciencedirect.com/science/journal/xxxxx . As part of our normal production process, you will receive an e-mail notice when your article appears on Elsevier's online service ScienceDirect (www.sciencedirect.com). That e-mail will include the article's Digital Object Identifier (DOI). This number provides the electronic link to the published article and should be included in the posting of your personal version. We ask that you wait until you receive this e-mail and have the DOI to do any posting. Central Storage: This license does not include permission for a scanned version of the material to be stored in a central repository such as that provided by Heron/XanEdu.

18. Author website for books with the following additional clauses:
Authors are permitted to place a brief summary of their work online only.
A hyper-text must be included to the Elsevier homepage at http://www.elsevier.com .
All content posted to the web site must maintain the copyright information line on the bottom of each image. You are not allowed to download and post the published electronic version of your chapter, nor may you scan the printed edition to create an electronic version.
Central Storage: This license does not include permission for a scanned version of the material to be stored in a central repository such as that provided by Heron/XanEdu.
19. Website (regular and for author): A hyper-text must be included to the Homepage of the journal from which you are licensing at http://www.sciencedirect.com/science/journal/xxxxx. or for books to the Elsevier homepage at http://www.elsevier.com

20. Thesis/Dissertation: If your license is for use in a thesis/dissertation your thesis may be submitted to your institution in either print or electronic form. Should your thesis be published commercially, please reapply for permission. These requirements include permission for the Library and Archives of Canada to supply single copies, on demand, of the complete thesis and include permission for UMI to supply single copies, on demand, of the complete thesis. Should your thesis
be published commercially, please reapply for permission.

21. Other Conditions:
v1.6

If you would like to pay for this license now, please remit this license along with your payment made payable to "COPYRIGHT CLEARANCE CENTER" otherwise you will be invoiced within 48 hours of the license date. Payment should be in the form of a check or money order referencing your account number and this invoice number RLNK500828519.

Once you receive your invoice for this order, you may pay your invoice by credit card. Please follow instructions provided at that time.
Make Payment To:
Copyright Clearance Center
Dept 001
P.O. Box 843006
Boston, MA 02284-3006
For suggestions or comments regarding this order, contact RightsLink Customer Support: customercare@copyright.com or +1-877-622-5543 (toll free in the US) or +1-978-646- 2777.
Gratis licenses (referencing $0 in the Total field) are free. Please retain this printable license for your reference. No payment is required.

IOP PUBLISHING
LICENSE

July 31, 2012

To whom it may concern,

I am a Master's Student in Bilkent University-Chemistry Department (Ankara, Turkey) and I am preparing a Master's thesis, entitled as "Photocatalytic NOx Oxidation and Storage Under Ambient Conditions for Air Purification".

I would like to ask for permission to re-use Figure 3 from the following article in my thesis: Wang, H. and J.P. Lewis, Second-generation photocatalytic materials: anion-doped TiO2. Journal of Physics-Condensed Matter, 2006. 18(2), p. 421-434.

I have already defended my thesis (on 24th July, 2012) and it is ready to be published in a couple of days, therefore I would appreciate it if you can get in touch with me as soon as possible.

Thank you.

Best regards,

Asli Melike Soylu

***

M.Sc Student
Department of Chemistry
Bilkent University, Ankara-TURKEY
Tel: 0090 312 290 1714

PERMISSION TO REPRODUCE AS REQUESTED IS GIVEN PROVIDED THAT:

(a) the consent of the author(s) is obtained
(b) the source of the material including author, title of article, title of journal, volume number, issue number (if relevant), page range (or first page if this is the only information available), date and publisher is acknowledged.
(c) for material being published electronically, a link back to the original article should be provided (via DOI).

IOP Publishing Ltd
Temple Circus
Temple Way
BRISTOL
BS1 6BE

31/07/12
Date

Rights & Permissions

SPRINGER LICENSE
TERMS AND CONDITIONS

Aug 01, 2012

This is a License Agreement between Asli Melike Soylu ("You") and Springer ("Springer") provided by Copyright Clearance Center ("CCC"). The license consists of your order details, the terms and conditions provided by Springer, and the payment terms and conditions.

All payments must be made in full to CCC. For payment instructions, please see information listed at the bottom of this form.

License Number	2960331397079
License date	Aug 01, 2012
Licensed content publisher	Springer
Licensed content publication	Journal of Materials Science (full set)
Licensed content title	Review of the anatase to rutile phase transformation
Licensed content author	Dorian A. H. Hanaor
Licensed content date	Jan 1, 2010
Volume number	46
Issue number	4
Type of Use	Thesis/Dissertation
Portion	Figures
Author of this Springer article	No
Order reference number	
Title of your thesis / dissertation	PHOTOCATALYTIC NOX OXIDATION AND STORAGE UNDER AMBIENT CONDITIONS FOR AIR PURIFICATION

Expected completion date Jul 2012

Estimated size(pages) 150

Total 0.00 USD

Terms and Conditions

Introduction
The publisher for this copyrighted material is Springer Science + Business Media. By clicking "accept" in connection with completing this licensing transaction, you agree that the following terms and conditions apply to this transaction (along with the Billing and Payment terms and conditions established by Copyright Clearance Center, Inc. ("CCC"), at the time that you opened your Rightslink account and that are available at any time at http://myaccount.copyright.com).

Limited License
With reference to your request to reprint in your thesis material on which Springer Science and Business Media control the copyright, permission is granted, free of charge, for the use indicated in your enquiry.

Licenses are for one-time use only with a maximum distribution equal to the number that you identified in the licensing process.

This License includes use in an electronic form, provided its password protected or on the university's intranet or repository, including UMI (according to the definition at the Sherpa website: http://www.sherpa.ac.uk/romeo/). For any other electronic use, please contact Springer at (permissions.dordrecht@springer.com or permissions.heidelberg@springer.com).

The material can only be used for the purpose of defending your thesis, and with a maximum of 100 extra copies in paper.

Although Springer holds copyright to the material and is entitled to negotiate on rights, this license is only valid, provided permission is also obtained from the (co) author (address is given with the article/chapter) and provided it concerns original material which does not carry references to other sources (if material in question appears with credit to another source, authorization from that source is required as well).

Permission free of charge on this occasion does not prejudice any rights we might have to charge for reproduction of our copyrighted material in the future.

Altering/Modifying Material: Not Permitted
You may not alter or modify the material in any manner. Abbreviations, additions, deletions and/or any other alterations shall be made only with prior written authorization of the author(s) and/or Springer Science + Business Media. (Please contact Springer at (permissions.dordrecht@springer.com or permissions.heidelberg@springer.com)

Reservation of Rights
Springer Science + Business Media reserves all rights not specifically granted in the combination of (i) the license details provided by you and accepted in the course of this licensing transaction, (ii) these terms and conditions and (iii) CCC's Billing and Payment terms and conditions.

Copyright Notice:Disclaimer
You must include the following copyright and permission notice in connection with any reproduction of the licensed material: "Springer and the original publisher /journal title, volume, year of publication, page, chapter/article title, name(s) of author(s), figure number(s), original copyright notice) is given to the publication in which the material was originally published, by adding; with kind permission from Springer Science and Business Media"

Warranties: None

Example 1: Springer Science + Business Media makes no representations or warranties with respect to the licensed material.

Example 2: Springer Science + Business Media makes no representations or warranties with respect to the licensed material and adopts on its own behalf the limitations and disclaimers established by CCC on its behalf in its Billing and Payment terms and conditions for this licensing transaction.

Indemnity
You hereby indemnify and agree to hold harmless Springer Science + Business Media and CCC, and their respective officers, directors, employees and agents, from and against any and all claims arising out of your use of the licensed material other than as specifically authorized pursuant to this license.

No Transfer of License
This license is personal to you and may not be sublicensed, assigned, or transferred by you to any other person without Springer Science + Business Media's written permission.

No Amendment Except in Writing
This license may not be amended except in a writing signed by both parties (or, in the case of Springer Science + Business Media, by CCC on Springer Science + Business Media's behalf).

Objection to Contrary Terms
Springer Science + Business Media hereby objects to any terms contained in any purchase order, acknowledgment, check endorsement or other writing prepared by you, which terms are inconsistent with these terms and conditions or CCC's Billing and Payment terms and conditions. These terms and conditions, together with CCC's Billing and Payment terms and conditions (which are incorporated herein), comprise the entire agreement between you and Springer Science + Business Media (and CCC) concerning this licensing transaction. In the event of any conflict between

your obligations established by these terms and conditions and those established by CCC's Billing and Payment terms and conditions, these terms and conditions shall control.

Jurisdiction
All disputes that may arise in connection with this present License, or the breach thereof, shall be settled exclusively by arbitration, to be held in The Netherlands, in accordance with Dutch law, and to be conducted under the Rules of the 'Netherlands Arbitrage Instituut' (Netherlands Institute of Arbitration).***OR:***

All disputes that may arise in connection with this present License, or the breach thereof, shall be settled exclusively by arbitration, to be held in the Federal Republic of Germany, in accordance with German law.

Other terms and conditions:

v1.3

If you would like to pay for this license now, please remit this license along with your payment made payable to "COPYRIGHT CLEARANCE CENTER" otherwise you will be invoiced within 48 hours of the license date. Payment should be in the form of a check or money order referencing your account number and this invoice number RLNK500830090.
Once you receive your invoice for this order, you may pay your invoice by credit card. Please follow instructions provided at that time.

Make Payment To:
Copyright Clearance Center
Dept 001
P.O. Box 843006
Boston, MA 02284-3006

For suggestions or comments regarding this order, contact RightsLink Customer Support:customercare@copyright.com or +1-877-622-5543 (toll free in the US) or +1-978-646-2777.

Gratis licenses (referencing $0 in the Total field) are free. Please retain this printable license for your reference. No payment is required.